Dissertation
submitted to the
Combined Faculties of
Natural Sciences and Mathematics
of the
Ruperto-Carola-University of Heidelberg,
Germany
for the degree of
Doctor of Natural Sciences

Put forward by

Aiara Lobo Gomes
Born in: Santo Estevão, Brazil

Oral examination: 29 October 2015

Planet-disk interactions in non-isothermal disks

Referees: Priv.-Doz. Dr. Hubert Klahr
Prof. Dr. Andreas Quirrenbach

Para minha família

Zusammenfassung

Protoplanetaren Scheiben bestimmen die Entstehung und die Evolution der Planeten, wobei auch die Planeten sich auf die Struktur der Scheiben auswirken. Gas und Staub in der Scheibe sind das Baumaterial der Planeten. Gezeitenkräfte zwischen Planet und Scheibe bestimmen die radiale Wanderung der Planeten (Migration) und gleichzeitig verformen die Planeten die Scheiben und bilden wahrscheinlich Lücken in ihnen. Die Wechselwirkung zwischen Planeten und Scheiben ist wichtig, um die Vielfalt der beobachteten Exoplaneten zu verstehen und um Planetenentstehungstheorien zu überprüfen. Diese Doktorarbeit untersucht neue Aspekte von Planet-Scheiben Wechselwirkungen in nicht-isothermen Scheiben, was ein entscheidender Schritt in Richtung einer besseren Beschreibung dieses Themenbereiches ist. Zu diesem Zweck werden Planet-Scheiben Strahlungshydrodynamische Simulationen durchgeführt. Zunächst wird ein Newtonsches Kühlungsgesetz verwendet, um die Dynamik von Wirbel zu untersuchen, die durch den Planeten erzeugt wurden und durch die Konvektive Überstabilität verstärkt werden. Die Entstehung von Dichteringen jenseits der eigentlichen Planeten Lücke für massereichere Planeten wird studiert sowie den Einfluss auf die Migrationsraten von massarmen Planeten. Schließlich werden Strahlungshydrodynamische Simulationen durchgeführt. Die Kopplung von Strahlungstransport und Hydrodynamik ergibt eine genauere Bestimmung der Gastemperatur in der Nähe der Planeten, was einen starken Einfluss auf die Entstehung und die Eigenschaften der Lücken in Scheiben zu haben verspricht.

Abstract

Protoplanetary disks control the formation and evolution of planets, in reaction the planets also influence the disk structure. Disk gas and dust are the building materials of planets. Tidal forces between planet and disk determine the radial movement of the planet (migration); the planets simultaneously influence the disk, possibly carving out a gap. The interplay between planets and disks is important to understand the variety of exoplanets observed and constrain planet formation theories. This thesis studies new aspects of planet-disk interactions in non-isothermal disks; an important step to a better description of this subject. To this end, radiative-hydrodynamical simulations of planet-disk interactions are performed. Firstly, a Newtonian cooling law is used to investigate the dynamics of vortices, which are generated by the planet and amplified by the convective overstability. The formation of density rings beyond the position of a planetary gap carved out by a high mass planet is studied, as well as the migration rates of low mass planets. Finally, radiative-hydrodynamical simulations are performed. The coupling of radiation transfer to hydrodynamics yields a more accurate determination of the disk temperature in the planet's vicinity, which has a strong influence on the formation and properties of gaps in disks.

Contents

List of figures

List of tables

Chapter 1

Introduction

The concept of heliocentrism was first proposed by the Greek astronomer Aristarchus of Samos in the III century BC, nonetheless his model was forgotten by history. Almost two thousand years later, in the XVI century AD, the astronomer Nicolaus Copernicus came up with a comprehensive mathematical model for the heliocentrism, breaking down the paradigm that the Earth was in the center of the Universe. In the following century, Johannes Kepler advanced Copernicus work, with the Kepler's laws, which describe the motion of the planets using ellipses and can predict how the planet velocities vary. At the same time period, Galileo Galilei was a pioneer for observational Astronomy, improving the telescope invention. With this new tool, he provided observational evidences for Kepler's work. The physical explanation, for the movement of the planets around the Sun, came in the end of the XVII century, with Isaac Newton's book *Philosophiæ Naturalis Principia Mathematica*, where he empirically derived one of the fundamental forces of the Universe – the gravity.

Once the existence of the Solar system was established, the new question humanity started to ask was how this system was formed. The most accepted theory is called the solar nebular hypothesis. This idea was proposed in the XVIII century by Emanuel Swedenborg, followed by further development by Immanuel Kant. Independently, Pierre-Simon Laplace proposed an analogous theory in the end of the XVIII century. The contemporary version of this model is called the solar nebular disk model and was developed by the Soviet astronomer Victor Safronov in the 1970's. The basic idea of this model is that stars are formed through the collapse of dense clumps in giant molecular clouds. As the collapse proceeds the angular velocity increases due to angular momentum conservation. Material collapses more efficiently along the spin axis, therefore a disk is formed around the star's equator. The planets are then supposed to be formed from this dusty gaseous disk. This

model is accepted to be true not only for our Solar system, but to every stellar system in the Universe.

It is fascinating to think that the basic idea of a solar nebular still holds. Certainly, many modifications were made from its original form and a complete model that explains the formation of stellar systems – from the stellar birth to the stellar system settlement – is still needed. Elsasser & Staude (1978) were the first ones to suggest the detection of a circumstellar disk. They showed that the high polarization measurements observed for young stellar objects (YSOs) could be explained by light scattering by dust grains and electrons in a flattened disk around the YSOs. In the following decades, observations ranging from near-infrared to millimeter wavelengths confirmed the existence of such disks. It is expected from statistical analysis that every star should host at least one planet (Youdin, 2011), which is formed out of the circumstellar disk material. The first exoplanet detection was made by Wolszczan & Frail (1992). They showed that the pulsar star PSR1257+12 was orbited by at least two planets, instead of having a second stellar companion. A few years later, Mayor & Queloz (1995) detect a Jupiter-mass planet around the solar-type star 51 Pegasi, using the radial velocity method. The hunting for more exoplanets was followed in the next years using several techniques (e.g., radial velocity, transit observations, microlensing, and direct imaging). Protoplanets and planets strongly interact with the circumstellar disk in which they are embedded. It is not an easy task to explain how these bodies evolve and how they can survive until the stellar disk is evaporated. Therefore, it is of major importance to understand the interplay between planets and their parent disks, which is the focus of this thesis.

In this chapter, a broad introduction to the topic of planet-disk interactions is given. First of all, background to disk formation and evolution is given in Section 1.1. The grounds for planet formation and the diversity of observed exoplanets are discussed in Section 1.2. A description of the current understanding of planet-disk interactions is given in Section 1.3. Finally, the structure of the thesis is summarized in Section 1.4.

1.1 Protoplanetary disks

The classical theory of star formation through the hydrodynamical collapse of a cloud was introduced by Jeans (1902). He derived a critical mass, the Jeans mass, from which the gas pressure cannot balance gravity anymore, the cloud becomes unstable and collapses to form a star. The Jeans mass is much smaller than the average mass of a clump in a molecular cloud. Therefore, additional mechanisms

are necessary to provide support against the gravitational collapse. Otherwise, the star formation rate expected for the Galaxy would have to be much higher than the one observed (Zuckerman & Palmer, 1974). Magnetic fields (Chandrasekhar & Fermi, 1953; Mestel, 1965; Spitzer, 1968; Mouschovias, 1976), rotation (Field, 1978), and turbulence (Norman & Silk, 1980; Larson, 1981) are the common ingredients invoked to solve this problem.

Other problems that rise from the classical theory of star formation are related to the observed angular momentum and magnetic field of young stars. The angular momentum of clumps are much higher than of the young stars. Supposing conservation of angular momentum during the collapse, we would expect the stars to be rotating much faster. Moreover, at some point the stellar spin would be so high that centrifugal forces would stop the collapse. This angular momentum problem was addressed by Mouschovias (1979b) and Mouschovias & Paleologou (1979). Molecular clouds possess magnetic fields and rotation. The magnetic fields lines are twisted due to the cloud rotation. This twist leads to the production of magnetohydrodynamical (MHD) waves. These waves are responsible for the angular momentum transport and this effect is called magnetic braking. With respect to the second problem, the magnetic fields of stars are much smaller than what is expected by conservation of the magnetic flux during the stellar collapse. Once more, Mouschovias (1979a) proposed a solution. If the ionization degree of the clouds decrease, leading to the decoupling of ionized and neutral matter, an effect called ambipolar diffusion, the magnetic flux of the cloud would be redistributed, solving the magnetic flux problem during the stellar collapse.

As more observations were available, the association of outflows and disks to young stars became a fact and the theory of star formation needed more revision (Shu et al., 1987). Disk formation was believed to be a consequence of the angular momentum conservation during a hydrodynamical collapse (Safronov, 1972). The angular momentum lost by the star would be deposited in a disk ranging between 100 and 1000 au (Terebey et al., 1984). This theory would explain why the planets of our Solar system possess almost all the angular momentum of the system. However, as previously touched upon, molecular clouds are magnetized and YSOs do possess magnetic fields. The magnetic braking effect helped to solve the star formation angular momentum transport problem. In the other hand we know, now, that this effect would suppress disk formation, since almost all the angular momentum would be removed by it, preventing the settlement of a disk. This new problem is called the magnetic braking catastrophe (Galli et al., 2006) and some solutions were already proposed. Non-ideal MHD effects, magnetic interchange instability, turbulence, misalignment between the magnetic field and the rotation axis, and

depletion of the envelope by outflow stripping or accretion are good candidates to solve this problem (see Li et al., 2014, for a recent review). Figure 1.1 shows simulations of collapsing disk models, where disk formation is suppressed in the ideal MHD case, but enabled for the turbulent case (Santos-Lima et al., 2012).

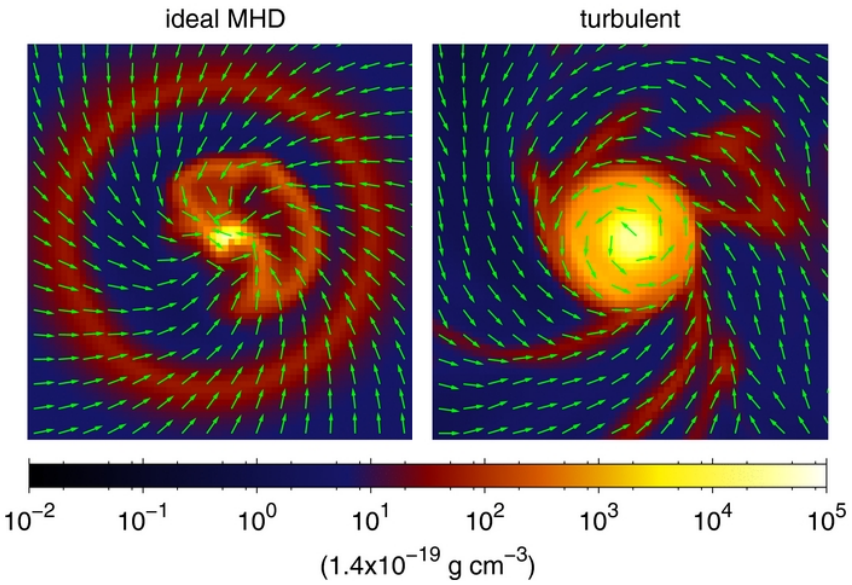

Figure 1.1 Density maps of collapsing disk models after ~ 0.03 Myr. The arrows display the velocity field. Disk formation is suppressed in the ideal MHD case due to magnetic braking, but enabled in the turbulent case. Figure adapted from Santos-Lima et al. (2012).

The presence of disks around YSOs is expected to be observationally detectable for low and intermediate mass stars. High mass stars join the main sequence when they are still accreting. As a consequence, all the information about their birth seems to be lost when they become visible (Shu et al., 1987). Low mass stars ($< 2M_{\odot}$) are called T Tauri stars before joining the main sequence (Joy, 1942, 1945, 1949), whereas intermediate mass stars ($2 - 8M_{\odot}$) are identified as Herbig Ae/Be stars (Herbig, 1960; Strom et al., 1975; Finkenzeller & Mundt, 1984). The first direct observations of circumstellar disks around YSOs were made with the *Hubble Space Telescope* (HST) in the Orion region (O'dell et al., 1993; McCaughrean & O'dell, 1996). At earlier times, indirect evidences were already obtained through infrared excess in spectral energy distributions of T Tauri stars (Mendoza V., 1966, 1968) and optical polarization data (Elsasser & Staude, 1978). Emission from infrared to (sub-)millimiter wavelengths trace the dust grain content, from warm to cold grains. Sub-millimeter observations are sensitive to midplane emission, while scattered light in infrared wavelengths traces small grains in the surface layers of the disk. Lastly, molecular line observations provide insights

to the temperature and kinematic structures of the disk. The infrared satellites *Spitzer Space Telescope* and *Herschel Space Observatory*, new instruments like *Spectro-Polarimetric High-contrast Exoplanet REsearch* (SPHERE) at the *Very Large Telescope* (VLT), and the *Atacama Large Millimeter/submillimeter Array* (ALMA) observatory are revolutionizing our view of circumstellar disks. Recently, several disk structures were revealed through observations, such as azimuthal rings, spirals, and warps. Scattered light images are a powerful technique to reveal disk structures. A beautiful example is the asymmetric features observed in the transition disk of the Herbig Ae star MWC 758. They were modelled as density spiral waves, where each arm of the symmetric two-armed spiral is launched by a massive embedded planet (Benisty et al., 2015), see Figure 1.2. More about transition disks is explained in Section 1.1.2 and about planet induced density spiral waves in Section 1.3.2. These disk structures could be a product of planet-disk interactions. Therefore the interpretation of these recent observations often rely on our understanding of this subject.

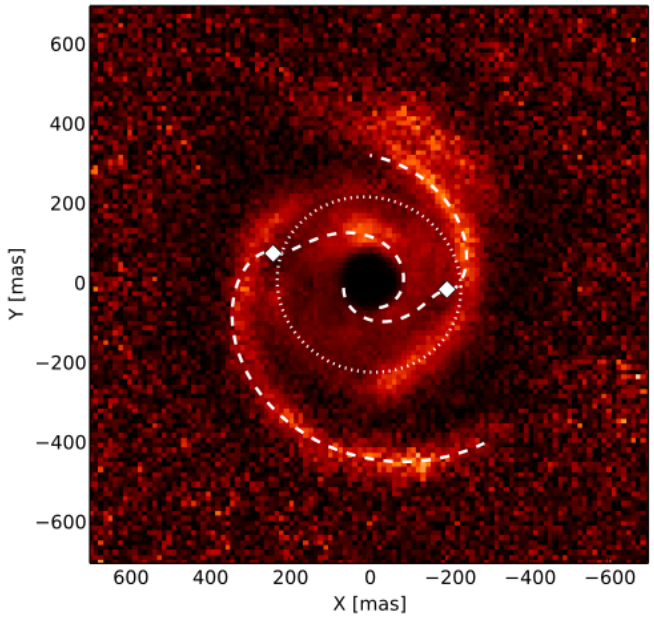

Figure 1.2 Polarized intensity image at 1.04 μm of the transition disk of the Herbig Ae star MWC 758, obtained with SPHERE/VLT. The asymmetric features were modelled as spiral waves induced by two planets. The best-fit model for the spiral waves are shown by the dashed lines. The location of the planets are indicated by the diamonds. The dotted ellipse is a projected circle with 0.25″. Figure from Benisty et al. (2015).

1.1.1 Disk structure

Circumstellar disks are commonly referred to as protoplanetary disks (PPDs), since they are massive enough to form giant planets (Dutrey et al., 2004). Once the gas is settled around the young star, an equilibrium solution for the density, velocity, and temperature structures of the disk can be found. PPDs are also accretion disks. For matter to flow inwards, angular momentum should be transported outwards to keep the angular momentum conservation. The only reason an equilibrium solution can be defined is because the accretion timescales are much longer than the orbital timescales of the disk. Also, for this solution to hold, the stellar-disk system must be located in a low density environment, so that external factors are not important, such as close binary companions or external radiation from massive stars (Armitage, 2013). In this section, the equilibrium solution for the disk structure is presented. The content of this section is based on the book by Armitage (2013).

Density

An expression for the vertical structure of the density can be obtained, assuming that the disk is in vertically hydrostatic equilibrium, so that

$$\frac{dp}{dz} + \rho g_z = 0, \tag{1.1}$$

where p is the pressure, ρ is the density, and g_z is the vertical acceleration. In order to relate pressure with density, an ideal equation of state is considered

$$p = c_s^2 \rho, \tag{1.2}$$

where c_s is the sound speed and the disk is assumed to be vertically isothermal, so that c_s does not depend on z. Now, it is needed to obtain the gravitational vertical acceleration. Considering that the disk mass is much smaller than the stellar mass, so that self-gravity can be neglected, a reasonable assumption for disks with masses up to $\sim 0.1 M_\odot$ (Armitage, 2013). The disk, then, just feels the gravitational force from the star, thus

$$g_z = g \sin\theta = \frac{GM_\star}{(r^2+z^2)} \frac{z}{\sqrt{(r^2+z^2)}}, \tag{1.3}$$

where r is the cylindrical disk radius, z is the disk height above the midplane, g is the gravitational acceleration, θ is the angle from r to z, G is the gravitational constant, and $M_\star$ is the stellar mass. Using Equations 1.2 and 1.3, Equation 1.1

can be written as

$$\frac{d\rho}{\rho} = -\frac{GM_\star z}{c_s^2(r^2+z^2)^{3/2}}dz. \tag{1.4}$$

The integration of Equation 1.4 gives the solution

$$\rho(r,z) = C\exp\left(\frac{GM_\star}{c_s^2\sqrt{r^2+z^2}}\right), \tag{1.5}$$

where C is the integration constant and can be defined, for instance, by the midplane density at the inner disk radius.

Due to the large surface areas, PPDs can cool down very efficiently. Thus, their temperature and pressure are very low. One then need to assume that the disk is thin, meaning that the vertical extent is much smaller than the radial extent ($z << r$). Otherwise, pressure would not be able to counteract gravity and all the matter would fall in to the central star (Armitage, 2013). Under the supposition that $z << r$, the below function can be Taylor expanded

$$(r^2+z^2)^{-1/2} \simeq \frac{1}{r} - \frac{z^2}{2r^3}. \tag{1.6}$$

The Keplerian angular velocity is given by

$$\Omega_K = \sqrt{\left(\frac{GM_\star}{r^3}\right)}. \tag{1.7}$$

Therefore, Equation 1.5 can be written as

$$\rho(z) = \rho(r)\exp\left(-\frac{z^2}{2H^2}\right), \tag{1.8}$$

where $\rho(r)$ is the midplane density and the disk scale height is defined as

$$H \equiv \frac{c_s}{\Omega_K}. \tag{1.9}$$

The radial structure of the density cannot be derived without knowing the nature of angular momentum transport or using observational constraints (Armitage, 2013), but it is often parametrized as a power law of radius

$$\rho(r) \propto r^{-\delta}, \tag{1.10}$$

typical values for the power law are $\delta = 1.0$ or $\delta = 1.5$.

Velocity

The azimuthal velocity of the fluid can be obtained using the Euler equation of conservation of momentum for an inviscid and unmagnetized flow

$$\frac{\partial \mathbf{v}}{\partial t} + (\mathbf{v} \cdot \nabla)\mathbf{v} = -\nabla \Phi_g - \frac{\nabla p}{\rho}, \tag{1.11}$$

where $\mathbf{v}$ is the velocity and Φ_g is the gravitational potential. Assuming a stationary flow, $\partial \mathbf{v}/\partial t = 0$; that the gravitational potential is dominated by the star; considering cylindrical coordinates; and assuming an axisymmetric flow, so that all the components of Equation 1.11, but the radial, vanishes, one gets

$$\frac{v_\phi^2}{r} = \frac{GM_\star}{r^2} + \frac{1}{\rho}\frac{dp}{dr}, \tag{1.12}$$

where v_ϕ is the azimuthal velocity. The Keplerian speed is given by $v_K = \Omega_K r$, therefore

$$v_\phi = \sqrt{v_K^2 + \frac{r}{\rho}\frac{dp}{dr}}. \tag{1.13}$$

The pressure near the midplane usually decreases with radius, thus $dp/dr < 0$, indicating that the flow is sub-Keplerian. If the disk density and temperature structures are known and assuming an equation of state, one can determine the fluid azimuthal velocity by using Equation 1.13.

Temperature

Disk thermal equilibrium is achieved in timescales much shorter than the disk and stellar evolution timescales. Thus, the temperature structure can be set by the balance between cooling and heating. The two main sources of heating are accretion and reprocessing of stellar radiation by dust grains. The cooling comes basically from dust emission.

The temperature structure in a passive disk, where the predominant heating source is irradiation by the star, is determined by the shape of the disk and the mechanism of re-emission of the stellar radiation. The disk shape is dependent on the disk aspect ratio $h = H/r$. Parametrizing the sound speed as

$$c_s(r) \propto r^{-\beta}, \tag{1.14}$$

makes the disk aspect ratio to be

$$h(r) \propto r^{-\beta+1/2}. \tag{1.15}$$

The isothermal sound speed is given by

$$c_s^2 = \frac{k_B T}{\mu m_p}, \tag{1.16}$$

where k_B is the Boltzmann constant, μ is the mean molecular weight, m_p is the proton mass, and T is the temperature. The disk will have a constant aspect ratio when $\beta = 1/2$, therefore a temperature profile

$$T(r) \propto r^{-1}, \tag{1.17}$$

for shallower temperature profiles, $\beta < 1/2$, the disk is flared, so the aspect ratio increases with radius, and for $\beta > 1/2$ the disk is shadowed.

Considering a flared disk, the temperature profile can be derived by evaluating how much stellar radiation can be intercepted by the disk surface at a position r and height H_p above the midplane, Figure 1.3 shows the geometry considered. Assuming that the star is a point source and that the disk surface can see all the stellar surface. The rate of heating per unit disk area can be estimated by the stellar flux absorbed at a distance r and a height H_p[1]

$$\begin{aligned} Q_+ &= 2 \sin \alpha_p \left(\frac{L_\star}{4\pi r^2} \right) \\ Q_+ &\simeq 2\alpha_p \left(\frac{L_\star}{4\pi r^2} \right), \end{aligned} \tag{1.18}$$

where α_p is the angle between the stellar radiation and the tangent to the disk surface at a distance r and height H_p, α_p will be very small at large distances, so that $\sin \alpha_p \sim \alpha_p$; $L_\star$ is the stellar luminosity and the fraction between the parenthesis represents the stellar flux ($F_\star$), so that $\sin \alpha_p F_\star$ is the stellar flux absorbed by the disk surface; the factor two comes from the fact that the disk has two hemispheres, so the midplane temperature at a distance r will be dependent on the radiation absorbed in the upper and lower disk surfaces. Finally, assuming that the disk is vertically isothermal, the temperature at a distance r and height H_p will be the same as the midplane temperature at a distance r.

The cooling rate can be estimated by the dust blackbody radiation flux

$$Q_- = 2\sigma T^4, \tag{1.19}$$

[1] H_p is not the same as H, since absorption is not dependent just on the density, but also on the opacities.

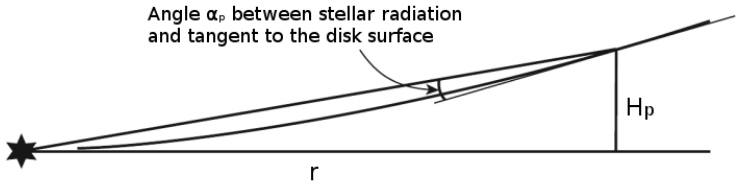

Figure 1.3 This sketch shows the geometry of a flared disk, with the important parameters to estimate the temperature profile. The radiation of the star is absorbed at a distance r and height H_p above the midplane. The angle α_p between the stellar radiation and the tangent to the disk surface is also shown. Figure adapted from Armitage (2013).

where σ is the Stefan–Boltzmann constant; T is the disk temperature, assumed to be the dust blackbody temperature; and the factor two comes again from the fact that the disk has two hemispheres.

The temperature structure can be obtained by imposing the balance between heating and cooling

$$T(r) = \left(\frac{L_\star}{4\pi\sigma}\right)^{1/4} \alpha_p^{1/4} r^{-1/2}$$
$$T(r) = \left(\frac{R_\star}{r}\right)^{1/2} \alpha_p^{1/4} T_\star, \tag{1.20}$$

with the stellar luminosity given by

$$L_\star = 4\pi R_\star^2 \sigma T_\star^4, \tag{1.21}$$

where $R_\star$ is the stellar radius and $T_\star$ is the effective stellar temperature.

Chiang & Goldreich (1997) obtained a good estimate for the angle α_p. Considering that the star has a finite size, their expression is given by

$$\alpha_p \simeq 0.4\frac{R_\star}{r} + r\frac{d(H_p/r)}{dr}. \tag{1.22}$$

This estimate for the temperature structure for flared disks was firstly put forward by Kenyon & Hartmann (1987). They also observed that at large radii the surface temperature is well approximated by

$$T(r) \propto r^{-1/2}. \tag{1.23}$$

1.1.2 Disk evolution

Protoplanetary disks have a lifetime of a few million years. Infrared excess observations suggest that thin disks have a longer lifetime than massive disks (Aumann,

1985). PPDs lose their mass as they evolve, indicating that the massive disk phase ends quickly and most of the disk lifetime is spent in the thin disk phase (Dutrey et al., 2004). Figure 1.4 shows a diagram with the four main phases of disk evolution. As previously touched upon, PPDs are also accretion disks. This physical process controls the dynamical evolution of disks in their massive and thin disk phases. Therefore, it is of extremely importance to understand how PPDs can transport their angular momentum. In the latest phases of disk evolution, most of its gas was already lost. Thus, it is needed to understand which processes lead to gas dispersal. In this section disk evolution is discussed. Most of the content is based on the book by Armitage (2013).

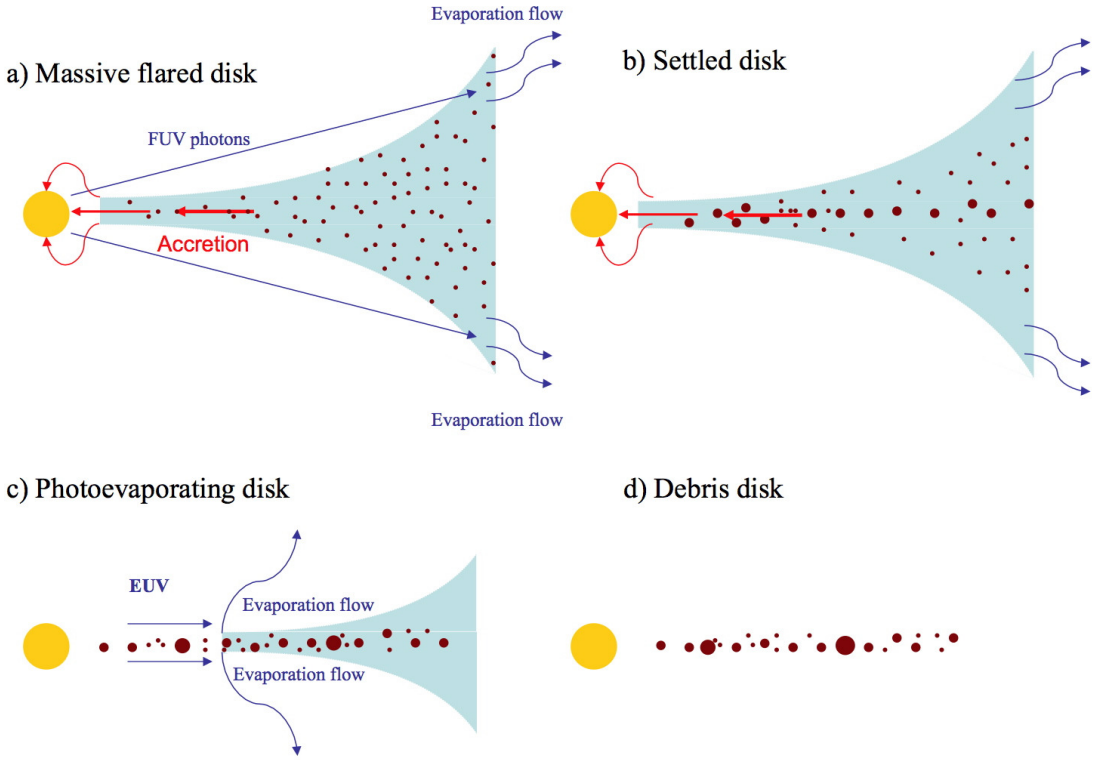

Figure 1.4 This diagram shows the four main phases of disk evolution. Figure from Williams & Cieza (2011).

Young disks

The evolution of young disks relies in angular momentum transport. Considering a thin disk ($h << 1$), the two main forces at play are rotational support and gravity. Assuming that the potential is not time-dependent, the only way to change the disk surface density is via angular momentum transport. When a gas parcel loses angular momentum, it will spiral towards the central star, which we call accretion.

On the other hand, this angular momentum should be given to a gas parcel in an outer radius, therefore moving it outwards; or this angular momentum should somehow be lost. The classical theory of angular momentum transport in accretion disks was developed by Shakura & Sunyaev (1973) and Lynden-Bell & Pringle (1974). Their theory prescribes that angular momentum is redistributed in the disk due to a turbulence-driven viscosity. Another way to explain accretion is via angular momentum loss by magnetically driven outflows and disk winds (e.g., Shu et al., 2007).

Considering the Navier-Stokes equations for a viscous fluid in cylindrical coordinates and imposing angular momentum conservation, it can be demonstrated that the surface density evolution for an accretion disk is governed by (e.g., Lynden-Bell & Pringle, 1974)

$$\frac{\partial \Sigma(r,t)}{\partial t} = \frac{3}{r}\frac{\partial}{\partial r}\left[r^{1/2}\frac{\partial}{\partial r}(\nu \Sigma r^{1/2})\right], \tag{1.24}$$

where ν is the kinematic viscosity. Equation 1.24 is a diffusive partial differential equation, which is linear when ν is not dependent on Σ. The steady-state solution ($\partial\Sigma/\partial t = 0$) for Equation 1.24, assuming Keplerian motion and constant accretion rate ($\dot{M}$), is given by

$$\nu\Sigma = \frac{\dot{M}}{3\pi}\left(1 - \sqrt{\frac{R_\star}{r}}\right). \tag{1.25}$$

The temperature profile of active disks, where accretion is important, can be derived by considering the transport of energy by the viscous torque and the gas energy losses by radiation. Assuming Keplerian motion and the solution for the surface density given by Equation 1.25, it can be showed that the temperature profile is given by

$$T(r) = \left[\frac{3GM_\star\dot{M}}{8\pi\sigma r^3}\left(1 - \sqrt{\frac{R_\star}{r}}\right)\right]^{1/4}. \tag{1.26}$$

Meaning that for positions far from the inner boundary ($r >> R_\star$), the temperature profile of active disks is given by

$$T(r) \propto r^{-3/4}. \tag{1.27}$$

It is interesting to notice that the temperature profile is not directly dependent on the viscosity; however, indirectly, viscosity remains important, since it is essential to determine the surface density profile and the timescales of disk evolution, which is given by (Armitage, 2013)

$$\tau_\nu \simeq \frac{r^2}{\nu}. \tag{1.28}$$

In order to understand the evolution of thin young disks, one need to comprehend the viscosity origin. A common approach is to use the Shakura & Sunyaev (1973) α-prescription, where viscosity is a turbulent-driven quantity given by

$$\nu = \alpha c_s H. \tag{1.29}$$

The α-value gives the turbulence strength. A classical theory is that turbulence is composed by eddies (Kolmogorov, 1941). The energy flows in cascade from large to small scales. The maximum eddy size is of the order of one scale height, whereas the minimum size is given by the Kolmogorov length scale, from which energy is then thermally dissipated. Several physical instabilities may produce turbulence. The common invoked mechanism for PPDs is called the magnetorotational instability (MRI, Balbus & Hawley, 1991). Nonetheless, for magnetic inactive regions, other mechanisms must be at play. In PPDs, there is a large region called the dead zone (Gammie, 1996), where MRI cannot be active. Hydrodynamical instabilities may also produce turbulence that is strong enough to explain angular momentum transport. The Rossby wave instability (RWI, Lovelace et al., 1999; Li et al., 2000) and the baroclinic instability (BI, Klahr & Bodenheimer, 2003) are good candidates. More about these instabilities will be discussed in Chapter 2 and Chapter 3.

Transition disks

Some disks present a large amount of mid-infrared excess; however, they lack of near-infrared excess, suggesting an inner hole. Such systems are called transition disks. The timescale for the dispersal phase is in the order of about 10^5 yr (Simon & Prato, 1995; Wolk & Walter, 1996). The short timescale for the depletion of the inner disk cannot be explained solely by accretion. Photoevaporation is an additional mechanism that play an important role during this phase of disk evolution (e.g., Owen et al., 2010, 2011). Ultraviolet and X-ray radiation heat the disk surface layers to high enough temperatures, so that the flow can escape the gravitational potential and disperse as a thermal wind (Armitage, 2013). Observational evidence of this process was firstly obtained in the Orion nebula cluster, where photoevaporative flows were associated to young stars with disks (O'dell et al., 1993; Johnstone et al., 1998). The ultraviolet radiation field comes mostly from close massive stars, but even weaker ultraviolet radiation from low mass stars would be sufficient to provide disk photoevaporation in the expected timescales (Armitage, 2013). The inclusion of photoevaporation into the disk evolution equation is rather easy. Its effects can

be captured by adding a simple mass sink in the disk evolution equation

$$\frac{\partial \Sigma(r,t)}{\partial t} = \frac{3}{r}\frac{\partial}{\partial r}\left[r^{1/2}\frac{\partial}{\partial r}(\nu\Sigma r^{1/2})\right] + \dot{\Sigma}_{wind}(r,t), \tag{1.30}$$

where the mass loss term ($\dot{\Sigma}_{wind}$) is specified by assuming a model for the photoevaporation process.

There are three phases in the evolution of PPDs with accretion and photoevaporation included (Clarke et al., 2001; Alexander et al., 2006). Firstly, the mass loss due to photoevaporation is negligible and the disk evolves due to the viscous angular momentum transport. At some point, the mass loss rate due to accretion drops to a comparable value to the photoevaporation one. The mass flowing from the outer disk is lost by a thermal wind, instead of reaching the inner disk. This process opens an annular gap and the inner material is accreted by the star in the viscous timescale, which then lasts for $\sim 10^5$ yr. These inner holes were observationally confirmed by direct imaging at millimeter wavelengths (Hughes et al., 2009; Brown et al., 2009; Andrews et al., 2011). The inner disk eventually becomes optically thin to the stellar extreme ultraviolet flux. Thus, this radiation will directly hit the inner edge of the outer disk, which increases the photoevaporation mass loss rate. The entire outer disk is then dispersed on a timescale of a few 10^5 yr.

Debris disks

Debris disk is the last phase of disk evolution, when dust grains and small bodies (planetesimals) dominate the disk content. Saturn's ring is a good example of what a stellar debris disk should look like. These systems are a good indirect evidence of planet formation and can be used to learn more about the diversity of planetary systems (e.g., Su et al., 2005; Raymond et al., 2011). They can be detected by an infrared excess flux in the spectral energy distributions of stars. The first detection was made using *InfraRed Astronomical Satellite* (IRAS) data of the Vega star (Aumann et al., 1984). Debris disks can be found around young stars, but also main sequence stars, and even one detection was reported around a neutron star (Wang et al., 2006). The most famous debris disk is the one around β Pictoris (Smith & Terrile, 1984). The presence of planets, star companions, or close stars can perturb the disk, increasing the collision velocities of dust grains and planetesimals (Kenyon & Bromley, 2002, 2004). These collisions can brake down dust grains to smaller sizes, that later can be expelled from the system by radiation pressure. Nonetheless, such collisions are also important to replenish the

disk content, grind down big bodies to smaller sizes, allowing the debris phase to last for longer lifetimes.

1.2 Planets

Planets are formed out of the protoplanetary disks of gas and dust around young stars. Dust particles of micron-meter sizes are the building material for objects of about 10 km in radius. These objects are called planetesimals and in order to form them, the dust grains have to grow through 10 orders of magnitude in size. The formation of planetesimals, which subsequently lead to the formation of terrestrial and giant planets, is currently a hot topic. In this section, the current planet formation scenarios and their problems are briefly introduced. Later, the diversity of planets that have been observed is mentioned. This section is based on the book by Armitage (2013).

1.2.1 Planetesimal formation

Dust particles embedded in a gaseous disk experience aerodynamic forces. Such forces influence how these particles move through the disk and therefore are important for their evolution. There are two types of drag, the Epstein drag (Epstein, 1924) is felt by particles with smaller sizes than the mean-free path of gas molecules within the disk, whereas the Stokes drag (Whipple, 1972) is felt by particles with larger sizes. Besides the aerodynamic drag, the dust particles also feel the stellar gravity. The vertical component of the gravity pushes dust particles towards the midplane, an effect called dust settling (e.g., Weidenschilling, 1997). The sub-Keplerian gas motion leads to a radial drift (Weidenschilling, 1977). Small particles are normally well coupled to the gas, thus they move with a sub-Keplerian azimuthal velocity. Since the particles do not feel the gas pressure, the centrifugal force is not sufficient to balance gravity, so the particles spiral inwards towards the central star. Larger particles are usually decoupled from the gas and move on Keplerian orbits. The fact that these solid bodies possess an azimuthal velocity faster than the gas, makes them to feel a headwind that removes some of their angular momentum, also leading them to move inwards towards the central star.

Relative velocities between dust particles make them to collide. Brownian motion is the main driver for the collisions of small grains, since it leads to random velocities between the small particles due to the thermal motion of the gas. Nevertheless, particles of all sizes should have relative velocities due to their difference in sizes. Turbulence can also change the velocity of particles because of diffusion. The

common theory for planetesimal formation is via dust coagulation. This model relies in the fact that dust aggregates may stick together after colliding. The problem is that the outcome of a collision may be that the involved dust aggregates fragment or bounce, i.e. they collide without sticking together or fragmenting. Therefore, the sticking efficiency must be high to allow planetesimal formation. How to form planetesimals via the growth of dust aggregates is one of the major problems of planet formation.

The dust aggregates should also overcome three growth barriers. The bouncing barrier (Zsom et al., 2010) acts on dust aggregates of about millimeter-sizes. Basically, their low relative velocities lead to elastic collisions, where sticking is not possible. The dust aggregates just rebound and do not grow further. This barrier is predominant in the inner parts of the disk. The fragmentation barrier (Dullemond & Dominik, 2005) is an issue for centimeter-size aggregates at a few *au*. In this case, high velocity collisions are disruptive and fragment the dust aggregates, instead of allowing them to grow. The last growth barrier is called the radial drift barrier (Whipple, 1972). The problem here is that dust aggregates drift to inner regions in timescales faster than the one which allow them to grow. This barrier is predominant in outer parts of the disk, where the drift timescales are larger.

It is clear that dust aggregates can grow up to centimeter-sizes. However, how to form planetesimals, which are well beyond these sizes, is still under debate. Several theories were proposed in the past years. Here, some of them are mentioned, without going into details. One possibility is that planetesimals are formed in pressure bumps (e.g., Whipple, 1972; Barge & Sommeria, 1995; Klahr & Henning, 1997). Particles can be efficiently trapped in these locations, and their collision rate may increase there, favouring coagulation. Planetesimal formation through a streaming instability is another channel (Johansen et al., 2007). Local enhancements of gas-to-dust mass ratios are caused due to the dust aggregates' drag. This enhancements have Keplerian velocity, thus as they move they grab particles with smaller velocities than the Keplerian. Once enough material is accumulated, the clump may get gravitationally unstable and collapse, forming planetesimals. Sweep-up growth is a third possibility to form planetesimals (Windmark et al., 2012). This model relies in the fact that the collision of a large particle with another with much smaller size will lead to the fragmentation of the smaller particle, but growth of the bigger. Since part of the fragments of the small particle may stick to the bigger one. The efficiency of this process is that about 1% of dust particles are turned to planetesimals (Drążkowska et al., 2013, 2014).

1.2.2 Terrestrial planet formation

The next step, after the formation of planetesimals, is to form terrestrial planets with radii of several thousands of kilometers. The gravitational force starts to play a role for bodies of this size. Thus, once a large number of planetesimals are formed, their interactions start to be dominated by gravity. The random velocity between these bodies is set by the balance between viscous stirring among themselves and damping due to aerodynamic drag. The cross section for collisions is dependent on the planetesimal mass. Therefore, the most massive bodies undergo collisions more often, increasing their mass much faster. This process is called runaway growth (Wetherill & Stewart, 1989; Kokubo & Ida, 1996) and it is terminated once the viscous stirring produced by a large body overtakes the self-stirring among the planetesimals. At this stage, an oligarchic growth (Kokubo & Ida, 1998) begins, where the largest body gets even more massive by the capture of smaller bodies from its feeding zone. These stages last for ~ 0.01 to 1 Myr, when several oligarchs may be formed in different locations of the disk. These protoplanets can achieve masses ranging from the Moon's mass to Mercury's mass. These oligarchs largely deplete the planetesimals disk, to the point that dynamical friction is no longer able to sustain their low eccentricities and inclinations. Therefore, these large blocks start to strongly interact via collisions. The terrestrial planets are formed as a product of these collisions. This stage is rather slow, lasting for at least 10 Myr, and extremely chaotic, the same initial conditions can lead to a large variety of planetary systems (e.g., Raymond et al., 2006; O'Brien et al., 2006).

1.2.3 Giant planet formation

There are two different accepted theories for the formation of gaseous giant planets: core accretion and gravitational instability. In the core accretion (Pollack et al., 1996) scenario, giant planets are formed in two stages. The assembly of a solid core followed by gas accretion, which builds up a thick atmosphere using the gaseous disk reservoir. The solid core is formed as a product of the collisions of protoplanets, exactly as in the terrestrial planet model. The core possess an envelope, which is initially in hydrostatic equilibrium. Further growth of the planet core and its envelope is governed by the cooling properties of the envelope. The energy liberated through the collision with planetesimals and the gravitational energy released by the contraction of the envelope should be transported through the envelope by convection or radiative diffusion, before being deposited in the stellar disk. The planet core and its envelope undergo hydrostatic growth until a critical mass ($\sim 10 M_{\oplus}$) is achieved. If by this time, the gaseous disk was not yet

dissipated, the interaction of the planet core with the disk leads to a hydrodynamical instability (Perri & Cameron, 1974; Mizuno, 1980) that results in a runaway growth of the planet's atmosphere, due to rapid gas accretion. This phase lasts for about 10^5 yr and planets with Jupiter's or Saturn's masses can be easily formed. The gas accretion phase is stopped, when the gaseous disk reservoir is gone, or if the planet carves out a gap, becoming isolated from the stellar disk.

Another channel to form giant planets is via gravitational instability (Kuiper, 1951; Cameron, 1978). The disk should be massive enough to become unstable due to its own self-gravity. The Toomre criterion (Toomre, 1964) for a disk to be gravitationally unstable is

$$Q \equiv \frac{c_s \Omega}{\pi G \Sigma} \lesssim 1. \tag{1.31}$$

This criterion requires rather high surface densities, more than one order of magnitude higher than the minimum mass Solar Nebula (Armitage, 2013). As discussed in Section 1.1.2, young stars are expected to have massive disks in the very early stages of their evolution (e.g., Eisner et al., 2005). Therefore, the formation of planets through gravitational instability is possible; however, this process is able to form only very massive planets, of at least a few Jupiter masses, and in the early stages of the disk lifetime. Another possibility is that gravitational instability may produce high mass planets at very large radii, where the disk mass is high enough. The fulfillment of the Toomre criterion is not sufficient for the formation of planets. The gravitational instability may just lead to the formation of spiral waves that are able to transport angular momentum outwards, inducing inward accretion. Fragmentation is another required condition for disks to form planets through the action of the gravitational instability. The disk should be able to efficiently radiate its thermal energy for fragmentation to occur. The cooling timescale has to be shorter than one orbital period (Shlosman & Begelman, 1989). Otherwise a clump would have a chance to collide with other clumps and generate more heating, instead of cooling down and fragment into a dense clump, that might form a massive planet or even a brown dwarf. This theory was already verified by simulations (e.g., Boss, 1997; Rice et al., 2003).

1.2.4 Observations of planets

It is expected that every star should host at least one planet (Youdin, 2011), meaning a minimum of 100 billion planets living in our Milky Way. The discovery of the first exoplanet was announced in 1992 (Wolszczan & Frail, 1992), since then, more than a thousand exoplanets were detected. The *Kepler Space Telescope* is responsible for the majority of these discoveries (Batalha et al., 2013). Several interesting objects

were found amongst these exoplanets, such as hot Jupiters and super-Earths. On the other hand, no Earth twins were yet announced. The hot Jupiters are a class of planets with similar sizes as Jupiter, but orbiting very close to the host star, which lead to very high surface temperatures. The super-Earths are a class of planets with masses higher than the Earth, but smaller than $\sim 10 M_{\oplus}$, also usually orbiting close to the parent star. An Earth twin would be a planet with very similar properties as our Earth, such as mass, radius, density, and composition. There are five most known methods to detect exoplanets: radial velocity, transit observations, microlensing, direct imaging, and astrometry. The first two are more sensitive to massive planets orbiting close to the star, whereas the last three are good to detect planets orbiting at larger distances from the host star. These techniques should be complementary and cover the whole planet's parameter space; however, they are usually applied to different samples of stars (Fischer et al., 2014).

Figure 1.5 shows a plot of planet mass vs. planet semimajor axis. The plot is color coded based on the planet orbital eccentricity. One would expect that exoplanets should have very low eccentricities, as the planets from our Solar system. Nonetheless, a large number of planets present quite high eccentricities, with a median value of ~ 0.3 (Takeda & Rasio, 2005). Planets seem also to present a broad distribution of inclinations. The measurement of the Rossiter McLaughlin effect in hot Jupiters have shown orbits highly misaligned with the star's equatorial plane (Albrecht et al., 2012) and that about 25% of hot Jupiters are orbiting in retrograde direction (Triaud et al., 2010). More about this topic is discussed in Section 1.3.3.

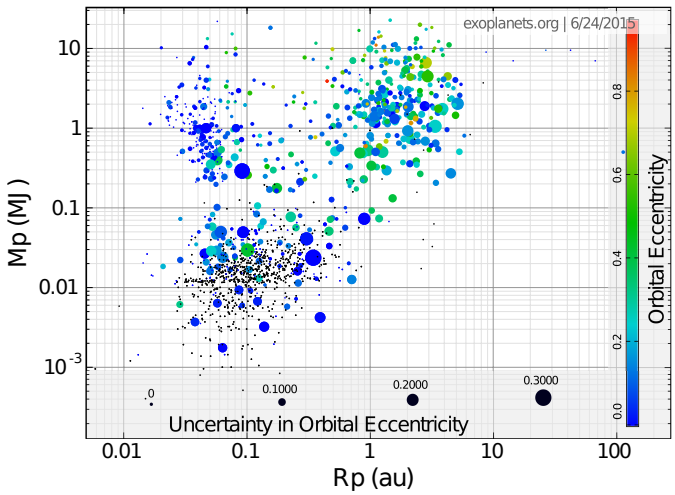

Figure 1.5 Planet mass in Jupiter masses vs. planet semimajor axis. The color bar represents the orbital eccentricity of the planets, the circle's size is scaled to the uncertainty of the measurement. Figure produced with the exoplanet.org plotter.

1.3 Planet-disk interactions

The study of planet-disk interactions is of major importance for the understanding of planetary systems. In Section 1.2.4, the large variety of exoplanets, that were found in the past two decades, was briefly mentioned. The gravitational forces between forming planets and their parent disks controls the evolution of the planet's orbital elements (eccentricity and semi major axis) before the protoplanetary disk dispersal (Baruteau et al., 2014). The planet acts as a perturbation in the disk, and depending on its mass, it influences the disk structure in different ways. The torque exerted by the disk on the planet changes the planet angular momentum. The planet's orbital elements depend on the planet specific angular momentum.

Simulations of planet-disk interactions basically measure these torques, thus one can predict the planet's orbital parameters. In order to pursue such simulations, one need to know the disk structure. In Section 1.1, the physics of protoplanetary disks was revised, where all the necessary assumptions about disk structure are justified. After disk dispersal, planet-planet and star-planet interactions may reshape planetary systems (Baruteau et al., 2014). Therefore, one need to comprehend all these three processes to be able to explain all sorts of planetary systems that are being observed. This thesis is concentrated on the subject of planet-disk interactions. Most of the studies in this subject are applied to the evolution of the planet semi major axis, a process called as migration. In the following sections, it is described how to simulate a planet-disk system. A summary of the current status of this area is also given. This section is based on the review by Baruteau et al. (2014).

1.3.1 Numerical simulations of planet-disk interactions

The most common way of studying planet-disk interactions is via numerical simulations. Several physical phenomenons are involved, such as hydrodynamics, gravity, magnetic fields, heating from viscous processes and radiation, cooling from dust radiation, gas dispersal via photoevaporation, N-body dynamics, and possibly more phenomenons. Unfortunately, to date it is not feasible to consider all the physics involved, thus one should know the most important ingredients for different situations.

In the simulations presented in this thesis, the dust component is considered only as a source of radiation, no dust feedback to the gas or its gravitational interaction with the planet is included. The justification is that the gravitational interaction between the dust and the planet should not play a major role, since the dust is a small fraction of the gas component $\sim 1\%$. Thin disks with Toomre parameters

$Q >> 1$ are considered, thus the disk self-gravity can be neglected. Magnetic fields were disregarded, this assumption can be justified by the fact that there is a large fraction in the midplane of the protoplanetary disk that is magnetically dead, the so-called dead zone (Gammie, 1996). Photoevaporation was not included, since it should not play a major role for fairly young thin disks. Finally, a single planet was assumed, thus no N-body dynamics from multiple planets is involved. The focus of this work is to study planet-disk interactions considering the thermal structure of the disk. Therefore, the gas hydrodynamics, the planet and stellar gravities, and heating and cooling processes are the important ingredients.

The PLUTO code (Mignone et al., 2007) was used, which is a finite-volume Godunov-type code, designed to integrate a system of conservation laws. In a first part of this work, the thermal structure of the disk evolves based on a Newtonian cooling approach, which is described in Chapter 2. In a second part, stellar and dust radiations were included, thus the disk thermal structure is evolved in a more consistent manner. For this purpose, radiation transport had to be carried together with hydrodynamics. Hereafter, the concepts involved on the hydrodynamics and radiation transport are briefly described.

Hydrodynamics

The hydrodynamical (HD) module of the PLUTO code is used to evolve the gas quantities in time. The Euler equations for compressible fluids in the conservative form are considered. The conservation of mass is described by the continuity equation

$$\frac{\partial \rho}{\partial t} + \boldsymbol{\nabla} \cdot (\rho \mathbf{v}) = 0, \tag{1.32}$$

where $\mathbf{v}$ is the gas velocity vector. The momentum conservation is described by the equation of motion

$$\frac{\partial \mathbf{v}}{\partial t} + (\mathbf{v} \cdot \boldsymbol{\nabla})\mathbf{v} = -\frac{1}{\rho}\boldsymbol{\nabla} p - \mathbf{a}, \tag{1.33}$$

where $\mathbf{a} = \sum_i \mathbf{a_i}$ is an acceleration term that accounts for additional physics, such as gravity, dust radiation, and stellar feedback. The energy conservation is described by the energy equation

$$\frac{\partial E}{\partial t} + \boldsymbol{\nabla} \cdot ((E + p)\mathbf{v}) = \rho \mathbf{v} \cdot \mathbf{a} - \boldsymbol{\nabla} \cdot \mathbf{F_{TR}}, \tag{1.34}$$

where E is the total gas energy density and $\mathbf{F_{TR}} = \mathbf{F_R} + \mathbf{F_\star}$ is the flux of the total radiation density energy, which is introduced in the following section. An ideal

equation of state was chosen to close this system of equations

$$p = (\gamma - 1)\rho\Big(E - \frac{1}{2}\rho v^2\Big), \tag{1.35}$$

where γ is the adiabatic index (specific heat ratio) and the term in between parenthesis in the right hand-side is the internal energy, thus the total gas energy subtracted by the kinetic energy.

In order to model a planet-disk system, one needs to include the gravitational forces from the central star and from the planet, which is done by setting $\mathbf{a_1} = \boldsymbol{\nabla}\Phi_g$, where Φ_g is the gravitational potential from the star and the planet. The implementation of this body force was done by Uribe et al. (2011), which is called the planet-disk PLUTO module. In this new module, the planet equations of motion are also evaluated, which takes into account the gravitational interaction of the planet with the disk and the star. Therefore, the planet is allowed to move through the disk. In Chapter 2 the planet-disk module is described in more details. The specification of the numerical schemes used to integrate the above equations in space and time is given in Chapter 2. A Newtonian cooling approach was used to evaluate the disk temperature structure in Chapters 2 and 3. More details about this procedure can be found in Chapter 2. In Chapter 4, radiation physics was considered to evaluate the disk temperature structure. Hereafter, the treatment of the radiation transport is briefly described.

Radiation transport

The irradiation of the star is an important heating source for the gas. The dust thermal emission can heat the gas as well, but it is mainly the most important source for cooling. Therefore, the consideration of radiation transport is of extreme importance to properly treat the disk thermal structure. The radiation transport module for the PLUTO code developed by Kuiper et al. (2010) was used, which considers a gray flux limited diffusion (FLD) approximation combined with a frequency dependent ray-tracing to solve the radiation transport. Details about the numerical methods and the derivation of the equations can be found in Kuiper et al. (2010).

First of all, the stellar irradiation flux is calculated using the ray-tracing method. For that, an opacity table is used, which has a fixed number of bins, where each bin is characterized by its central value (ν_i). The stellar irradiation flux is given by

$$\mathbf{F}_\star(r,\nu) = \mathbf{F}_\star(R_\star,\nu)\left(\frac{R_\star}{r}\right)^2 e^{-\tau(r,\nu)}, \tag{1.36}$$

where $\mathbf{F}_\star(R_\star, \nu)$ is the boundary flux at the stellar surface and $\tau(r, \nu)$ is the optical depth. The stellar boundary flux can be calculated by integrating the Planck function over the frequency bin interval

$$\mid \mathbf{F}_\star(R_\star, \nu) \mid = \frac{c}{4} \int_{(\nu_{i-1}+\nu_i)/2}^{(\nu_i+\nu_{i+1})/2} B_\nu(\nu, T_\star) d\nu, \tag{1.37}$$

where c is the speed of light. The optical depth is given by

$$\tau(r, \nu) = \int_{R_\star}^{r} \kappa(\nu)\rho(r) dr, \tag{1.38}$$

where $\kappa(\nu)$ is the dust opacity. This method neglects scattering, therefore it assumes that the stellar irradiation always travels away from the central star in the radial direction and it is only allowed to be absorbed.

The dust radiation flux is then computed using the FLD approximation. Assuming that the dust temperature is in equilibrium with the total radiation field (stellar and diffusive radiation fields), one gets

$$aT^4 = E_R + \sum_{\nu_i} \frac{\kappa(\nu_i)}{\kappa_P(T)} \frac{\mid \mathbf{F}_\star(r, \nu_i) \mid}{c}, \tag{1.39}$$

where a is the radiation constant, E_R is the dust radiation energy density, $\kappa_P(T)$ is the Planck mean opacity for a temperature T, and assuming thermal equilibrium, $T_{dust} = T_{gas} = T$.

The evolution of the radiation energy density is given by

$$\frac{\partial E_R}{\partial t} = -f_c(\boldsymbol{\nabla} \cdot \mathbf{F_R} + \boldsymbol{\nabla} \cdot \mathbf{F}_\star - Q^+), \tag{1.40}$$

where f_c is a coefficient that depends on the ratio between internal and radiation energies, $\mathbf{F_R}$ is the flux of the radiation energy density, and Q^+ is a source term that depends on the gas dynamics (viscous heating, accretion luminosity, etc). The coefficient f_c is given by

$$f_c = \left(\frac{c_V \rho}{4aT^3} + 1 \right)^{-1}, \tag{1.41}$$

where c_V is the specific heat capacity. The flux of the radiation energy density is given by

$$\mathbf{F_R} = -\frac{\lambda c}{\kappa_R \rho} \boldsymbol{\nabla} E_R, \tag{1.42}$$

where λ is the flux limiter and k_R is the Rosseland mean opacity. The source term from the hydrodynamics is given by

$$Q^+ = -p\boldsymbol{\nabla}\cdot\mathbf{v}. \tag{1.43}$$

Equation 1.39 is used to obtain the radiation energy density using the current temperature. The radiation energy density for following timesteps is then obtained through the integration of Equation 1.40. In order to solve this equation, one needs to know the flux of the radiation energy density, which is calculated using the FLD approximation to solve Equation 1.42. The new temperature distribution is then obtained through Equation 1.39. This process is called an iterative Newton-update, since it re-uses the equation from which the radiation energy density was firstly obtained, to later determine the temperature. One important thing to mention is that Equation 1.34 is used to determine the hydrodynamical source term Q^+ and not to evolve the temperature. The temperature evolution is obtained as just mentioned.

The additional acceleration terms for the HD equations are then given by

$$\begin{cases} \mathbf{a_2} = -\dfrac{\boldsymbol{\nabla}\cdot\mathbf{F}_\star}{c\rho}\hat{\mathbf{e}}_\mathbf{r}, & (1.44) \\ \mathbf{a_3} = -\dfrac{\lambda}{\rho}\boldsymbol{\nabla}E_R, & (1.45) \end{cases}$$

where $\mathbf{a_2}$ accounts for the stellar feedback and $\mathbf{a_3}$ for dust radiation.

1.3.2 Low mass planets

Low mass planets of a few Earth masses exert a small perturbation in their parent disks, thus the disk density structure remains mostly unchanged. Since the planet induces just a small perturbation in the velocity ($\mathbf{v_1} = \mathbf{v} - \mathbf{v_0}$) and the pressure ($p_1 = p - p_0$), where $\mathbf{v_0}$ and p_0 are the unperturbed velocity and pressure, one can use linear perturbation analysis to find a solution for the disk structure. Tanaka et al. (2002) solved this problem for three-dimensional (3D) isothermal disks. A perturbation $\eta = p_1/\rho_0$ is introduced, which is equivalent to an enthalpy perturbation, with ρ_0 being the unperturbed density. Before obtaining the perturbation equations, the enthalpy, velocity, and planet gravitational potential are expanded into Fourier series

$$X = \sum_m Re[X_m e^{im(\phi-\Omega_p t)}], \tag{1.46}$$

where X is the quantity to be expanded, m is the Fourier wave number, ϕ is the azimuthal angle from cylindrical coordinates, and Ω_p is the planet angular velocity.

Substituting the Fourier components (X_m) in Equations 1.32 and 1.33 gives

$$im(\Omega-\Omega_p)v_{1,r,m}-2\Omega v_{1,\phi,m}=-\frac{\partial\eta'_m}{\partial r}-\frac{2\beta}{r}\eta_m, \tag{1.47}$$

$$im(\Omega-\Omega_p)v_{1,\phi,m}-2Bv_{1,r,m}=-\frac{im\eta'_m}{r}, \tag{1.48}$$

$$im(\Omega-\Omega_p)v_{1,z,m}=-\frac{\partial\eta'_m}{\partial z}, \tag{1.49}$$

$$\begin{aligned} im(\Omega-\Omega_p)\frac{\eta_m}{c_s^2}+\frac{\partial v_{1,r,m}}{\partial r}+\frac{\partial\ln(r\rho_0)}{\partial r}v_{1,r,m}\\ +\frac{im}{r}v_{1,\phi,m}+\frac{\partial v_{1,z,m}}{\partial z}-\frac{z}{H^2}v_{1,z,m}=0, \end{aligned} \tag{1.50}$$

where (r,ϕ,z) are the cylindrical coordinates, Ω is the unperturbed disk angular velocity, $\eta'_m=\eta_m+\phi_{p,m}$, β is the negative sound speed exponent, and $B=\Omega+r(\partial\Omega/\partial r)/2$ is the Oort parameter. Eliminating $\mathbf{v_{1,m}}=(v_{1,r,m},v_{1,\phi,m},v_{1,z,m})$ from Equations 1.47 to 1.50, leads to a wave equation for η'_m

$$\begin{aligned} \frac{\partial^2\eta'_m}{\partial r^2}+D'_r\frac{\partial\eta'_m}{\partial r}+\left(\Omega'_rD'_r-\frac{m^2}{r^2}-\frac{D}{c_s^2}\right)\eta'_m\\ +\frac{2\beta}{r}\left\{\frac{\partial}{\partial r}-\Omega'_r+D'_r\right\}\times(\eta'_m-\phi_{p,m})\\ +\frac{D}{m^2(\Omega-\Omega_p)^2}\left[-\frac{\partial^2\eta'_m}{\partial z^2}+\frac{z}{H^2}\frac{\partial\eta'_m}{\partial z}+\frac{1}{\Omega-\Omega_p}\left(\frac{\partial\Omega}{\partial z}\right)\frac{\partial\eta'_m}{\partial z}\right]=\\ -\frac{D}{c_s^2}\phi_{p,m}, \end{aligned} \tag{1.51}$$

where

$$\begin{cases} D'_r=\dfrac{\partial\ln(r\rho_0/D)}{\partial r}, & (1.52)\\ \Omega'_r=\dfrac{2\Omega}{r(\Omega-\Omega_p)}, & (1.53)\\ D=4B\Omega-m^2(\Omega-\Omega_p)^2. & (1.54) \end{cases}$$

The amplitude of the wave η'_m diverges when (i) $4B\Omega-m^2(\Omega-\Omega_p)^2=0$ and (ii) $\Omega-\Omega_p=0$. The first case occurs at positions $r_{L,m}$ known as Lindblad resonances, whereas the second case occurs at the position r_C known as the corotation resonance. These waves carry angular momentum flux, thus a torque is exerted on the disk, and in turn, the disk exerts a torque on the planet. It is possible to analytically estimate the resulting torque using the Wentzel-Kramers-Brillouin (WKB) approximation (Goldreich & Tremaine, 1979; Lin & Papaloizou, 1979). This migration regime is

known as type I migration and the torque exerted on the planet can be divided into a Lindblad torque and a corotation torque.

Lindblad torque

The Lindblad resonances are locations in the disk where the gas azimuthal velocity relative to the planet matches the phase velocity of azimuthal acoustic waves (Baruteau et al., 2014) and condition (i) cited above is fulfilled. The superposition of the waves at the Lindblad resonances leads to the formation of a one-armed spiral density wave that propagates from the planet position (e.g., Goldreich & Tremaine, 1979, 1980; Ogilvie & Lubow, 2002). The Lindblad torque was analytically estimated by Tanaka et al. (2002) for 3D disks; however, their formula is valid only in the isothermal case. So far there is no estimate for the Lindblad torque in 3D non-isothermal disks. The main reason is that the analytics involved are very difficult (Tanaka et al., 2002; D'Angelo & Lubow, 2010). Moreover, it is not trivial to separate the corotation torque from the Lindblad one in 3D numerical simulations (Baruteau et al., 2014).

It has been showed that when the planet gravitational potential is appropriately softened, two-dimensional (2D) results can recover effects of vertical stratification (Müller et al., 2012; Kley et al., 2012). Therefore, 2D results comparable to a more precise 3D simulation are possible. Paardekooper et al. (2010a) used this softening gravity approach in their 2D simulations and obtained a formula for the Lindblad torque in adiabatic disks

$$\gamma \frac{\Gamma_L}{\Gamma_0} = -2.5 - 1.7\beta_T + 0.1\beta_\Sigma, \tag{1.55}$$

with

$$\Gamma_0 = \left(\frac{q}{h}\right)^2 \Sigma_p R_p^4 \Omega_p^2, \tag{1.56}$$

where β_T is the negative exponent for the temperature profile, β_Σ is the negative exponent for the surface density profile, $q = M_p/M_\star$ is the ratio between the planet and stellar masses, Σ_p is the surface density at the planet position, and R_p is the planet position. The formula above is valid for non-isothermal disks, in general, if γ is replaced by an effective γ_{eff} that depends on thermal diffusion (Paardekooper et al., 2011). The surface density and temperature profiles decrease with radius, thus β_Σ and β_T are positive. For reasonable values for the surface density slope, negative Lindblad torques are obtained. This torque takes angular momentum away from the planet, thus the planet moves inwards due to it. Tanaka et al. (2002) showed that the Lindblad torque is always predominant with respect to the

corotation torque, for isothermal disks, thus leading to inward migration for low mass planets. A timescale for the type I migration can be estimated using the normalization constant Γ_0 (Baruteau et al., 2014)

$$\tau_I = \frac{R_p}{\dot{R}_p} = \frac{1}{2}\frac{h^2}{q}\frac{M_\star}{\Sigma_p R_p^2}\Omega_p^{-1}. \tag{1.57}$$

Assuming typical values for the disk parameters, leads to a timescale of $\sim 3\times10^5$ yr for Earth-mass planets at 1 au, which is much shorter than the disk lifetimes (Baruteau et al., 2014). This fast type I migration timescale is a huge problem to explain the observed mass-distance distribution of exoplanets (Alibert et al., 2004; Ida & Lin, 2008; Mordasini et al., 2009). One of the objectives of this work is to study how to make the type I migration less efficient. This subject is tackled in Chapter 3.

Corotation torque or horseshoe drag

In principle, the corotation resonance should be located at the planet orbital radius, condition (ii) cited above; however, due to the pressure gradient, this resonance is offset from the planet position (Lin & Papaloizou, 1986; Ward, 1997; Tanaka et al., 2002). Using the same procedure as for the Lindblad torque, one can estimate the corotation torque for isothermal disks (e.g., Tanaka et al., 2002). Goldreich & Tremaine (1979) showed that the linear isothermal corotation torque scales with the local gradient of the potential vorticity[2]. When non-isothermal disks are considered, a second component is found, which is dependent on the entropy gradient (Baruteau & Masset, 2008a; Paardekooper & Papaloizou, 2008). The corotation torque comes from the fact that fluid elements are moving in a horseshoe orbit around the planet. These fluid elements follow equipotential surfaces around the Lagrangian points, which can be estimated by the two-body problem. The angular momentum of a fluid element changes every time it approaches the planet, executing a U-turn from the inner (outer) side to the outer (inner) side of the planet orbit, see Figure 1.6. This change in the angular momentum of fluid elements executing a U-turn leads to a torque exerted on the planet.

Ward (1991) estimated the corotation torque by considering disk material executing a horseshoe orbit relative to the planet. Potential vorticity should be conserved in an isothermal inviscid disk. When a fluid element executes a U-turn, it is taken to a region of different vorticity, thus the surface density should change in order to conserve the potential vorticity. This process leads to a torque exerted

[2]Potential vorticity is defined as vorticity divided by surface density.

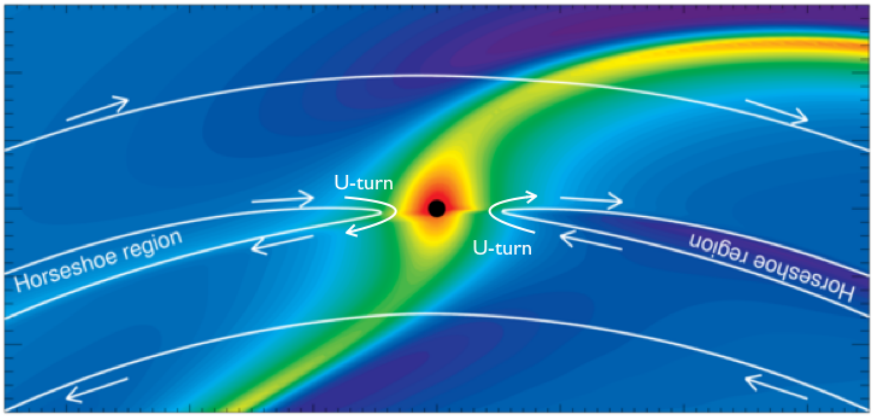

Figure 1.6 The color shows the relative perturbation of the surface density for a 5 Earth-mass planet. The spiral density wave induced by the planet can be seen. The typical gas trajectories, with respect to the planet, in the horseshoe region are shown with white curves and arrows. Figure adapted from Baruteau et al. (2014).

on the planet, which is called a horseshoe drag. The linear corotation torque and the horseshoe drag turns out to depend on the same things, in fact, they should represent the same mechanism. The horseshoe drag, however, is found to be stronger than the linear corotation torque (Paardekooper & Papaloizou, 2009; Paardekooper et al., 2010a). The only difference between the two is that the horseshoe drag takes into account nonlinear terms, which was found to make a difference.

Paardekooper & Mellema (2006) showed that the horseshoe drag is highly dependent on the viscosity and thermal properties of the disk. In an adiabatic disk, entropy should be conserved. Assuming a radial entropy gradient, as a fluid element executes a U-turn, its entropy has a jump to guarantee the entropy conservation. This jump in entropy produces vorticity, thus leading to another torque exerted on the planet (Masset & Casoli, 2009). The horseshoe drag in an adiabatic disk is given by (Paardekooper et al., 2010a)

$$\gamma\frac{\Gamma_{HS}}{\Gamma_0} = 1.1\left(\frac{3}{2} - \beta_\Sigma\right) + 7.9\frac{\beta_S}{\gamma}, \tag{1.58}$$

where β_S is the negative exponent of the entropy profile. The first term on the right-hand side represents the vortensity-related horseshoe drag, whereas the second term the entropy-related. Masset & Casoli (2010) and Paardekooper et al. (2011) obtained estimates for the horseshoe drag, for general non-isothermal cases. Equation 1.58 shows that for disk profiles where entropy decreases with radius, thus positive β_S, a positive horseshoe drag can be obtained. Numerical simulations already showed that the horseshoe drag can be large enough to overcome the Lindblad torque in

non-isothermal disks (e.g., Morohoshi & Tanaka, 2003; Paardekooper & Mellema, 2006), thus leading to outward migration for low mass planets. This is a very promising mechanism to slow down or reverse the type I migration. Nevertheless, there is a limited amount of angular momentum in the horseshoe region, that the horseshoe drag can use to counteract the Lindblad torque. Angular momentum transport through the disk is then crucial to keep the horseshoe drag unsaturated and sustain slow type I migration (Baruteau et al., 2014). This issue is discussed in Chapter 3, where the unsaturation of the horseshoe drag is studied.

Effects of self-gravity, magnetic fields, and eccentric/inclined orbits

Pierens & Huré (2005) showed that when self-gravity is considered, the Lindblad resonances get shifted towards the planet, thus the Lindblad torque becomes stronger. Their result was numerically confirmed by Baruteau & Masset (2008b). Magnetic fields do not seem to alter the Lindblad torque. Nevertheless, when a magnetic field is present, instead of having just acoustic waves, there are fast and slow magneto-sonic waves and Alfvén waves. For strong azimuthal magnetic fields, slow magneto-sonic waves are launched at magnetic resonances (Terquem, 2003). These waves also carry angular momentum and therefore leads to a new torque component. Terquem (2003) and Fromang et al. (2005) found that this magnetic component can be positive, leading to outward migration. The vertical component of a magnetic field also alters the magnetic resonances (Muto et al., 2008). Uribe et al. (2015) showed that azimuthal and vertical large-scale magnetic fields in 3D simulations can slow down the type I migration by a factor of two; however, the migration reversal is not possible. They demonstrated that migration reversal due to an azimuthal field is conceivable just in the 2D case. Regarding the horseshoe drag, strong azimuthal magnetic fields prevent horseshoe motions, thus the horseshoe drag is extinguished. For weak magnetic fields, the horseshoe motions take over and suppress the magnetic resonances (Guilet et al., 2013). It was noticed in simulations with weak azimuthal magnetic fields, that there is accumulation of magnetic field near the downstream separatrices of the horseshoe region. In order to sustain pressure balance, an underdensity is then created at this location, leading to a new torque component, which can be even stronger than the entropy-related horseshoe drag and sustain outward migration (Guilet et al., 2013).

A stochastic component for the torque was found in MHD simulations, which is driven by turbulence generated by MRI (Nelson & Papaloizou, 2004; Laughlin et al., 2004; Nelson, 2005). This torque component is dependent on the turbulence strength, rather than the planet mass. Therefore, this stochastic torque can dominate the

migration of planetesimals and small planet cores (Baruteau & Lin, 2010; Nelson & Gressel, 2010). Since a random walk component is added to the planet migration, it is expected that a small fraction of planets can migrate to the outer disk due to this effect (Johnson et al., 2006; Adams & Bloch, 2009). The MRI is also a good candidate to prevent the horseshoe drag saturation. Baruteau et al. (2011) and Uribe et al. (2011) showed that outward migration can be sustained for fairly long times in MHD simulations.

All the previous discussion was related to low mass planets moving in co-planar circular orbits. For small eccentricities, the disk tends to damp non-circular motions (Goldreich & Tremaine, 1980; Artymowicz, 1993a; Masset, 2008), the same being valid for inclined planets (Tanaka & Ward, 2004). This damping was confirmed by hydrodynamical simulations (Cresswell et al., 2007; Bitsch & Kley, 2010, 2011). Bitsch & Kley (2010) showed that the magnitude of the horseshoe drag decreases for increasing eccentricities, because the width of the horseshoe region gets narrower (Fendyke & Nelson, 2014). The Lindblad torque, in contrast, gets higher for increasing eccentricities (Papaloizou & Larwood, 2000). Nevertheless, it does not imply outward migration, since the torque in this case acts to change the planet orbital position, as well as the planet eccentricity (Masset, 2008). In the case of inclined planets, the planet interacts less with the dense midplane gas as the inclination increases, leading to smaller horseshoe drags. This shows that inclined planets can undergo outward migration only if the inclination is below a few degrees (Bitsch & Kley, 2011).

1.3.3 High mass planets

High mass planets, with masses greater than about Saturn's mass, highly perturb their parent disks, thus they strongly modify the local disk structure, in contrast to the low mass planet case. When the planet gets above a certain mass, it can open a cavity around its orbit. As described in Section 1.3.2, the planet spiral density wave transports angular momentum through the disk. The inner spiral gives angular momentum from the inner disk to the planet, whereas the outer spiral takes angular momentum from the planet and gives to the outer disk. As a consequence, the inner disk can move inwards and the outer disk outwards, opening what is called a planetary gap.

The basic condition for a planet to be able to carve out a gap, is that the gravity torque, from the spiral waves, must exceed the disk viscous torque. This condition is necessary because viscosity wants to spread mass to fill up the void areas (Lin & Papaloizou, 1979; Goldreich & Tremaine, 1980). Therefore, the gap width should

be set by the position where the gravity and viscous torques balance each other (Varnière et al., 2004). The gap width and depth should then increase as viscosity decreases. This dependence appeared to be much weaker in numerical simulations than expected by theory. Crida et al. (2006) explained this discrepancy, clarifying that just a fraction of the planet gravitational torque is locally deposited in the disk, some of it is transported away by density waves (Papaloizou & Lin, 1984; Goldreich & Nicholson, 1989; Rafikov, 2002). Thus, the viscous torque has to counterbalance just a fraction of the gravitational torque. Crida et al. (2006) showed that the angular momentum flux carried by these density waves corresponds to a pressure torque. When the disk achieves equilibrium, the gap profile can be obtained by considering the balance between the pressure, gravity, and viscous torques. Crida et al. (2006) obtained a new criterion for gap opening considering this balance

$$\mathcal{P} = \frac{3}{4}\frac{H}{R_H} + \frac{50}{q\mathcal{R}} \lesssim 1, \tag{1.59}$$

where $R_H = R_p(q/3)^{1/3}$ is the planet Hill radius and $\mathcal{R} = R_p^2\Omega_p/\nu$ is the Reynolds number. When this condition is fulfilled the planet can carve out a gap with density contrast of at least 90%.

Planets with $\mathcal{P}$ values of a few can open partial gaps with density contrasts of few tens of percent (Baruteau et al., 2014). The criterion above is confirmed by MHD simulations. Nevertheless, viscous disk models with α-values similar to the ones obtained by MRI display gaps with different widths and depths (Papaloizou et al., 2004; Zhu et al., 2013). It has also been showed that a planet, which does not fulfill the above criteria, can open a very deep gap in disks with quite low viscosities, as it is expected in dead zones (Duffell & MacFadyen, 2013). In Chapter 4, the effect of dust radiation and stellar irradiation for gap opening planets interacting with their parent disks is studied.

Gap-opening planets do not feel a Lindblad torque, as this torque is cancelled out by the viscous and pressure torques. Since the material in the horseshoe region is also almost totally depleted, there is no horseshoe drag. The planet is then locked inside its gap and migrates following the viscous evolution of the disk. This regime is known as type II migration and the timescale is given by the viscous timescale (Lin & Papaloizou, 1986)

$$\tau_{II} = \tau_\nu = \frac{R_p^2}{\nu}. \tag{1.60}$$

Eccentricities and inclinations

The disk tends to damp any eccentricity or inclination for high mass planets (Bitsch et al., 2013; Xiang-Gruess & Papaloizou, 2013), as it happens for low mass planets. Nevertheless, several massive planets display high eccentricities and inclinations, as it was discussed in Section 1.2.4. One possibility is that these planets acquire non-circular inclined orbits due to planet-planet scattering. Once the gaseous disk is dispersed, gravity dominates the interaction between the survivor planets and may reshape the configuration of the final planetary system, generating eccentric and inclined orbits (Ford & Rasio, 2008). However, there are some possibilities to explain these features through planet-disk interactions.

Eccentricity can be excited because of the $m = 3$ eccentric inner Lindblad resonance (Lubow, 1991). The planetary gap should be wide enough, so that the eccentricity pump effect can be larger than the disk damping effect, allowing the planet and the disk eccentricities to grow (Papaloizou et al., 2001). Numerical simulations have shown that planets with masses in the range $5 - 10$ Jupiter masses can acquire eccentricities up to ~ 0.25 due to planet-disk interactions (Papaloizou et al., 2001; Bitsch et al., 2013; Dunhill et al., 2013).

Inclinations can be easily explained if there exist a misalignment between the rotation axis of the star and the disk. One possible mechanism to generate such misalignment is that material with different angular momentum direction can be added at different stages of the disk lifetime (Bate et al., 2010). Another possibility is that a stellar companion in a dense stellar cluster can tilt the disk's rotation axis as it flies-by (Batygin, 2012). Finally, the interaction of the disk with the magnetic field of its central star may tilt the star's rotation axis (Lai et al., 2011).

Observational signatures

To date, gap structures, as expected by planet-disk interactions, have been observed in the disks of HD 169142 (Quanz et al., 2013) and TW Hya (Debes et al., 2013). Apart from that, cavities have been observed in several protoplanetary disks. Nevertheless, there is no proof that these cavities are due to high mass planets, since they are characterized by an absence of dust in the inner disk, therefore they are transition disks. If a planet is much more massive than the gas just outside its gap, its inertia can hold the outer disk, while the inner disk is accreted by the central star in the normal viscous timescale. The threshold for the planet mass is $M_p > 4\pi\Sigma_o R_p^2$, where Σ_o is the surface density just outside the planetary gap, and the migration of such planets is slower than the viscous timescale and defined by

(Baruteau et al., 2014)

$$\tau_{II} = \tau_\nu \frac{M_p}{4\pi\Sigma_o R_p^2}. \tag{1.61}$$

This process is an alternative explanation for transition disks, in addition to photoevaporation. To relate these cavities to the presence of planets, one need to measure the gas content inside these cavities, as well as understand the decoupling of the dynamics of the gas and dust components. New observations using the ALMA observatory and the upcoming *Multi AperTure mid-Infrared SpectroScopic Experiment* (MATISSE) instrument should give more insight to this matter (Baruteau et al., 2014).

Large-scale anticyclonic vortices are another possible observational sign of massive planets (e.g., Fu et al., 2014; Les & Lin, 2015). The edges of a gap opened by a planet posses a sharp surface density gradient, therefore the RWI can be triggered in these regions. This instability may produce large-scale vortices next to the planetary gap. Dust asymmetries have been observed in several transition disks (Isella et al., 2013; van der Marel et al., 2013; Casassus et al., 2013; Fukagawa et al., 2013; Pérez et al., 2014), which could be explained by large-scale vortices. Figure 1.7 shows the case of Oph IRS48 (van der Marel et al., 2013). The vortex structure is revealed by the asymmetric millimeter continuum emission (panel A), which displays the millimeter-sized dust grain distribution. The molecular line observations shows a symmetric gas disk with Keplerian rotation at an inclination of 50° (panel B). The mid infrared emission (panel C) indicates that the micrometer-sized dust grains are symmetrically spread throughout the ring. In Chapter 2, the formation and evolution of planet-induced vortices is studied, as well as a model for the Oph IRS48 system is presented.

1.3.4 Intermediate mass planets embedded in massive disks

Intermediate mass planets, from sub-Saturnian to Jovian masses, that carves out a partial gap in their parent disk may suffer a third migration regime, which is called type III migration (Masset & Papaloizou, 2003). In this regime, the planet has a relative radial drift with respect to the disk, that may be caused due to the planet's migration itself and/or the disk viscous radial drift.

The torque applied on the planet has a contribution from trapped material in the planet's horseshoe region that executes U-turns around the planet. This component is exactly the same as the horseshoe drag explained in Section 1.3.2. Another contribution comes from fluid elements that crosses the planet only one time. The exchange of angular momentum between the planet and this material is

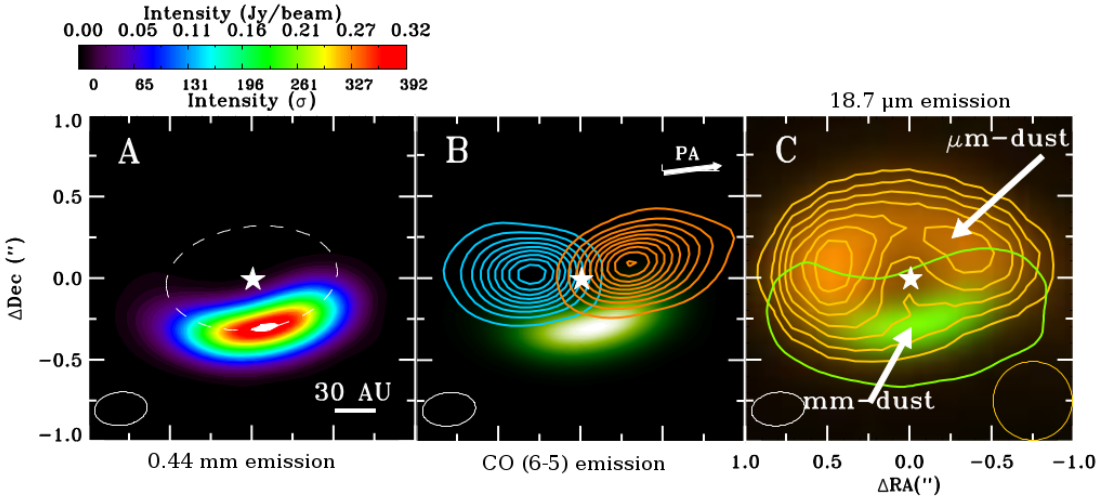

Figure 1.7 The star symbol marks the star position and the white ellipse the ALMA beam. Panel A displays the 0.44 mm continuum emission, obtained with the ALMA observatory, the white dashed ellipse with 63 au radius marks the vortex position. Panel B displays the velocity contours of the integrated $^{12}CO(6-5)$ emission, obtained with the ALMA observatory. The position angle (PA) is indicated in the upper right corner. Panel C displays the 18.7 μm emission in orange color, obtained with the *VLT Imager and Spectrometer for mid InfraRed* (VISIR) instrument at the VLT telescope, the beam size is indicated with an orange circle. The green line shows the 5σ contour line of the 0.44 mm continuum emission. The green background in panels B and C displays the 0.44 mm continuum emission. Figure adapted from van der Marel et al. (2013).

dependent on the mass flow rate across the planet orbit, thus it depends on the relative radial drift between the planet and the disk. This torque is negative in the case the planet is moving inwards, whereas it is positive in the case the planet is moving outwards. Since the material trapped at the planet's horseshoe region should also move at the same pace as the planet. A negative (positive) torque by the planet is applied on this material, in turn, this material applies a positive (negative) torque on the planet. Both torques being also dependent on the relative radial drift.

In the case that the planet mass is larger than the mass difference between the material in the horseshoe region and the material crossing the planet orbit, the planet migration is accelerated. In the case this mass difference is larger than the planet mass, so for massive disks, the planet migration suffers a runaway, meaning an exponentially growth for the drift rate. When the drift rate reaches the so-called fast regime, the drift rate settles to this finite large value, and this drift rate defines the type III migration regime (Baruteau et al., 2014).

1.3.5 Multiple planets

All the previous discussion considered the evolution of single planets. Nevertheless, several multi planetary systems have been discovered, especially with the *Kepler* mission. The dynamics of multi planetary systems are different than of a single planet, since the gravitational forces between the planets can lead to resonant configurations. When two planets have different migration rates or are formed close to each other and are massive enough to carve out a common gap, they may be captured in resonant positions, if their migration is convergent. In the case of a divergent migration, thus larger separations with time, the interaction between the two planets becomes small and no resonant capture occurs (e.g., Kley et al., 2004; Kley & Nelson, 2012; Baruteau et al., 2014).

For a mean-motion resonance to occur, the orbital frequencies of the planets should satisfy (Baruteau et al., 2014)

$$(p+q)\Omega_{p2} - p\Omega_{p1} = 0, \tag{1.62}$$

where Ω_{pi} is the angular velocity of planet i and (p, q) are positive integers. When the orbital frequencies of two planets satisfy this condition, they are said to be in a $(p+q) : p$ mean-motion resonance. Two planets are captured in a mean-motion resonance if the convergent migration timescale is longer than the libration timescale of the resonance width (Snellgrove et al., 2001). Otherwise, there is no time for the resonance to be excited, the planets pass through it and no capture occurs (Quillen, 2006; Mustill & Wyatt, 2011).

The two planets may be captured in different resonances, depending on their mass, relative migration speed, and initial separation (Nelson & Papaloizou, 2002). The 2:1 resonance is the most common, because it is the first first-order resonance that two planets with large initial separations in a convergent migration encounters (Baruteau et al., 2014). Once the planets are captured in a resonance, they migrate as a pair. Eccentricities then tend to increase and if no damping was present, it would grow to very large values that makes the system unstable (Kley et al., 2004). The growth of eccentricities and inclinations due to planet-planet interactions, such as just described, is a possible explanation for the large eccentricities observed for some exoplanets. In particular, when the disk is dissipated and no disk damping is present, planet-planet interactions can lead to high eccentricities and inclinations (Chatterjee et al., 2008; Jurić & Tremaine, 2008; Matsumura et al., 2010). The theory of resonant capture matches pretty well observed multi planet systems (Lee & Peale, 2002; Kley et al., 2005; Crida et al., 2008; Correia et al., 2009; Rein et al., 2010).

The picture is similar for systems with more than two planets. For instance, it has been showed by numerical simulations, that a system with several protoplanets experiencing type I migration can lead to crowded systems (McNeil et al., 2005; Papaloizou & Szuszkiewicz, 2005; Cresswell & Nelson, 2008). This may explain the observations by the *Kepler* mission of low mass planets packed very close to the parent star (e.g., Lissauer et al., 2011). In this scenario, the strong disk damping render the low mass planets in stable co-planar circular orbits during their migration.

A last interesting feature of planet-planet interactions in a gaseous disk is that it may lead to outward migration of a pair of planets (Masset & Snellgrove, 2001; Morbidelli & Crida, 2007; Pierens & Nelson, 2008; D'Angelo & Marzari, 2012). Supposing a large gap-opening planet located at R_{p1} experiencing type II migration. If a less massive planet that carves out a partial gap is located at $R_{p2} > R_{p1}$, it migrates faster than the inner planet. At some point their gaps merge and the planets may be captured into a mean-motion resonance. The final torque felt by the planet pair is then positive, because the inner planet is larger than the outer one, thus the inner torque is larger and the net torque is positive. The Grand Tack model (Walsh et al., 2011) uses this scenario to describe the migration of Jupiter and Saturn and it was successful in explaining the small mass of Mars and the distribution of the main asteroid belt.

1.4 Structure of the thesis

The aim of this thesis is to study several aspects of planet-disk interactions. Hydrodynamical simulations of non-isothermal disks are performed using the PLUTO code (Mignone et al., 2007), the planet-disk module of Uribe et al. (2011), and new approaches for the temperature evolution. It is important to include the disk temperature evolution, since the thermodynamics of the system can strongly influence how planets evolve and interact with their parent disk. This thesis is organized as follows.

In Chapter 2, the formation and evolution of planet-induced vortices in two-dimensional and initially buoyantly unstable disks is investigated. A Newtonian cooling approach (thermal relaxation) is used to describe the temperature evolution of the disk. Several benchmark cases with different thermal relaxation timescales and two different planet masses are considered. The role of the Rossby wave instability and radial buoyancy for the formation and evolution of the planet-induced vortices is discussed. A model for the Oph IRS48 system is presented, using a similar physical setup as the benchmark cases. The dependence of the

vortices lifetimes and birth times with respect to the thermal relaxation time scale is also studied.

In Chapter 3, type I migration in two-dimensional non-isothermal turbulent disks is studied. The same cooling approach as in Chapter 2 is used. Buoyantly unstable disks are considered, thus the turbulence is generated due to a convective instability. The effect the thermal relaxation timescale, the disk temperature slope, the disk aspect ratio, and the planet mass have for the total torques and the generation of turbulence is investigated. It is also studied whether the turbulence-triggered viscosity can slow down the migration rate or reverse the migration direction.

In Chapter 4, three-dimensional radiative-hydrodynamical simulations of planet-disk interactions are presented. The planet-disk (Uribe et al., 2011) and radiation transport (Kuiper et al., 2010) PLUTO modules are merged. The coupling of radiation transport with hydrodynamics is an important step, since it provides a more precise temperature evolution compared to the consideration of a simple cooling law. The interaction between gap opening planets and their parent disks is studied. The results with radiation transport are contrasted with locally isothermal and adiabatic models. These simulations are used to test the new radiation transport planet-disk PLUTO module.

In Chapter 5, a summary of this thesis is given, along with the main results and conclusions. In addition, some perspectives for future work are listed.

Chapter 2

Vortex formation and evolution in planet harboring disks under thermal relaxation

The work presented in this chapter is from **Lobo Gomes, A.***, Klahr, H., Uribe, A. L., Pinilla, P., Surville, C., The Astrophysical Journal, 810, 94.*

High mass planets leave remarkable features in their parent protoplanetary disks (PPDs), namely a gap, spiral waves, vortices, and eccentricities. These features are captured in numerical simulations of planet-disk interactions (e.g., Nelson et al., 2000; Winters et al., 2003; Klahr & Kley, 2006; Kley & Dirksen, 2006; de Val-Borro et al., 2007; Uribe et al., 2011; Lin & Papaloizou, 2011a,b; Ataiee et al., 2013; Zhu & Stone, 2014), and are also expected to be observationally detectable (Regály et al., 2010; Pinilla et al., 2012; Ruge et al., 2013; Regály et al., 2014; Ruge et al., 2014; Juhász et al., 2015; Pinilla et al., 2015). In this chapter we are particularly interested in studying the evolution of planet-induced vortices in buoyantly unstable disks.

Vortices can be formed in PPDs as a product of a Kelvin-Helmholtz instability, referred to as the Rossby wave instability (RWI) for accretion disks, and/or unstable radial buoyancy. The RWI can be triggered when there is a local bump in the inverse potential vorticity profile of the disk (Lovelace et al., 1999; Li et al., 2000). Radial buoyancy can be manifested as the baroclinic instability (BI, Klahr & Bodenheimer, 2003), which needs a radially decreasing pressure and entropy, or in other words, a pressure and entropy gradients with the same sign. Vortices can be amplified due to the subcritical baroclinic instability (SBI, Lesur & Papaloizou, 2010), which is a nonlinear process. A convective overstability (CO, Klahr & Hubbard, 2014; Lyra,

2014) is also able to amplify vortices, CO is the linear phase of SBI. More about this topic will be discussed in Section 2.3. Vortices are interesting structures to be studied, considering that they are important in the context of planet formation, angular momentum transport through the dead zone, and type I migration.

In the context of planet formation, vortices are good candidates to trap dust grains allowing them to grow to planetesimal or planets sizes (Barge & Sommeria, 1995; Klahr & Bodenheimer, 2006). This scenario is a possible solution for the radial drift barrier – large dust grains achieve high velocities toward the central star, making for them impossible to grow before being accreted (Whipple, 1972). However, if the disk has a pressure bump, the dust grains can get trapped into this pressure maximum and an anticyclonic vortex is an example of such maxima (e.g., Bracco et al., 1999; Varnière & Tagger, 2006; Inaba & Barge, 2006; Lyra et al., 2009b; Regály et al., 2012; Meheut et al., 2012a).

Accretion disks need some mechanism to transport angular momentum outwards, allowing then matter to fall inwards. Shakura & Sunyaev (1973) introduced an α-disk model to explain this transport, where viscosity, triggered by some kind of turbulence, is shown to be an efficient accretion mechanism. Usually, magnetorotational instability (MRI; Balbus & Hawley, 1991) is the most invoked mechanism to explain turbulence in accretion disks, though in PPDs there is a region, around the disk's midplane, where the level of ionization is not high enough for MRI to take place: the so called dead zone (Gammie, 1996). The problem of angular momentum transport through the dead zone has been investigated by many authors (e.g., Klahr & Bodenheimer, 2003; Lesur & Papaloizou, 2010; Dzyurkevich et al., 2010; Meheut et al., 2012b). Large-scale vortices in the dead zone of PPDs can help to transport angular momentum through that region. Meheut et al. (2012b) studied the angular momentum flux carried by Rossby vortices. The exchange of angular momentum between Rossby waves in the inner and outer sides of a density bump, leads to a negative net flux, thus an outward transport of angular momentum.

Vortices may also play a role in the context of type I migration. Planet cores and low mass planets experience type I migration (Ward, 1997; Tanaka et al., 2002). One of the biggest issues about type I migration is the fast time scale in which it happens. Vortices are able to trap not only dust particles but also planet cores, thus they are able to slow down the type I migration rate (e.g., Koller et al., 2003; Ou et al., 2007; Li et al., 2009; Yu et al., 2010; Regály et al., 2013; Ataiee et al., 2014).

The formation of planet-induced vortices is being explored thoroughly (e.g., Balmforth & Korycansky, 2001; de Val-Borro et al., 2007; Lyra et al., 2009a; Lin &

Papaloizou, 2011b; Zhu & Stone, 2014; Fu et al., 2014; Les & Lin, 2015). Fu et al. (2014) studied the long term evolution of vortices depending on the disk viscosity, disk temperature, and planet mass. They found critical parameters for the disk viscosity ($\nu = 10^{-7} r_p^2 \Omega_p^2$) and temperature ($h/r_p = 0.06$) that lead to a long vortex lifetime ($\sim$ 1 Myr). A nonmonotonic behavior with respect to the viscosity and temperature was found, thus high and low viscosities/temperatures lead to a faster damping of the vortices. They concluded also that disks with same viscosity and temperature, but more massive planets, in their case $5 M_J$, can sustain vortices for a longer time. Les & Lin (2015) studied vortex evolution in terms of different cooling timescales. They found a non-monotonic dependence of the vortex lifetimes with the cooling timescales, which is in agreement with Fu et al. (2014). Moreover, they pointed out the importance of not considering locally isothermal disks, due to the fact that the RWI theory was developed for adiabatic disks (Lovelace et al., 1999; Li et al., 2000).

In addition to the theoretical/numerical state-of-art, observations with high angular resolution are increasing. The *Atacama Large Millimeter/submillimiter Array* (ALMA) is now giving the capabilities to detect structures which may be related with unseen planets. Recently, dust asymmetries were observed in five different systems: LkHa 330 (Isella et al., 2013), Oph IRS48 (van der Marel et al., 2013), HD 142527 (Casassus et al., 2013; Fukagawa et al., 2013), SAO 206462 (Pérez et al., 2014), and SR 21 (Pérez et al., 2014). An anticyclonic vortex could be a reasonable explanation for these asymmetries; however, the definite explanation for these observations is still under debate (Pinilla et al., 2015; Flock et al., 2015).

The aim of this chapter is to study the long term evolution of planet-induced vortices in buoyantly unstable disks. The chapter is laid out as follows. In Section 2.1 we describe the planet-disk model and simulation setups. We describe the general evolution of our different simulations in Section 2.2. We discuss the role that the RWI and buoyancy played for vortex formation and sustenance in Section 2.3. We study the convergence of our results with respect to several factors in Section 2.4. We observed the formation of a second generation of vortices, which arise in a surface density enhancement that is created beyond the primary vortex position. The formation of the secondary vortices is discussed in Section 2.5. The vortex lifetimes and birth times with respect to different thermal relaxation timescales is discussed in Section 2.6. Lastly, in Section 2.7 we briefly summarize our results and state our conclusions.

2.1 Simulations

We study the formation and evolution of vortices in the outer edge of planetary gaps by solving numerically the following system of hydrodynamical (HD) equations

$$\frac{\partial \Sigma}{\partial t} + \boldsymbol{\nabla} \cdot (\Sigma \mathbf{v}) = 0, \tag{2.1}$$

$$\frac{\partial \mathbf{v}}{\partial t} + \mathbf{v} \cdot \boldsymbol{\nabla} \mathbf{v} = -\frac{\boldsymbol{\nabla} p}{\Sigma} - \boldsymbol{\nabla} \Phi_g, \tag{2.2}$$

$$\frac{\partial p}{\partial t} + \mathbf{v} \cdot \boldsymbol{\nabla} p + \Sigma c_s^2 \boldsymbol{\nabla} \cdot \mathbf{v} = 0, \tag{2.3}$$

where Σ is the gas surface density, $\mathbf{v}$ is the velocity, p is the vertically integrated pressure, Φ_g is the gravitational potential, and c_s is the sound speed. In order to close the system of equations, we used an ideal equation of state $p = c_s^2 \Sigma / \gamma$, with $\gamma = 1.4$.

We considered an inviscid disk, thus no prescribed viscosity was included. This approximation may influence the vortex evolution, since previous works showed that the vortex lifetime is inversely proportional to the magnitude of viscosity (de Val-Borro et al., 2007; Ataiee et al., 2013; Fu et al., 2014). In this chapter, we would like to study the direct influence of the RWI and radial buoyancy for the development of the vortices. Therefore we chose to not include a prescribed viscosity. In our models, the only possible source of viscosity is the turbulence-triggered viscosity by the hydrodynamical instabilities. Lastly, we assumed that the barycenter of the system is located at the star's center. This simplification is plausible, because the planet masses considered are not very large (1 and $3 M_J$) neither the vortices accumulate much mass,[1] thus the deviation of the barycenter with respect to the star's center should be small. Nonetheless, this approximation may slightly influence planet-induced vortex formation, since it eliminates the Lagrange point L3, in the corotation region, which could change the gap structure.

We used the planet-disk module for the PLUTO code that is presented in Uribe et al. (2011). The gravitational potential includes contributions from the planet and the star, and it is given by

$$\Phi_g(\mathbf{r}) = -\frac{G M_p}{\sqrt{(|\, \mathbf{r} - \mathbf{R_p} \,|^2 + \epsilon^2)}} - \frac{G M_\star}{|\, \mathbf{r} \,|}, \tag{2.4}$$

where G is the gravitational constant, M_p is the planet mass, $\mathbf{R_p}$ is the planet location, $M_\star$ is the stellar mass and ϵ is a softening parameter. It is needed to soften

[1] We obtained vortices masses up to a few $10^{-4} M_\odot$, integrating the surface density with respect to the area element inside the vortex region.

the gravitational potential of the planet in order to avoid numerical divergence close to the planet's location. Moreover, this softening can account for 3D effects of vertical stratification. We considered this parameter as being a fraction of the Hill radius $\epsilon = kR_H$, with $k = 0.6$ and $R_H = R_p(M_p/(3M_\star))^{1/3}$. The recommended softening factor for the planet gravitational potential is of $\epsilon = 0.6H - 0.7H$ (Kley et al., 2012), where H is the disk scale height. These values can recover 3D effects of vertical stratification. The Hill radius and the disk scale height at the planet position are similar in our simulations, thus we chose $\epsilon = 0.6R_H$.

The stationary solution of a sub-Keplerian disk was taken as initial conditions, which in polar coordinates is given by

$$\Sigma = \Sigma_0 \left(\frac{r}{r_0}\right)^{-\beta_\Sigma}, \tag{2.5}$$

$$c_s = c_0 \left(\frac{r}{r_0}\right)^{-\beta_T/2}, \tag{2.6}$$

$$v_r = 0, \tag{2.7}$$

$$v_\phi = \sqrt{v_K^2 + \frac{r}{\Sigma}\frac{\partial p}{\partial r}}, \tag{2.8}$$

where Σ_0 is the initial surface density at $r_0 = 1$ au, $\beta_\Sigma = 1.5$ is the slope for the power law distribution of surface density, $\beta_T/2 = 0.5$ is the slope for the power law distribution of sound speed, v_K is the Keplerian velocity, and $h = c_s/v_K = H/r = 0.05$ is the initial aspect ratio and fix the intial sound speed c_0 at $r_0 = 1$ au, since v_K at $r_0 = 1$ au is set as one.

The planet is set up as a point mass in a given position R_p and with a given mass M_p. In order to avoid an initial big disturbance to the disk, we added the planet slowly along its first Keplerian orbit, according to the following

$$M_p' = M_p \left[\sin\left(\frac{\pi}{2}\frac{t}{P}\right)\right]^2, \tag{2.9}$$

where t is the global time and $P = 2\pi(GM_\star/R_p)^{-3/2}$ is one planetary orbit. Thus, while $t < T$ the planet mass slowly increases toward M_p.

The assume the Keplerian velocity $v_{\phi,p} = \sqrt{GM_\star/R_p}$ as the planet initial velocity and the initial acceleration coming from the gravitational interaction with the star and the disk is

$$\mathbf{a_p} = -\frac{GM_\star \mathbf{R_p}}{|\,\mathbf{R_p}\,|^3} + \xi \int_{\text{disk}} \frac{G\Sigma(\mathbf{r} - \mathbf{R_p})}{\sqrt{(|\,\mathbf{r} - \mathbf{R_p}\,|^2 + \epsilon^2)^3}} dA, \tag{2.10}$$

where dA is the area element and ξ is a factor that soften the contribution of the disk gravity in the Hill sphere and is given by

$$\xi = 1 - \exp\left[-\frac{|\,\mathbf{r} - \mathbf{R_p}\,|^2}{(0.6R_H)^2}\right]. \tag{2.11}$$

Lastly, the planet position, velocity, and acceleration changed according to the dynamical interaction with the star-disk system. Its acceleration changes with time following Equation 2.10 and its position and velocity are then updated using a leapfrog integrator.

2.1.1 Thermal relaxation

In order to account for radiative effects, we applied cooling to the system. We modelled this cooling via thermal relaxation, following the approach below

$$\frac{dT}{dt} = -\frac{(T - T^0)}{\tau(r)}, \tag{2.12}$$

where T is the temperature, T^0 is the initial temperature (equilibrium temperature as result of irradiation), and $\tau(r)$ is the relaxation timescale, which depends on radius ($\tau(r) = 2\pi\tau/\Omega(r)$). This approach tends to reestablish the equilibrium temperature profile, after the planetary gap is opened and the system reaches a steady state.

Instead of adding cooling as a source term in the energy equation, we updated the temperature at each time step according to equation 2.12. Numerically it corresponds to

$$T^{\text{new}} = T^{\text{old}} - \frac{\Delta t}{\tau(r)}(T^{\text{old}} - T^0), \tag{2.13}$$

where T^{new} is the relaxed temperature, T^{old} would be the temperature we get from the solution of the energy equation, and Δt is the time step. We solve Equation 2.3, which describes conservation of energy, considering pressure as an independent variable. Hence, we had to convert equation 2.13 from temperature to pressure dependent, for which we used the relation $T \propto p/\Sigma$, leading to

$$p^{\text{new}} = p^{\text{old}} - \frac{\Delta t}{\tau(r)}\left(p^{\text{old}} - p^0\frac{\Sigma^{\text{new}}}{\Sigma^0}\right), \tag{2.14}$$

where p^{new} is the new pressure from the relaxed temperature, p^{old} is the pressure we get from the solution of equation 2.3, p^0 is the initial pressure, Σ^{new} is the density we get from the solution of equation 2.1 and Σ^0 is the initial density. Finally, we

cooled the disk through equation 2.14. For the locally isothermal setups, instead of using Equation 2.14 to cool the disk, we setup the sound speed to its initial profile at every time step, in order to guarantee locally isothermality.

2.1.2 Numerical setup

The simulations were carried out using the finite volume Godunov-type code PLUTO (Mignone et al., 2007). Spacial integration and time evolution were performed using the piecewise parabolic method (PPM) and second order Runge-Kutta schemes, respectively. The Harten-Lax-van Leer-Contact (HLLC) Riemann solver was used to compute the numerical fluxes and the Strang operator splitting method to solve the equations in multi-dimensions.

The HD equations were solved in a two-dimensional domain considering polar coordinates. A logarithmic grid was used for the radius and a uniform one for azimuth. The system was integrated from 0.25 au to 4.0 au in radius and from 0 to 2π in azimuth. Temporal evolution was taken up to 5000 orbits. Reflective boundary conditions were used in the radial direction and periodic conditions in the azimuthal direction. Distances are given in units of 1 au; surface densities in units of $\Sigma_0 = 10^{-4}\ M_\odot/\mathrm{au}^2$, which corresponds to a disk mass of $0.002 M_\odot$ inside the domain considered, therefore it is plausible to neglect disk self-gravity, since the Toomre parameter is $Q >> 1$ everywhere in the disk; and velocities in units of Keplerian speed at 1 au. Table 2.1 summarizes the simulations parameters.

Table 2.1 Simulations parameters

Label	M_p [a] (M_J)	R_p [b] (au)	τ [c] ($2\pi/\Omega_o$)	(N_r, N_ϕ) [d]
TR001	1.0	1.0	0.01	(512, 1024)
TR01	1.0	1.0	0.1	(512, 1024)
TR1	1.0	1.0	1.0	(512, 1024)
TR2	1.0	1.0	2.0	(512, 1024)
TR5	1.0	1.0	5.0	(512, 1024)
TR10	1.0	1.0	10.0	(512, 1024)
ISO1MJ	1.0	1.0	0.0	(512, 1024)
ISO3MJ	3.0	1.0	0.0	(512, 1024)

[a] Planet mass in terms of Jupiter mass (considering $M_\star = M_\odot$).
[b] Planet location in au.
[c] Thermal relaxation timescale in orbital units.
[d] Numerical resolution in the radial (N_r) and azimuthal (N_ϕ) directions.

2.2 General evolution

In this section we describe the system evolution for our simulations. Firstly, we present the results for the simulations with a $1M_J$ planet mass, varying the thermal relaxation timescales. Secondly, we present the results for the isothermal simulations, considering $1M_J$ and $3M_J$ planet masses.

2.2.1 Non-isothermal cases

The first set of results presented are the cases with a $1M_J$ planet and different thermal relaxation timescales. The different values of $\Omega\tau$[2] considered and their labels can be seen in Table 2.1. All the simulations presented a similar behavior, which we describe hereafter.

The formation of spiral waves takes place during the first planetary orbit. Additionally, during the first tens of orbits the planet carves out a very noticeable gap and small vortices are formed in the outer edge of this gap. In the first hundreds of planetary orbits these small vortices merge into a bigger one. Some mass remains in the gap region even after a few thousands of orbits, which can be related to the inviscid and/or non-barycentric approximations. The inviscid approximation may influence the efficiency of mass transport. Nonetheless, neglecting the indirect potential exerted on the disk due to the barycenter shift also seems to retain mass in the gap region, even for non-inviscid disks (see Figure 2 in Zhu & Stone, 2014). In the first thousands of planetary orbits a surface density enhancement appears beyond the vortex position. Accumulation of mass persists and a second vortex is formed in this region. The primary vortex is damped in different timescales for the different $\Omega\tau$'s, nonetheless some material remains in a ring-shape form in between the planetary gap and the secondary vortex. This material is also dispersed out in different timescales.

Simulations TR001 and TR01 present a secondary vortex very similar to the primary one. Figure 2.1 shows the system evolution for TR01. Simulations TR1, TR2, TR5, and TR10 present also a secondary vortex; however, the new vortex is highly spread in the azimuthal direction. Figure 2.2 shows the potential vorticity at 5000 orbits for the different $\Omega\tau$'s. For $\Omega\tau = 0.01$, the secondary vortex survives until the end of the simulation; however, the vortex gets spread along the azimuthal direction. For $\Omega\tau = 0.1$, the secondary vortex survives and does not get spread in the azimuthal direction. For $\Omega\tau \geq 1.0$, the secondary vortex is mostly damped by the end of the simulation interval.

[2]Hereafter, we refer to $\tau(r)$ as $\Omega\tau$.

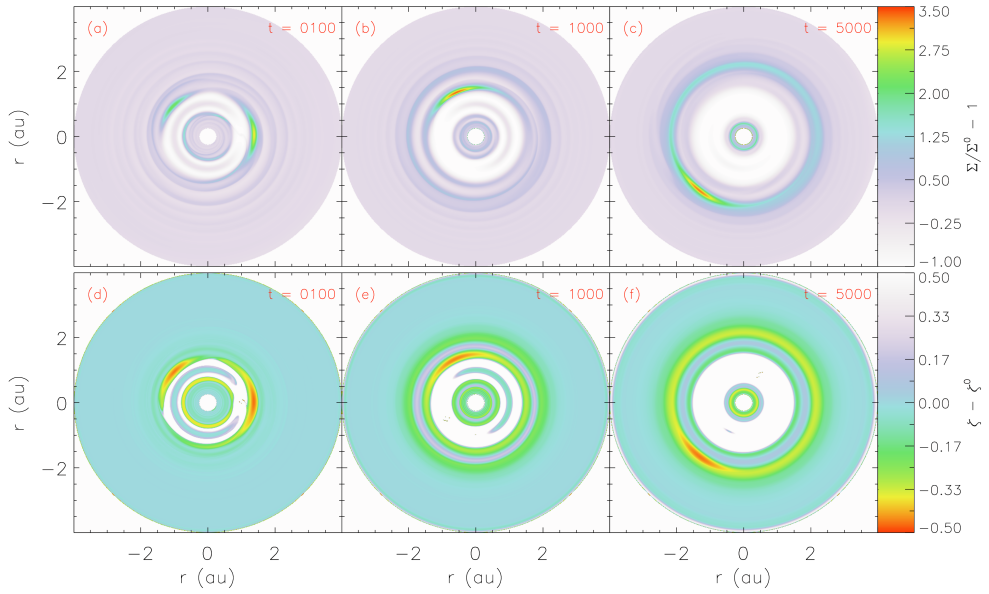

Figure 2.1 Evolution of the surface density perturbation (top panel) and the potential vorticity with the Keplerian profile subtracted (bottom panel). The color bar for the potential vorticity plots was truncated from −0.5 to 0.5, in order to provide a higher contrast. The results show simulation TR01.

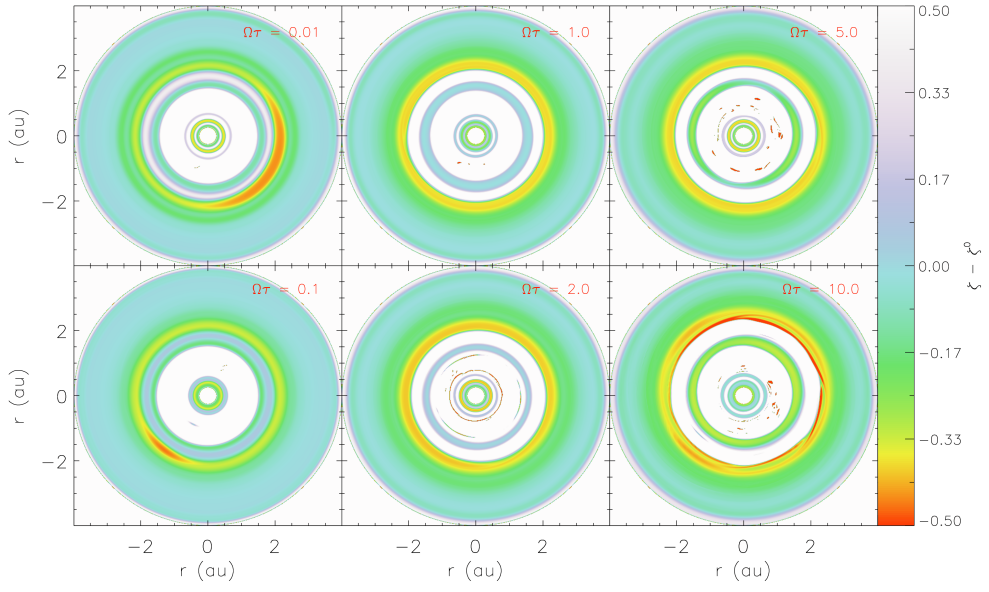

Figure 2.2 Final potential vorticity with the Keplerian profile subtracted for the different $\Omega\tau$'s considered.

2.2.2 Isothermal cases

Here we present the results for the isothermal setup and planet masses of $1M_J$ and $3M_J$. The simulations labels are presented in Table 2.1.

The isothermal configuration shows a considerably similar behavior as the models with thermal relaxation. For the ISO1MJ simulation, the sequence of events is the same. We firstly observe the formation of spiral waves, followed by planet gap opening, and production of small vortices at the outer edge of this gap. The small vortices gather together and merge into a bigger one. A surface density enhancement appears beyond the primary vortex position. Material is accumulated at this location and a second vortex arises, this structure gets spread in the azimuthal direction with time. The primary vortex gets damped and the material in between the planetary gap and the secondary vortex disperses out. The timescales for the events are similar to the ones for the non-isothermal cases.

The ISO3MJ simulation presents a similar sequence of events, with the difference that two vortices, that do not merge with time, are created in the outer edge of the planetary gap. The evolutionary timescales for which different structures form are also different. The surface density enhancement appears in hundreds of planetary orbits, instead of thousands. The damping of the primary vortices is also faster. Pile-up of material at the surface density enhancement also happens. Nonetheless, it takes thousands of planetary orbits for a secondary vortex to arise. After a few thousands of planetary orbits the material between the planetary gap and the secondary vortex is totally dispersed out, and a much wider gap is settled. Figure 2.3 shows the system evolution for simulation ISO3MJ.

It was not possible to consider a higher planet mass (e.g., $10M_J$) under the setup assumed, because the gap created is much wider, which makes the disk size considered too small. To solve the same structures in a bigger disk, we would need to use more grid cells.

2.3 Vortex formation and evolution

In a protoplanetary disk, we know that vortex formation can happen as a product of the RWI (Lovelace et al., 1999; Li et al., 2000) and/or radial buoyancy (Klahr & Bodenheimer, 2003; Lesur & Papaloizou, 2010; Klahr & Hubbard, 2014). In this chapter, we considered initially buoyantly unstable disks. Nonetheless, we know that the presence of a planetary gap naturally triggers the RWI, due to the sharp surface density gradient that is created in the gap edges. Hereafter, we discuss the role that the RWI and radial buoyancy played for the formation and evolution of

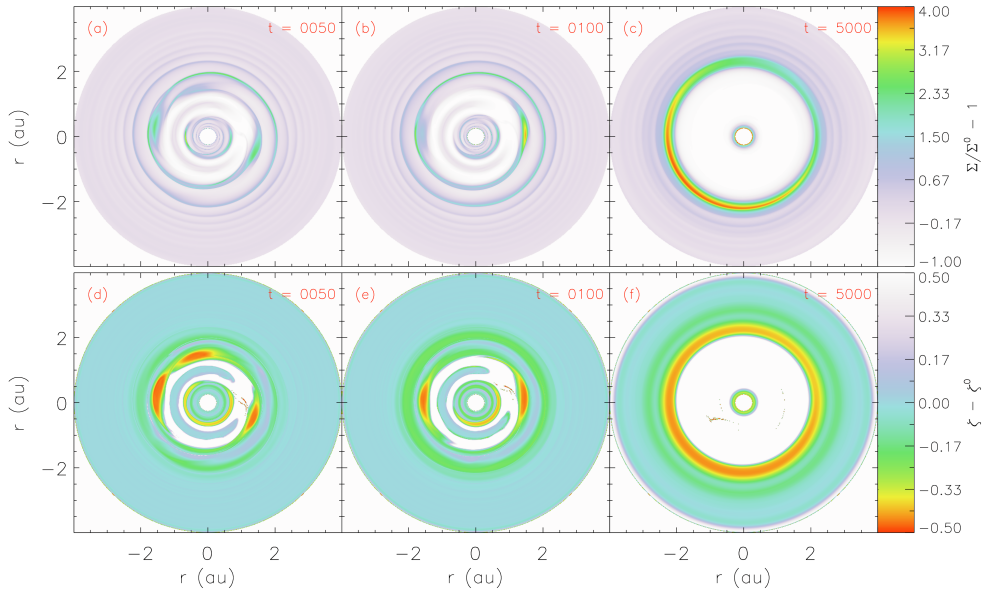

Figure 2.3 Evolution of the surface density perturbation (top panel) and the potential vorticity with the Keplerian profile subtracted (bottom panel). The color bar for the potential vorticity plots was truncated from -0.5 to 0.5, in order to provide a higher contrast. The results shows simulation ISO3MJ.

planet-induced vortices. We would like to remember that we are using an inviscid approximation, thus any viscosity in the system is turbulence-triggered viscosity by the hydrodynamical instabilities. We chose to consider an inviscid approximation to assess the direct influence of radial buoyancy and the RWI for the vortices evolution.

2.3.1 Rossby wave instability

The RWI is a pressure driven instability for rotating systems, which is composed of non-axisymmetric modes. The RWI is triggered when there is a local maximum in the radial profile of the function (Lovelace et al., 1999)

$$\mathcal{L}(r) \equiv \mathcal{F}(r) S^{2/\gamma}(r), \tag{2.15}$$

where $\mathcal{F}^{-1} = (\vec{\nabla} \times \vec{v}) \cdot \hat{z}/\Sigma$ is the potential vorticity[3] and $S = p/\Sigma^{\gamma}$ is an equivalent to the entropy. Physically, this condition can be achieved at the edge of planetary gaps (de Val-Borro et al., 2007) and the edge of dead zones due to sharp viscosity transitions (Lyra & Mac Low, 2012).

The formation of vortices as a product of the RWI has been studied by many authors. The growth rate of the instability for 2D disks was studied by Li et al.

[3]Hereafter, called as ζ instead of $\mathcal{F}^{-1}$.

(2000) and Umurhan (2010), using different approximations, and in 3D stratified disks by Meheut et al. (2012b) and Lin (2012b). The nonlinear phase of the instability was explored by Meheut et al. (2013). Despite the theory for the RWI was developed for adiabatic disks (Li et al., 2000), most of the works used locally isothermal disks to study the formation and evolution of planet-induced vortices (Balmforth & Korycansky, 2001; de Val-Borro et al., 2007; Lyra et al., 2009a; Lin & Papaloizou, 2011b; Zhu et al., 2014; Fu et al., 2014). Just recently, Les & Lin (2015) made a breakthrough and added an artificial source of cooling and heating to explore the non-isothermal behavior. In this context, our work is a second step to the process of understanding the non-isothermal scenario.

It is not in the scope of this chapter to make an extensive study of the growth and decay of the RWI, since this matter was already addressed by Les & Lin (2015) for a physical scenario very similar to ours. In order to have just a qualitative insight, we analysed the spacetime evolution of the potential vorticity (ζ) averaged in azimuth. Figure 2.4 shows the result for simulation TR01.

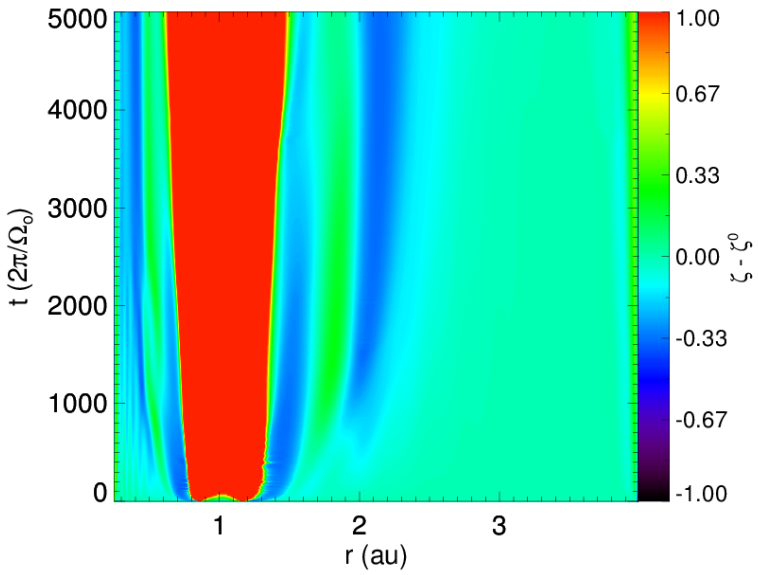

Figure 2.4 Spacetime evolution of the potential vorticity (ζ) averaged in azimuth for simulation TR01. The Keplerian profile was subtracted. The color bar was truncated from -1.0 to 1.0 in order to obtain a higher contrast.

The blue region in Figure 2.4 represents a minimum in ζ. A minimum in ζ is equivalent to a maximum in $\mathcal{L}$ (Equation 2.15), sufficient condition to trigger the RWI. This minimum is achieved in both, the outer edge of the planetary gap and at the surface density enhancement outwards the primary vortex position. Therefore, the RWI has been triggered in both regions. The presence of the minimum is maintained along the whole simulation interval. In the planetary gap edge, its

value slowly increases with time, which explains the vortex decay. In the surface density enhancement outwards the primary vortex position, its value is kept slightly constant with time, which explains the survival of the secondary vortex until the end of our simulation. The spacetime evolution of ζ is similar for all the cases. A local minimum is observed in the regions of the primary and secondary vortices. The main differences are the size of the blue regions (local minimums), the time the local minimum related the primary vortex starts to decay, and the time the local minimum related to the secondary vortex appears.

2.3.2 Radial buoyancy

The necessary ingredients for a CO and SBI are: (i) radial pressure and entropy gradients possessing the same sign (radial buoyancy) and (ii) thermal relaxation, with maximum amplification for $\Omega\tau \simeq 1.0$. The formation of vortices due to the BI was first observed by Klahr & Bodenheimer (2003). Further studies by Petersen et al. (2007a,b) showed the importance of thermal relaxation for baroclinic vortex amplification. They found that thermal relaxation or diffusion, besides entropy gradient, are required to keep the instability in action. Lesur & Papaloizou (2010) studied baroclinic vortex amplification through the growth of existing vortical perturbations. In order to not cause confusion between the generation of vortices by the classical BI and amplification of the vortices in a radial buoyant fluid, they coined this process a SBI. A parametric study covering the important ranges of entropy gradients, thermal diffusion timescales, and thermal relaxation timescales for PPDs was carried out by Raettig et al. (2013). They showed the importance of baroclinic effects even for small entropy gradients, which is the case in PPDs. Klahr & Hubbard (2014) found a linear amplification of epicyclic oscillations in radially stratified and vertically unstratified disks, which they called convective overstability. This phenomenon can be regarded as the linear phase of the SBI. Yet not much efforts were made to study how vortex formation and amplification proceeds in a buoyantly unstable disk with a high mass planet embedded. Les & Lin (2015) discussed briefly whether an axisymmetric instability was at play in their simulations of planet induced vortices; however, they concluded that only the RWI was in action.

We can quantify the radial stability in a disk with regards to convection through the Brunt-Väisälä frequency (N), which is given by (Raettig et al., 2013)

$$N^2 = -\beta_p \beta_S \frac{1}{\gamma} \left(\frac{H}{r}\right)^2 \Omega^2, \tag{2.16}$$

where β_p is the pressure gradient, β_S is the entropy gradient, and Ω is the angular velocity. Positive values of N^2 indicate stability. The entropy gradient for a 2D vertically integrated disk is given by

$$\beta_S = \beta_T + (1-\gamma)\beta_\Sigma, \tag{2.17}$$

where β_T is the temperature gradient and β_Σ is the surface density gradient. We made the choice for the initial surface density and sound speed gradients in a way that it gives an initial negative value for N^2 equals to -0.0018, thus favouring instability.

Figure 2.5 shows the spacetime evolution of N^2/Ω^2 averaged in azimuth for simulation TR01. We plot N^2/Ω^2 instead of N^2 to eliminate the dependence with the angular velocity. Since Ω^2 is always positive, $N^2/\Omega^2 > 0$ still indicates stability. We can see that in the outer disk N^2 is kept negative and roughly equals to its initial value, with exception for the outer boundary. The outer radial extent with negative N^2 becomes narrower throughout the simulation interval, thus the evolution of the system tends to stabilize the disk with respect to buoyancy. In the gap region and outer gap wall, N^2 becomes positive after a few tens of planetary orbits; however, there is a strip around the primary vortex position with smaller values of N^2. The strip's center possesses negative N^2 in the first tens of planetary orbits, but N^2 turns positive later on. From $\sim$ 600 orbits, N^2 becomes negative again in the central position of the vortex. The region with negative N^2 is not as large as the vortex size, thus buoyancy is not playing a major role for the evolution of the primary vortex. N^2 is positive in the region where the second generation of vortex appears, until the time that the secondary vortex arises and a strip with negative N^2 appears around the secondary vortex position. Once more, the strip width is smaller than the vortex size, indicating that buoyancy may not be playing a major role in the location of the vortex.

The behavior of N^2 for the other cases is similar to the one of TR01, with exception for TR001 and the isothermal cases. For them, N^2 becomes positive in the first tens of planetary orbits and remains positive along the whole simulation interval. This indicates that buoyancy does not play any role for the quasi-isothermal and isothermal cases. Reinforcing the findings of Petersen et al. (2007a,b), in the lack of thermal relaxation or diffusion, buoyancy is not sustained. For $\Omega\tau \geq 1.0$, the strip around the position of the primary vortex has negative N^2 during a larger fraction of the primary vortex lifetime. The strip around the secondary vortex is wider, indicating that buoyancy had more importance for the secondary vortex evolution than in the case that $\Omega\tau < 1.0$.

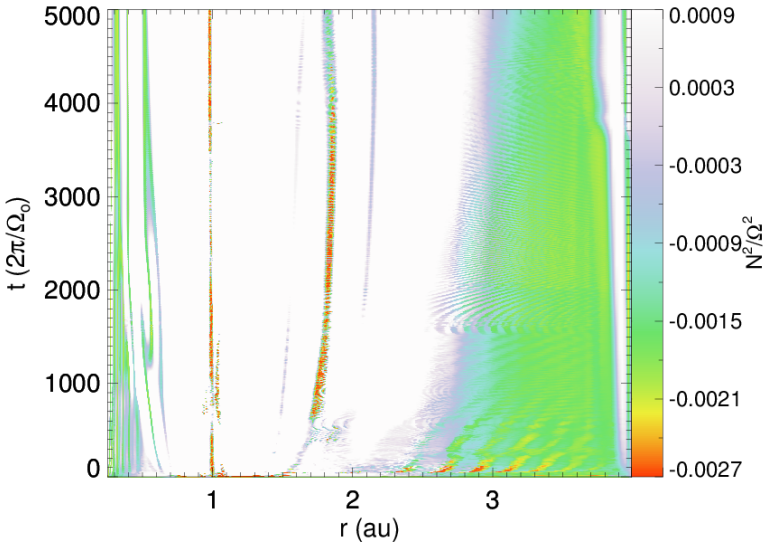

Figure 2.5 Spacetime evolution of N^2/Ω^2 averaged in azimuth for simulation TR01. The color bar was truncated from $1.5(N^2/\Omega^2)_{ini}$ to $-0.5(N^2/\Omega^2)_{ini}$, in order to provide a higher contrast.

To check the impact that buoyancy has in the results, we used a model where the initial N^2 is positive. We run the new simulation with the same physical and numerical setup as for the TR01 case, but changing the surface density gradient from $\beta_\Sigma = 1.5$ to $\beta_\Sigma = 3.0$. The general evolution of the system was very similar to the case where N^2 is initially negative. Two major differences were noticed. The first is regarding the maximum amplitudes that the primary and secondary vortices achieve, which is higher for the case where N^2 is initially positive. The second is regarding the second generation of vortices. For the $N^2_{\rm ini} > 0$ case, two vortices arise in the surface density enhancement region and take more time to merge (~ 1000 orbits against ~ 500 orbits for the reference case). The secondary merged vortex has also an aspect ratio much smaller than the secondary vortex for the $N^2_{\rm ini} < 0$ case. Figure 2.6 presents a comparison of the surface density profiles for the $N^2_{\rm ini}$ positive and negative cases, for two different points in time ($t = 250$ orbits and $t = 2500$ orbits).

The planetary gap structure is very similar for the different surface density slopes, the same width and lower level for the depth are observed, as well as the same location for the maximum and minimum surface density perturbations. The standing difference is the sharpness of the surface density gradient in the planetary gap edge and at the surface density enhancement beyond the primary vortex position. A larger gradient produces stronger vortices, therefore the vortices for $N^2_{ini} > 0$ are stronger. The times chosen to compare the cases represent a

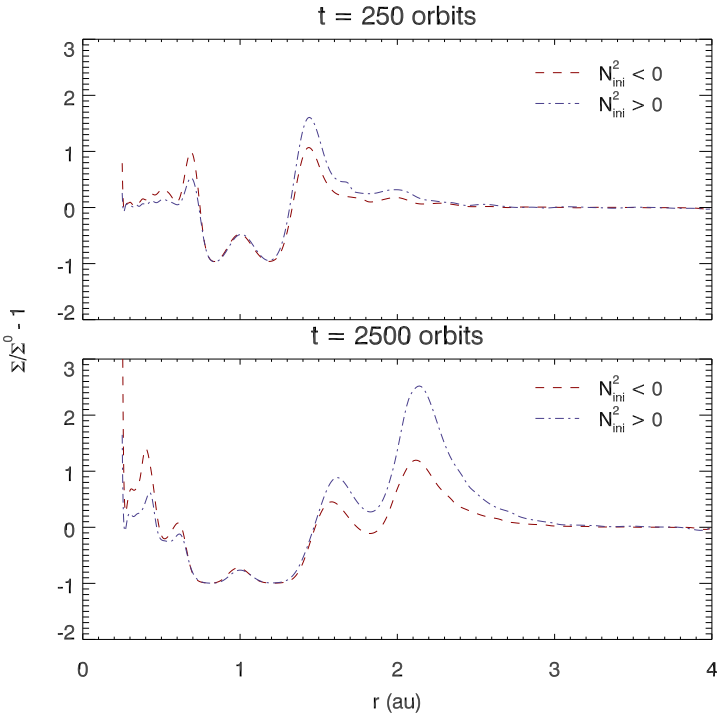

Figure 2.6 Surface density profiles averaged in azimuth. The red dashed line shows N^2 initially negative, whereas the slate blue dotted-dashed line N^2 initially positive.

moment the vortices are totally merged. The spacetime evolution of N^2/Ω^2 for $\beta_\Sigma = 3.0$ (Figure 2.7) shows that N^2 becomes negative in the first tens of orbits in the region where the primary vortices arise; however, it becomes positive again and local buoyancy disappears for hundreds of orbits, N^2 becomes negative again from ~ 700 orbits. The strip with negative N^2 around the vortex position is again not as wide as the vortex size, indicating that buoyancy is not playing a major role for the evolution of the primary vortex. Nonetheless, this shows that initially buoyantly stable disks can undergo an inversion of sign for the entropy gradient, therefore turning on instability. In the secondary vortex region, N^2 never turns to be negative. The RWI is the only responsible for the formation and sustenance of the secondary vortex.

This result demonstrates that when we have the RWI and buoyancy acting at the same time, weaker vortices are produced. Therefore, buoyancy opposes vortex amplification and survival, in this scenario. Taking into account that these processes provide viscosity to the system, once we have both in action more viscosity is produced. More viscous disks carve out smoother gaps, leading to the weaker vortices. It should also be noticed that for $\Omega\tau \geq 1.0$, the secondary vortices get

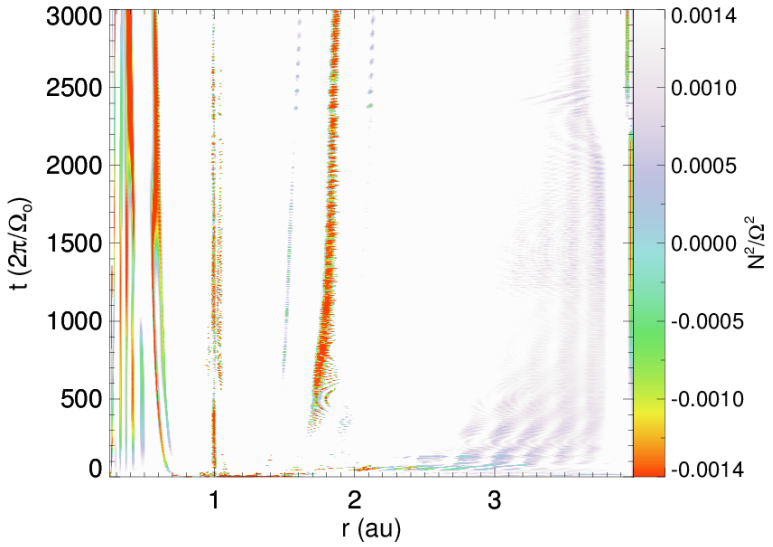

Figure 2.7 Spacetime evolution of N^2/Ω^2 averaged in azimuth for the simulation with $N^2_{ini} > 0$. The color bar was truncated from $-(N^2/\Omega^2)_{ini}$ to $(N^2/\Omega^2)_{ini}$, in order to provide a higher contrast.

damped during the simulation interval, those are also the cases for which buoyancy plays some role for the secondary vortex evolution.

2.4 Code control

In this section, we explore the numerical factors that could influence the physical validity of our simulations. The tests were done using the TR01 case as reference. The physical conditions and numerical setup were exactly the same as for TR01, varying only what we following mention. We checked the convergence of the results considering a higher numerical resolution. We analysed whether our reflecting boundary conditions for the radial direction may have reflected waves, influencing the evolution of the system. A different way to prevent boundary effects is to push the outer disk to a larger radius, hence we also used this approach to check whether the disk size influenced the results. Lastly, we added the planet along a larger number of planetary orbits to analyse whether the initial planet disturbance could have been too large, generating fake effects.

For the numerical resolution test, we doubled the number of grid cells from (N_r, N_ϕ) = (512, 1024) to (N_r, N_ϕ) = (1024, 2048). The temporal evolution was taken up to 1000 planetary orbits. The full temporal evolution was not checked, because the doubled resolution is numerically highly expensive. For the boundary conditions test, we first changed the inner and outer radial boundary conditions from reflective

to non-reflective, secondly we considered a larger disk extending from 0.25 au to 8 au. Finally, aiming to check the effect of the initial planet disturbance to the disk, we made two tests: slowly adding the planet along its first 10 and 100 orbits, following Equation 2.9, in the reference case the planet was slowly added along its first orbit. The temporal evolution for the last four tests was taken up to 5000 planetary orbits.

We compare our test cases with the reference case using their surface density profiles at the latest snapshot. Figure 2.8 presents these profiles for $t = 1000$ orbits (numerical resolution comparison) and $t = 5000$ orbits (other comparisons). We observed a good agreement for the surface density profiles, indicating that the simulation results were not much influenced by these factors. Nonetheless, for the resolution test, the outer gradient that leads to the second generation of vortices is slightly smoother than for the standard case.

For the boundary condition test, in the outer disk ($r \gtrsim 3$ au) the material is emptied out, due to the boundary choice; however, the main results agree with the standard case. The major difference is regarding the secondary vortex, for the standard case a secondary merged vortex is created, in this case two secondary vortices are created and they do not merge until the end of the simulation. The two secondary vortices, for the non-reflecting radial boundaries, are right opposite to each other in the azimuthal direction and they have about the same strength. We speculate that the flow in the corotation region of these vortices is not being able to push them together, exactly because the vortices have the same strength and are located right opposite to each other, leading to a stable configuration. For the larger disk size, the standing difference is regarding the local minimum between the surface density bumps, where the primary and secondary vortices sit. For the standard case, the local minimum is still present by the end of the simulation. For the larger disk size, this local minimum has disappeared by the end of the simulation, meaning that the matter is dissipating slightly faster.

For the planet being added along the first 10 orbits, the primary small vortices merge in a faster timescale, and the vortices amplitudes take a longer time to grow than for the standard case. For the planet being added along the first 100 orbits, the vortices amplitudes take also a longer time to grow than for the standard case. Higher planet masses can excite stronger vortices (Fu et al., 2014), thus when the planet perturbation is added slower, the vortices will also take a longer time to grow.

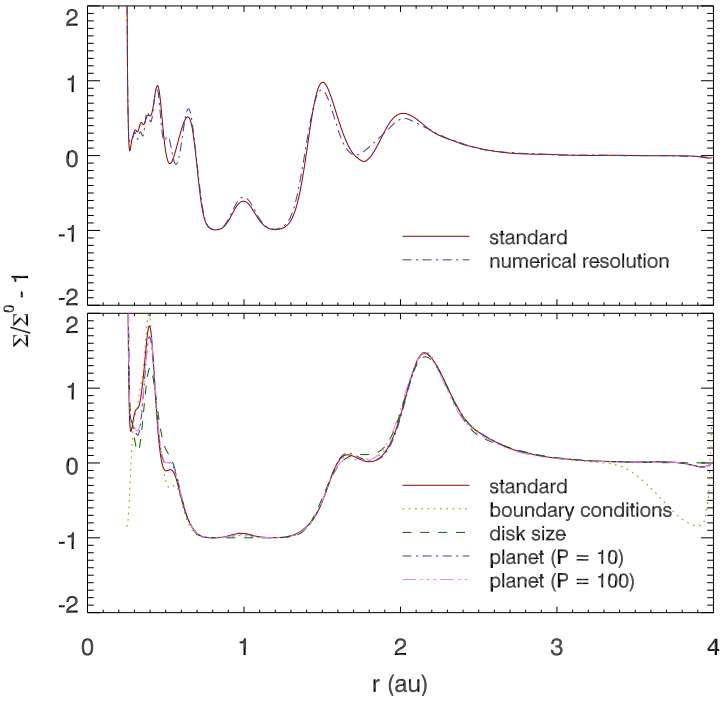

Figure 2.8 Surface density profiles (averaged in azimuth) at 1000 orbits (top panel) and 5000 orbits (bottom panel). The top panel presents the comparison for the numerical resolution test. The red solid line shows the reference case, whereas the slate blue dotted-dashed line the numerical resolution test. The bottom panel presents the comparison for the other cases. The red solid line shows the reference case, the goldenrod dotted line shows the boundary conditions test, the green dashed line shows the disk size test, the slate blue dotted-dashed line shows the planet disturbance test (the planet was added during its first 10 orbits), and the violet triple-dotted-dashed line shows the planet disturbance test (the planet was added during its first 100 orbits).

2.5 Second generation of vortices

The most interesting result of our simulations is the second generation of vortices. A surface density enhancement was observed beyond the primary vortex position for all the cases. This bump is strong enough to trigger the RWI outside the primary vortex radius and to form a second generation of vortices. As it was discussed before, we observe a minimum for ζ in the region of the secondary vortex for all the cases. Also, there are strips of negative N^2 in the region of the secondary vortex, with exception for the TR001 and the isothermal cases. Once more, the action of the RWI together with buoyancy controls the vortex evolution. For the TR001 and isothermal cases, the RWI is solely responsible for the secondary vortex. We already established that our results were not affected by the choice of boundary conditions, resolution, or the planet perturbation being too sharp. Therefore, it

confirms the physical origin of the second generation of vortices. No further density enhancement (strong enough to keep triggering the RWI) beyond the secondary vortex position was observed, even for the test simulation with a larger disk, thus we do not expect a third generation of vortices.

2.5.1 The origin of the secondary vortex

Accumulation of mass is observed at the inner boundary for all the cases. Our understanding is that the primary vortices produce an effective α-viscosity that is large enough to induce accretion in the disk in the timescales we simulate. Therefore mass is flowing from the region of the primary vortex to the inner disk. The depletion of mass in the orbit of the primary vortex position looks like a gap carved out by the primary vortex. In fact, the outer wall of the planetary gap is moving outwards due to this depletion of mass. For instance, for the ISO3MJ case, by the end of our simulation all the mass in the orbit of the primary vortex was already depleted and the planetary gap became wider in its outer side. Figure 2.9 presents the inner disk mass as a function of time for simulation TR01, where the increase of the mass is demonstrated.

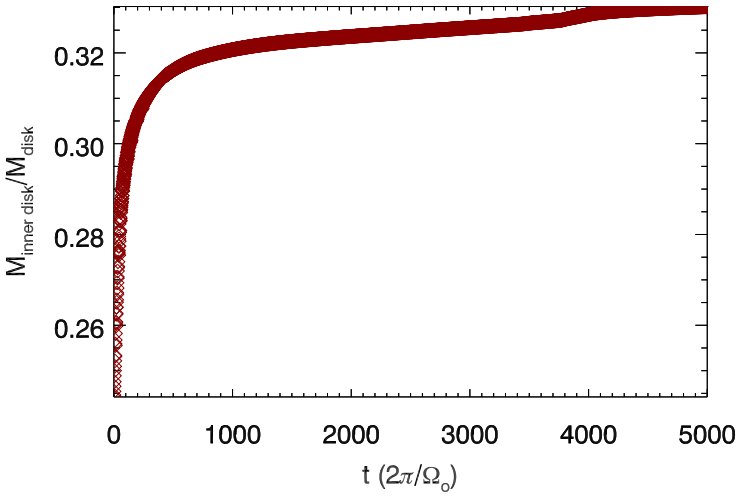

Figure 2.9 Inner disk mass as a function of time for simulation TR01. We consider 0.25 au $\leq r \leq$ 0.75 au as the inner disk.

The faster mass increase happens in the first tens of orbits, when the planet still carving out its gap. During this period, the mass increase is mostly due to the planetary gap opening process. The inner disk mass is being pushed from $r = 1$ au to the inner parts of the disk. For $t \gtrsim 100$ orbits, the mass increase is most likely due to accretion induced by the primary vortex. Our simulations assumed an

inviscid disk, therefore any viscosity is produced by the hydrodynamical instabilities, which in this case could be named a vortex-induced viscosity. We can obtain an estimate of the α-parameter, using the $r-\phi$ component of the Reynolds stress and the local sound speed (Flock et al., 2011). For simulation TR01, the α-parameter averaged in space and time (until the time the secondary vortex appears) was $\alpha \simeq 3 \times 10^{-3}$, a value in the range of what is typically obtained by the MRI, $\alpha = 10^{-4} - 10^{-2}$ (Dzyurkevich et al., 2010). The other simulations presented values in the range from $\alpha = 10^{-4} - 10^{-2}$, in agreement with MRI. The lowest value obtained was $\alpha \simeq 6 \times 10^{-4}$, for TR1, and the highest value was $\alpha \simeq 1 \times 10^{-2}$, for TR5. Large-scale vortices are able to transport angular momentum outwards, because a negative angular momentum flux is obtained from the balance between the angular momentum carried by Rossby waves in the inner and outer sides of a surface density bump (Meheut et al., 2012b).

In this chapter we assumed that the barycenter of the system is located at the star's center. This approximation could influence the gap structure, since the Lagrange point L3, in the corotation region of the planet, is removed. Changes in the gap structure may affect the primary vortex generation, subsequently possibly impacting the second generation of vortices. This assumption summed to the inviscid disk approach are two factors that could influence the formation of a second generation of vortices. We suggest that further studies should check these factors.

2.5.2 Pressure bumps

Vortices are able to trap dust particles, because they are local pressure bumps. The particles are attracted to the highest pressure region, thus to the vortex center. The secondary vortex becomes extensively spread in the azimuthal direction for $\Omega\tau \geq 1.0$ and $M_p = 3M_J$. In order to make sure that these nonaxisymmetric structures can still trap dust particles, we checked their pressure profiles. Figure 2.10 shows a radial cut of the pressure for ϕ equals to the vortex center and an azimuthal cut of the pressure for r equals to the vortex center. We show the cases of $\Omega\tau = 10.0$ and $M_p = 3M_J$, since these are the simulations that present the most spread vortices in the azimuthal direction. We can observe a pressure bump in both radial and azimuthal directions; however, in the azimuthal direction the bump of ISO3MJ is very smooth. Birnstiel et al. (2013) showed that a very smooth pressure bump in the azimuthal direction is still sufficient to trap mm and cm particles in the vortex center. Therefore the secondary vortices should be able to trap dust particles, leading to an asymmetric global dust distribution.

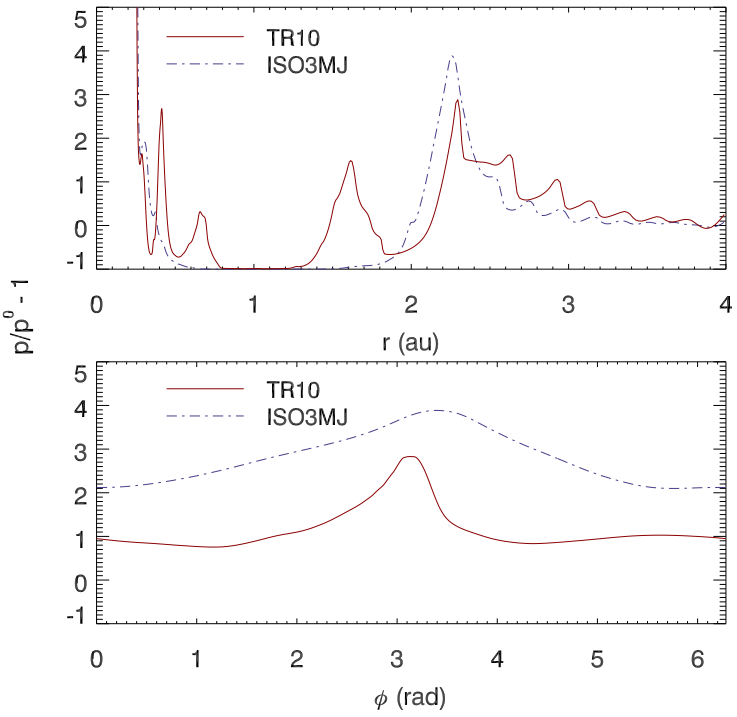

Figure 2.10 Pressure perturbation at $t = 3500$ orbits. The top panel shows a cut of the pressure for ϕ equals to the secondary vortex center. The bottom panel shows a cut of the pressure for r equals to the secondary vortex center. The red solid line represents simulation TR10, whereas the slate blue dotted-dashed line represents simulation ISO3MJ.

2.5.3 Oph IRS48

The system Oph IRS48 is a good candidate to host a vortex-like structure induced by a planet (van der Marel et al., 2013). The continuum emission ALMA observations at 0.44 mm revealed a high-contrast asymmetry in the disk of this system, which was interpreted as existing due to the presence of an anticyclonic vortex (van der Marel et al., 2013). Besides, this system shows a central cavity in CO line observations, which was explained as a gap opened by a massive planet (Brown et al., 2012). van der Marel et al. (2013) ran a FARGO simulation considering the parameters of this system to get the gas density distribution. Later on the result from the HD simulation was used as the initial condition in a dust evolution code to get the expected continuum emission. They were able to roughly reproduce the ALMA observation; however, there is a debate regarding the location of the vortex. If the planet is located at 20 au, the vortex is expected to be located at most at ~ 45 au, nonetheless it is located at ~ 63 au.

We run a simulation using the same setup as van der Marel et al. (2013), with the difference that here no viscosity was included, but instead we used thermal relaxation, and initialized the disk with H/r constant. We observed vortex formation at the outer edge of the planetary gap, the vortex position is roughly 40 au; however, we did not observe a second generation of vortices. The disk considered was much larger (from 2 to 150 au) than the one of our benchmark cases (from 0.25 to 4.0 au), therefore the resolution may not have been sufficient to solve the secondary vortex. Figure 2.11 shows the potential vorticity for this simulation after 700 planetary orbits. We can see that ζ is negative around 60 au, therefore a secondary vortex could be formed in that region.

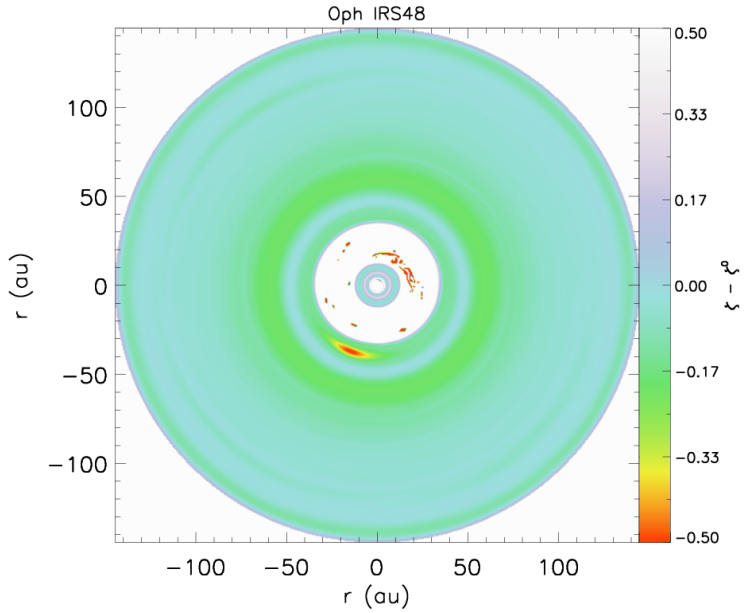

Figure 2.11 Potential vorticity with the Keplerian profile subtracted for $t = 700$ orbits. The color bar was truncated from -0.5 to 0.5 in order to obtain a higher contrast.

The ratio between the positions of the secondary and primary vortices in our benchmark cases is about 1.5. If this ratio is fixed, the second generation of vortices in the Oph IRS48 system would be located at ~ 60 au. In order to check whether the secondary vortex was not observed due to a numerical resolution problem, we run a second simulation considering the same planet-disk setup as before, but integrating over a smaller disk size. We fixed the inner and outer disk radius, in order to maintain the same ratio between the planet orbital distance and the boundaries as for the benchmark cases. The new simulation has a disk ranging from 5 au to 80 au. Figure 2.12 shows the potential vorticity for the smaller disk size after 700 planetary orbits. Here, we can see the formation of a secondary

vortex, located at $\sim$ 62 au, indicating that in the previous case the numerical resolution was indeed not sufficient. This new result is a promising explanation for the location of the Oph IRS48's vortex, assuming a single planet at $\sim$ 20 au distance from the star. It is also important to mention that at 700 planetary orbits, the primary and secondary vortices are present. The benchmark cases show that the primary vortex get damped before the secondary one, thus for later times, just the secondary vortex may be present.

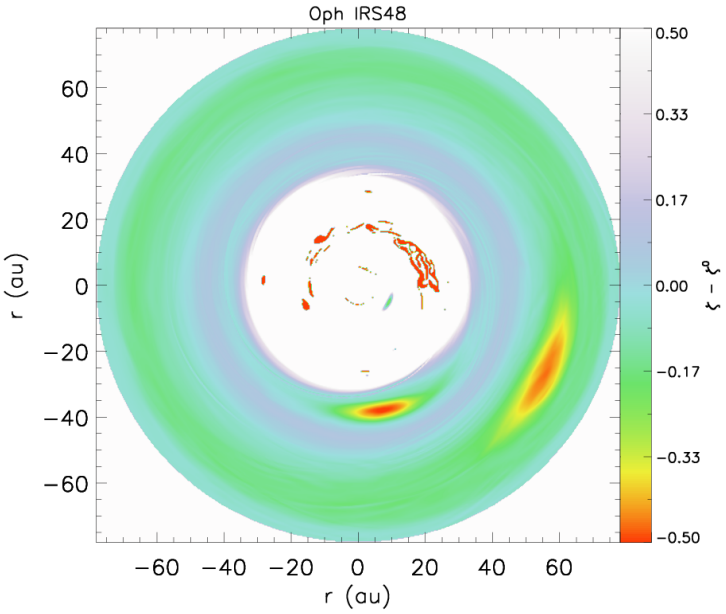

Figure 2.12 Potential vorticity with the Keplerian profile subtracted for $t = 700$ orbits. The color bar was truncated from -0.5 to 0.5 in order to obtain a higher contrast.

2.6 Vortex lifetimes and birth times

In this section we obtain the primary vortex lifetime and secondary vortex birth time as a function of the thermal relaxation timescale. For this purpose, we firstly had to define when the vortex is born. Once an overdensity with negative potential vorticity arises, we declare that this overdensity is a vortex. We define as overdensity a region that possesses an average surface density at least 20% higher than the average background surface density.

The center of the vortex was defined as the position of the maximum surface density. We determined the vortex edge by looking to the position where the potential vorticity drops to 50% below its value at the vortex center. This procedure was done in both radial and azimuthal directions. Knowing the dimensions of the

vortex, we could calculate the average surface density and potential vorticity inside the vortex.

The procedure of finding the vortex and defining its border was done until the time that the vortex cannot be defined as an overdensity anymore. Once this criterion was reached we defined the vortex as dead. In this way, the vortex lifetime was defined as the difference between the time it is born and the time it dies.

Figure 2.13 presents the primary vortex lifetime as a function of the different thermal relaxation timescales. We observe a nonmonotonic behavior that was already seen by Fu et al. (2014) and Les & Lin (2015). Les & Lin (2015) explained that the nonmonotonic behavior is due to the fact that the vortex lifetime depends on (i) the decay timescale of the RWI, which decreases for increasing $\Omega\tau$, and (ii) the vortex growth time, which increases for values of $\Omega\tau$ up to ~ 5.0 and then decreases for larger values. The nonmonotonic nature is a result of this double dependence. The double peak, featuring at small $\Omega\tau$'s and $\Omega\tau = 5.0$, is due to the nonmonotonic behavior of the vortex growth time for different $\Omega\tau$'s. Higher disk temperatures favours the RWI (Li et al., 2000; Lin, 2012a), nevertheless this effect seems to be important just for larger $\Omega\tau$'s. The dependence of the vortex lifetime with the vortex growth time comes to the fact that once the vortex amplitude is very large, it begins to induce shocks, thus the vortex looses energy through shock dissipation and starts to decay. The inviscid approximation may have influenced the estimation of the vortex lifetimes, since it is inversely dependent on the viscosity magnitude (de Val-Borro et al., 2007; Ataiee et al., 2013; Fu et al., 2014). Nonetheless, it is clear that it did not influence the qualitatively behaviour of vortex lifetimes as a function of thermal relaxation timescales, since our results are in agreement with Fu et al. (2014) and Les & Lin (2015).

We also plot in Figure 2.13 the time when the secondary vortex is born. A nonmonotonic behavior is also observed and the curves are shifted by a few hundreds of planetary orbits, with exception for $\Omega\tau = 10.0$. Since the primary vortex is born in a scale of tens of planetary orbits, it is clear that the secondary vortex is always born before the death of the primary vortex, again with exception for $\Omega\tau = 10.0$. The time taken for the secondary vortex to be born is correlated to the time that the primary vortex needs to deplete the mass on its orbit. Therefore it depends on the vortex growth time and the accretion rate generated by the primary vortex. This explains the inverse dependence of the secondary vortex birth time and primary vortex growth time as a function of the thermal relaxation time scale.

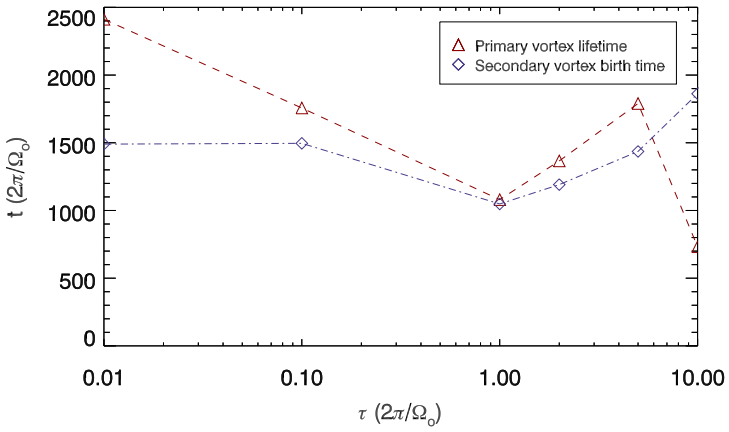

Figure 2.13 The lifetime of the primary vortex (red dashed line) and the birth time of the secondary vortex (slate blue dotted-dashed line) as a function of the thermal relaxation timescale.

2.7 Summary and conclusions

Vortices can be formed as a product of the RWI and/or unstable radial buoyancy (BI/SBI/CO). The RWI can be triggered in the walls of a planetary gap due to a sharp surface density gradient. The disk is buoyantly unstable when the pressure and entropy gradients have the same sign, a thermal relaxation of the order of $\Omega\tau \simeq 1.0$ also favours vortex amplification. We carried out global 2D-HD simulations of planet-disk interactions, using the PLUTO code. The aim was to study the long-term evolution of planet-induced vortices in inviscid disks and initially buoyantly unstable, considering several thermal relaxation timescales. Thermal relaxation is an important ingredient to sustain radial buoyancy (Petersen et al., 2007a,b). It has also a strong impact on amplifying and damping vortices.

We found that radial buoyancy smoothen the surface density gradients in the wall of a planetary gap, which generates weaker vortices. In this particular physical scenario, radial buoyancy operates against vortex amplification and survival. This effect is less pronounced for the isothermal and quasi-isothermal states ($\Omega\tau << 1$), which is expected, since thermal relaxation is a required ingredient to sustain radial buoyancy. The qualitative system evolution is similar for different thermal relaxation timescales and different planet masses. The major difference is regarding the timescales of events (e.g., time required for vortex damping and mass transfer).

The most interesting result from our simulations was the formation of a second generation of vortices. The primary vortex creates an effective α-viscosity that is large enough to induce accretion. We obtained α-values in the range $\alpha = 10^{-4} -$

10^{-2}, which agrees with what is obtained by the MRI (Dzyurkevich et al., 2010). The accretion process depletes the mass in the primary vortex orbit, creating a density enhancement outwards the vortex position. This bump is sufficient to trigger the RWI, leading to the secondary vortex formation. This result is a promising explanation for the location of the vortex in the Oph IRS48 system (van der Marel et al., 2013), which is located at ~ 63 au. Previous models predicted that the vortex location could be at most at ~ 45 au, assuming a single planet at ~ 20 au. Our model suggests that a second generation of vortices can be formed at ~ 62 au, if a massive planet ($5M_J$) is assumed at 20 au. We suggest that further works should test the formation of a second generation of vortices in non-inviscid disks and considering a proper treatment of the system's barycenter location, since these factors may influence the generation and sustenance of vortices.

We observed a nonmonotonic behavior for the vortex lifetime as a function of the thermal relaxation timescale. This result was already observed by Fu et al. (2014) and Les & Lin (2015). The vortex lifetime depends on the decay of the RWI and the vortex growth time. The former decreases as a function of the thermal relaxation timescale. The latter increases as a function of the thermal relaxation timescale up to $\Omega\tau = 5.0$, decreasing for larger $\Omega\tau$'s. The nonmonotonic behavior and double peak observed for the vortex lifetime is a result of this double dependence. The birth time of the secondary vortex also presents a nonmonotonic behavior. The appearance of the secondary vortex is correlated to the time the primary vortex needs to deplete the mass on its orbit. Therefore it is linked to the primary vortex growth time and the accretion rate generated by it. It is important to remember that we considered an inviscid disk. Previous works have shown that the vortex lifetime is inversely dependent on the viscosity magnitude (de Val-Borro et al., 2007; Ataiee et al., 2013; Fu et al., 2014). All the viscosity in our models is turbulence-triggered by the hydrodynamical instabilities. The inviscid approximation may have quantitatively changed the vortices lifetimes; however, it did not change the qualitative behaviour of vortices lifetime as a function of thermal relaxation timescales.

Chapter 3

Type I migration in radially stratified turbulent disks

The work presented in this chapter is from **Lobo Gomes, A.**, *Klahr, H., Surville, C., Uribe, A. L., The Astrophysical Journal, submitted.*

The study of planet migration is of major importance for the understanding of planet evolution, bearing in mind that this process is crucial to explain the observed mass-distance distribution of exoplanets (Alibert et al., 2004; Ida & Lin, 2008; Mordasini et al., 2009). The torque exerted by the disk on the planet changes its orbital angular momentum, thus leading to the radial migration of the planet. We can characterize the migration regimes into three types that are basically dependent on the planet mass.

Type II migration is experienced by high mass planets around Jupiter's mass. The massive planet carves out a gap, becoming "isolated" from the gaseous disk. Subsequently, the planet migration follows the viscous evolution of the disk (Lin & Papaloizou, 1986). Type III migration is experienced by intermediate-mass planets in the range from sub-Saturnian to Jovian masses embedded in a high mass disk. The planet should be massive enough to create a dip or open up a partial gap and the surrounding gas mass should exceed the planet mass. The deficit of mass around the planet's position makes the planet's migration to undergo a runaway process that can change the planet's semimajor axis by 50% over just a few planetary orbits (Masset & Papaloizou, 2003).

Type I migration, the subject of this study, is experienced by low mass planets of a few Earth masses (Ward, 1997; Tanaka et al., 2002). This process is governed by the differential Lindblad torque (Ward, 1986, 1988) and the corotation torque (Ward, 1989; Korycansky & Pollack, 1993; Tanaka et al., 2002). The former consists

of the torque exerted by the fluid elements located at the Lindblad ressonances on the planet. The latter consists of the torque exerted by the fluid located at the corotation region on the planet. The corotation torque used to be estimated from linear stability analysis. Recently, the nonlinear component was found to be important. This torque is now refereed to as the horseshoe drag, which includes both linear and nonlinear parts (e.g., Paardekooper & Papaloizou, 2009; Casoli & Masset, 2009). The outstanding problem of type I migration is the fast timescale predicted by isothermal models (e.g., Ward, 1986, 1989; Artymowicz, 1993b; Tanaka et al., 2002; Casoli & Masset, 2009). Different physical mechanisms were invoked to overcome this problem, such as magnetic field effects (e.g., Nelson, 2005; Baruteau & Lin, 2010; Baruteau et al., 2011; Uribe et al., 2011; Guilet et al., 2013; Uribe et al., 2015; Bans et al., 2015), planet traps (e.g., Masset, 2002; Masset et al., 2006; Morbidelli et al., 2008), and non-isothermal effects (e.g., Morohoshi & Tanaka, 2003; Paardekooper & Mellema, 2006; Baruteau & Masset, 2008a; Kley & Crida, 2008; Kley et al., 2009; Yamada & Inaba, 2011; Lega et al., 2014).

Many developments were made towards a solution for the fast type I migration timescale, when non-isothermal disks started to be examined. Morohoshi & Tanaka (2003) showed that the torque felt by a planet can strongly change due to radiative effects in optically thin disks. Paardekooper & Mellema (2006) found that the total torque increases with the disk opacity, turning to be positive (outward migration) for sufficiently high opacity values. The effect of energy dissipation by radiation was studied by Yamada & Inaba (2011) in radiatively efficient disks. They showed that when the energy is efficiently dissipated the horseshoe drag decreases and the planet migrates inwards. The migration velocity is dependent on the radiative efficiency and can be reduced for inefficient radiative cooling.

Lyra et al. (2010) used evolutionary radiative disk models to study the consequence of outwards type I migration. They found the existence of a zero torque region. Planets in an inner radius from that region migrate outwards and planets in an outer radius migrate inwards, both towards the equilibrium radius. Once they reach this location, they remain locked to the viscous and photoevaporation evolution of the disk, being decoupled once the gas surface density and temperature greatly drop. Planets of $\sim 10 M_\oplus$ do not migrate further after decoupling, whereas smaller planets from $0.1 - 1.0 M_\oplus$ released beyond 1 au, experience further inward migration, however, succeed to not fall into the central star. Dittkrist et al. (2014) studied how different migration models impact planetary populations. They found that the inclusion of non-isothermal effects can give a physical explanation for the slow migration rates required for planet population synthesis to match observations.

Yet, an aspect that is not completely understood is the mechanism that is able to maintain the horseshoe drag unsaturated, so that it balances or counteracts the Lindblad torque on a given timescale. Baruteau & Lin (2010) studied the desaturation of the horseshoe drag in isothermal disks, using a two-dimensional (2D) turbulence model that mimics the properties of three-dimensional (3D) magnetohydrodynamical (MHD) turbulence. They found that the desaturation of the horseshoe drag depends on the turbulence strength. They also pointed out the importance to study the long-term evolution of the total torques considering several hydrodynamical instabilities observed in protoplanetary discs (PPDs): the Rossby wave instability (RWI, Lovelace et al., 1999; Li et al., 2000), the baroclinic instability (BI, Klahr & Bodenheimer, 2003), the Kelvin-Helmholtz instability (KH, Johansen et al., 2006), and the magnetorotational instability (MRI, Balbus & Hawley, 1991). These instabilities may generate turbulence, which affects the horseshoe drag, potentially helping its desaturation. Therefore dedicated studies of type I migration in the presence of these instabilities should be carried. So far, most of the works were done in a MRI framework (e.g., Nelson, 2005; Uribe et al., 2011), thus more attention should be given for pure hydrodynamical instabilities.

The BI is a radial convective instability. It needs radial buoyancy to be activated, so pressure and entropy gradients with the same sign. This instability is known to create vortices. Klahr & Bodenheimer (2003) were the first ones to observe the formation of vortices in baroclinic disks. Klahr (2004) made a linear analysis of the BI and concluded that just nonlinear effects can lead to a significant amplification of vortices. Petersen et al. (2007a,b) showed that thermal relaxation or diffusion are necessary ingredients for baroclinic vortex amplification. Lesur & Papaloizou (2010) studied baroclinic vortex amplification through the growth of vortical perturbations and named the nonlinear phase of this process as the subcritical baroclinic instability (SBI). Recently, Klahr & Hubbard (2014) considered radially stratified and vertically unstratified disks and found a linear amplification of epicyclic oscillations, which they called a convective overstability (CO). This overstability can be seen as the linear phase of the SBI.

In this chapter we are interested in studying how unstable radial buoyancy can influence the type I migration behavior. In particular, whether its effects can slow down, halt, or reverse the migration rate. The chapter is organized as follows. In Section 3.1 we discuss the setup of the simulations. The impact that radial buoyancy has for type I migration is discussed in Section 3.2, where we analyse the dependence of the total torques with respect to the thermal relaxation timescales, the temperature slopes, the disk aspect ratio, and the planet masses.

The generation of turbulence in buoyantly unstable disks is studied in Section 3.3. Finally, we summarize our results and conclusions in Section 3.4.

3.1 Simulations

The physical model and numerical setup assumed for our simulations are explained in details in Chapter 2 (Lobo Gomes et al., 2015). We used the Godunov-type code PLUTO (Mignone et al., 2007) to solve numerically the 2D hydrodynamical (HD) equations. We carried out 2D-HD global simulations, using the PLUTO planet-disk module from Uribe et al. (2011) and including the thermal relaxation approach explained in Chapter 2 (Lobo Gomes et al., 2015). We applied cooling to the disk following Newton's cooling law. Perturbing agents like the planet lead to changes in the density and/or pressure of the gas, thus the temperature changes accordingly. Newton's cooling law states that the gas should return to its initial temperature, recovering equilibrium with the surrounding unperturbed gas, in a certain timescale. This timescale mimics the effects of opacity, thus it is an approach to approximate radiative effects in the disk.

Polar coordinates were considered. The domain of integration was $r \in [0.5,\ 2.0]$ and $\phi \in [0, 2\pi]$, with a numerical resolution of $(N_r, N_\phi) = (1024, 1024)$. Distances are given in units of $r_0 = 1$ au, surface densities in units of $\Sigma_0 = 10^{-4}\ M_\odot/\mathrm{au}^2$ (corresponding to a disk mass of $0.001 M_\odot$ inside the domain considered), and velocities in units of Keplerian speed $v_{K,0}$ at 1 au. The planet's orbital separation is allowed to vary. The planet is initially located at a separation of 1 au, and it was added smoothly (its mass increases from zero up to M_p) during its first orbit.

3.1.1 Initial conditions

We assumed the stationary solution of a sub-Keplerian disk as initial conditions. The initial gas surface density had a radial profile ($\Sigma \propto r^{-\beta_\Sigma}$) defined by the slope β_Σ and the initial sound speed had a radial profile ($c_s \propto r^{-\beta_T/2}$) defined by the slope $\beta_T/2$, where β_T is the temperature slope. We made the choice for β_Σ and β_T in order to maximize the effect of radial buoyancy. The Brunt-Väisälä frequency (N) quantifies the radial stability in a disk with respect to convection. We determine N^2 as in Raettig et al. (2013)

$$N^2 = -\beta_p \beta_S \frac{1}{\gamma} \left(\frac{H}{r}\right)^2 \Omega^2, \tag{3.1}$$

where β_p is the pressure gradient; β_S is the entropy gradient; γ is the adiabatic index, which we chose to be $\gamma = 1.43$; $h = H/r = c_s/v_K$ is the disk aspect ratio; and Ω is the angular velocity. Positive values of N^2 indicate stability. The entropy gradient in a vertically integrated disk is given by

$$\beta_S = \beta_T + (1-\gamma)\beta_\Sigma. \tag{3.2}$$

We can rewrite Equation 3.1 in function of the surface density and temperature gradients, using Equation 3.2 and taking into account that $p \propto T\Sigma$, obtaining

$$N^2 = -\left(\frac{h^2\Omega^2}{\gamma}\right)[2\beta_T^2 + (1-\gamma)\beta_\Sigma^2 + (2-\gamma)\beta_T\beta_\Sigma]. \tag{3.3}$$

For a fixed value of β_T, Equation 3.3 has its minimum when

$$\beta_\Sigma = -\frac{(2-\gamma)}{2(1-\gamma)}\beta_T. \tag{3.4}$$

Therefore, given a temperature slope, we defined the density slope in order to minimize Equation 3.3, or in other words, to maximize the effect of radial buoyancy. Table 3.1 presents the simulations parameters. For a $10M_\oplus$ planet, $\beta_T = 1.0$, and $h = 0.1$, we considered several thermal relaxation timescales, from $\Omega\tau = 0.1$[1] to $\Omega\tau = \infty$ (adiabatic limit). These simulations had the objective of checking how the type I migration varies with the cooling timescale. We also considered different temperature slopes to check its effect, fixing the planet mass as $10M_\oplus$, the initial disk temperature as $h = 0.1$, and the thermal relaxation as $\Omega\tau = 1.0$. To check the effect of the initial disk temperature, we used a $10M_\oplus$ planet, $\beta_T = 1.0$, and $\Omega\tau = 1.0$. Finally, the planet mass was varied fixing $\beta_T = 1.0$, $h = 0.1$, and $\Omega\tau = 1.0$.

3.1.2 Torques

Since we are interested in studying migration, we calculated the total torque exerted by the disk on the planet at each time step. The torque is given by

$$\Gamma_i = GM_p\xi \int_{\text{disk}} \Sigma(\mathbf{r}) \frac{(\mathbf{R_p} \times \mathbf{r})_i}{\sqrt{(|\ \mathbf{r} - \mathbf{R_p}\ |^2 + \epsilon^2)^3}} dA, \tag{3.5}$$

where i is the torque component; G is the gravitational constant; M_p is the planet mass; $\Sigma(\mathbf{r})$ is the surface density at a certain point; $\mathbf{R_p}$ is the planet location; dA

[1] $\Omega\tau$ is the thermal relaxation timescale in orbital units, since $\tau(r) = 2\pi\tau/\Omega(r)$.

Table 3.1 Simulations parameters

Label	M_p[a] ($M_\oplus$)	β_Σ	β_T	h	$\tau(r)$[b] ($2\pi/\Omega_o$)	T_{tot}[c] ($2\pi/\Omega_o$)
ME10t01T1h1	10.0	0.66	1.0	0.1	0.1	2000
ME10t1T1h1	10.0	0.66	1.0	0.1	1.0	5000
ME10t2T1h1	10.0	0.66	1.0	0.1	2.0	5000
ME10t5T1h1	10.0	0.66	1.0	0.1	5.0	2000
ME10t10T1h1	10.0	0.66	1.0	0.1	10.0	2000
ME10tinfT1h1	10.0	0.66	1.0	0.1	∞	2000
ME10t1T0h1	10.0	0.66	0.0	0.1	1.0	2000
ME10t1T05h1	10.0	0.33	0.5	0.1	1.0	2000
ME10t1T2h1	10.0	1.32	2.0	0.1	1.0	3000
ME10t1T1h05	10.0	0.66	1.0	0.05	1.0	2000
ME10t1T1h07	10.0	0.66	1.0	0.07	1.0	2000
ME5TtT1h1	5.0	0.66	1.0	0.1	1.0	3000
ME20t1T1h1	20.0	0.66	1.0	0.1	1.0	3000
ME30t1T1h1	30.0	0.66	1.0	0.1	1.0	3000

[a] Planet mass in terms of Earth mass (considering $M_\star = M_\odot$).
[b] Thermal relaxation timescale in orbital units.
[c] Total time simulated in orbital units.

is the area element; $\epsilon = kR_H$ is a softening parameter, which is important to avoid numerical divergence at the planet location, we took it to be a fraction of the Hill radius $R_H = R_p(M_p/(3M_\odot))^{1/3}$, this parameter can also be used to recover 3D effects of vertical stratification (Kley et al., 2012), when k is properly chosen, based on this we used $k = 0.6$; and ξ is a factor that taper the contribution of the torque in the Hill sphere and is given by

$$\xi = 1 - \exp\left[-\frac{|\,\mathbf{r} - \mathbf{R_p}\,|^2}{(0.6R_H)^2}\right]. \tag{3.6}$$

The specific torques (Γ/M_p) are given in units of $v_{K,0}^2$.

3.2 Torque behaviour

The torque exerted by the disk on the planet leads to a change in the planet's angular momentum. The vertical component of the torque changes the planet's orbital angular momentum, therefore leads to the planet orbital migration. In this section, we study the migration behavior of low mass planets in the presence of unstable radial buoyancy. For this purpose, we calculate the cumulative averaged

torque as in Uribe et al. (2011)

$$\Gamma_n = \frac{1}{T_n} \sum_{k=1}^{n} \Gamma_k \Delta t_k, \tag{3.7}$$

where T_n is the total time until timestep n; Γ_k is the vertical component of the averaged torque at time k and is obtained during the simulations by Equation 3.5; and Δt_k is the time interval between timesteps k and $k-1$. The total time simulated for each case can be seen in Table 3.1.

3.2.1 Thermal relaxation

Figure 3.1 shows the cumulative torques for several $\Omega\tau$'s. A bump is observed in the first hundred orbits for all the cases, with the total torque becoming positive for $\Omega\tau \geqslant 2.0$. A second bump, distributed along the following hundreds of orbits, is observed for $\Omega\tau > 0.1$. The first bump achieves higher values for larger $\Omega\tau$'s, indicating that the total torque is directly proportional to the thermal relaxation timescale. Higher cooling times also means higher opacities, thus our results are in agreement with Paardekooper & Mellema (2006).

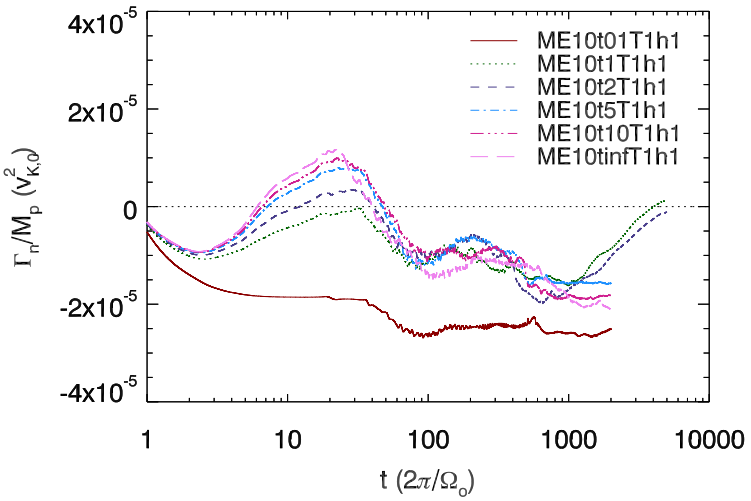

Figure 3.1 Cumulative averaged torques as a function of time. The different lines show the total torques for a $10M_\oplus$ planet, $\beta_T = 1.0$, $h = 0.1$, and several thermal relaxation timescales. See Table 3.1 to check the labels.

Baruteau & Masset (2008a) studied what are the physical mechanisms that can alter the total torque on the planet. They found that the horseshoe drag, for adiabatic disks (infinite opacity), depends on the vortensity and entropy gradients.

The dependence with the vortensity gradient is associated with pressure perturbations and is also present in isothermal disks (Tanaka et al., 2002). The dependence with the entropy gradient is related to the advection of entropy perturbations, which happens just in non-isothermal disks. The entropy-generated torque was also suggested independently by Paardekooper & Papaloizou (2008).

The bumps observed in the total torque curves seem to be related to the development of the vortensity and entropy gradients in the horseshoe region. Figure 3.2 presents the average vortensity and entropy gradients across the horseshoe region as a function of time, for $\Omega\tau = 1.0$, as well as the cumulative sum on time of these gradients until 100 orbits, thus in the region of the first bump. The vortensity-generated horseshoe drag scales with the opposite of the vortensity gradient, the same relation is true for the entropy-generated horseshoe drag (e.g., Baruteau & Lin, 2010). The vortensity gradient in the horseshoe region is negative until ~ 20 orbits, turning to be positive for later times. The vortices tend to be located mostly in the inner side of the planet orbit, explaining the positive vortensity gradients across the horseshoe region. The entropy gradient, on the other hand, is always negative across the horseshoe region, it remains roughly at the initial level until ~ 1000 orbits, having a drastic decrease for later times. The decrease starts exactly after the second bump. The cumulative sum on time of these two gradients, for the first 100 orbits, shows how these gradients influence the total torque. In the first ~ 20 orbits, the sum of the gradients is negative, this is the time interval for which we observe an increase of the total torque. From ~ 20 until 100 orbits, the sum becomes positive and strongly increases, in the other hand, the total torque decreases.

The torque curve for $\Omega\tau = 0.1$ is always below the ones with higher $\Omega\tau$'s. We expect that the isothermal regime will give the lower values for the total torque. Therefore, this behaviour is expected, since this case is the closest to this regime. The final cumulative averaged torque obtained was $-2.5 \times 10^{-5} v_{K,0}^2$. The analytical expression for the total torque in the locally isothermal regime, where temperature is constant with time, but varies with radius, is given by (Paardekooper et al., 2010a)

$$\begin{aligned}\frac{\Gamma_{lociso}}{\Gamma_0} =& -(2.5 - 0.5\beta_T - 0.1\beta_\Sigma)\left(\frac{0.4}{\epsilon/h}\right)^{0.71} \\ & - 1.4\beta_T\left(\frac{0.4}{\epsilon/h}\right)^{1.26} + 1.1\left(\frac{3}{2} - \beta_\Sigma\right)\left(\frac{0.4}{\epsilon/h}\right),\end{aligned} \tag{3.8}$$

with

$$\Gamma_0 = \left(\frac{q}{h}\right)^2 \Sigma_p R_p^4 \Omega_p^2, \tag{3.9}$$

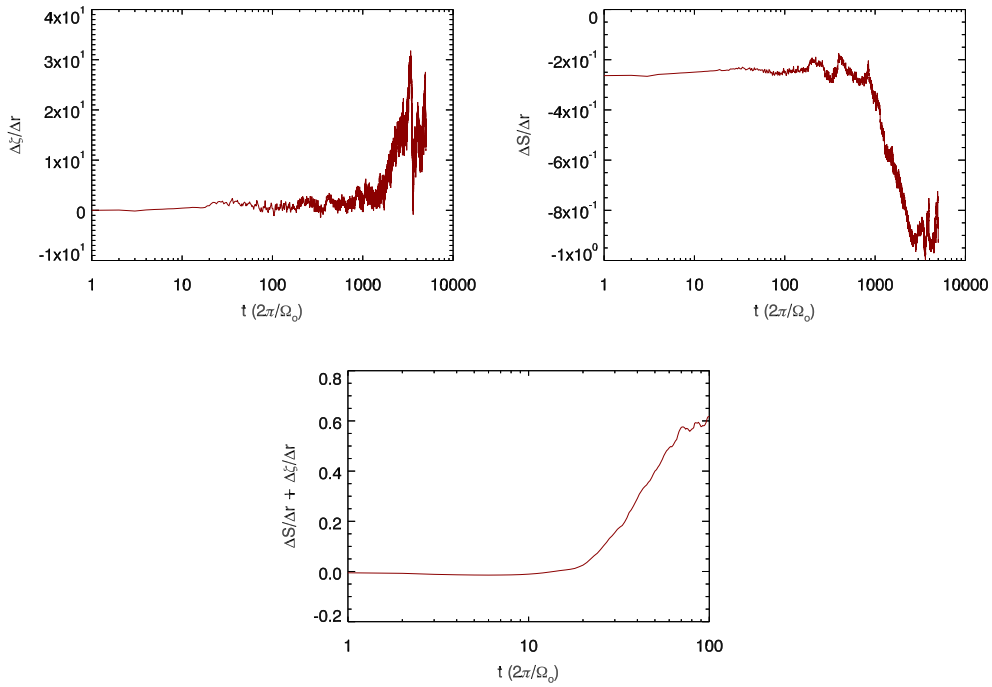

Figure 3.2 The top plot shows the average vortensity gradient across the horseshoe region as a function of time. The middle plot presents the average entropy gradient. The bottom plot shows the cumulative sum of these gradients with respect to time, until 100 orbits. The results were obtained for simulation ME10t1T1h1. The horseshoe radius was obtained by the formula presented in Paardekooper et al. (2010a).

where $q = M_p/M_\star$ is the ratio between the planet and stellar masses; Σ_p is the gas surface density at the planet position; and Ω_p is the planet angular velocity. All the other already defined variables should be updated to their new values in the time the total torque is evaluated. Using Equation 3.8 for $t = 2000$ orbits gives a total torque of $-8.5 \times 10^{-8} v_{K,0}^2$. The analytical value is three orders of magnitude smaller than the one obtained by the simulation.

The cumulative averaged torque obtained by the simulation at $t = 500$ orbits is $-2.4 \times 10^{-5} v_{K,0}^2$, while the analytical value is $-2.6 \times 10^{-6} v_{K,0}^2$. For earlier times there is better agreement between simulations and the analytical expectation; however, there is still a difference of one order of magnitude. We would like to remember that despite $\Omega\tau = 0.1$ is close to a locally isothermal regime, it is still non-isothermal. Moreover, this analytical expression was scaled for a planet softening parameter of $0.4h$, while we used $0.6R_H$. Thus, we do not expect a perfect agreement. The comparison is still interesting to make, to check the torques deviation from locally isothermality.

We observe the formation of two strong vortices in the horseshoe region in the first hundreds of orbits. Vortex formation in the horseshoe region was observed by Koller et al. (2003), and they pointed out that these structures may strongly influence the torque felt by the planet. These vortices grow and induce spiral waves, which make them to migrate to the inner disk. This process cleans up some of the material around the planet orbit, see Figure 3.3. We suspect that the difference between the final numerical torque and the analytical expectation comes mostly from the fact that a partial gap was opened, although the usage of a different softening parameter and the deviations from non-isothermality should also influence, mainly in the early stages, when there is no partial gap.

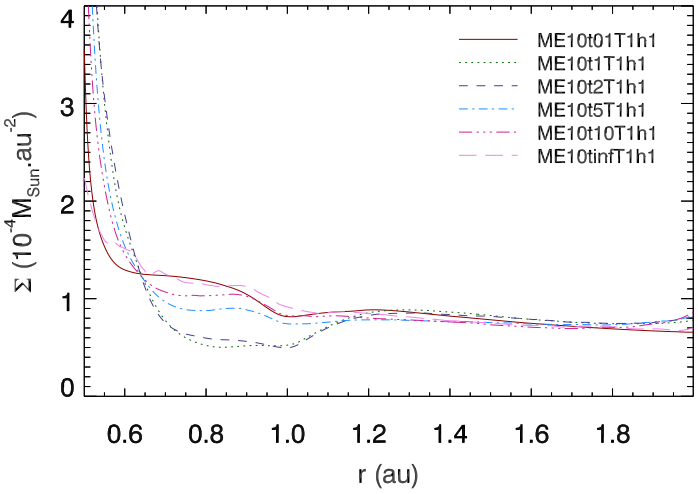

Figure 3.3 Surface density profiles averaged in azimuth at 2000 orbits and for a $10M_\oplus$ planet, $\beta_T = 1.0$, $h = 0.1$, and several $\Omega\tau$'s. See Table 3.1 to check the labels.

For $\Omega\tau = 1.0$ and $\Omega\tau = 2.0$, after the second minimum, the total torques continue to increase from $\sim$ 1000 orbits and $\sim$ 700 orbits, respectively, for the simulation time we could afford. The total torque turns to be positive after ~ 4000 orbits for $\Omega\tau = 1.0$. The total torque convergence is not clear yet. These cases correspond to simulations with the largest change in the surface density close to the planet location, see Figure 3.3.

The planet perturbation induces vortex formation in the horseshoe region, see Figure 3.4. These vortices get amplified with time. The amplification rate is faster for $\Omega\tau = 1.0$, in agreement with Klahr & Hubbard (2014). The vortices excite spiral density waves in the disk, this effect was already observed by Paardekooper et al. (2010b); Surville & Barge (2012, 2013). The exchange of angular momentum between the vortex and the disk leads to fast vortex migration to the inner disk.

Paardekooper et al. (2010b) studied radial vortex migration in 2D isothermal disks, here we confirm that vortex radial migration is also observed in non-isothermal disks. We also observe fast radial migration of our vortices, in timescales of hundreds of orbits. Thus, vortices are formed in the horseshoe region, they get amplified, induce spiral waves in the disk, and then migrate to the inner boundary. Since the planet perturbation is always present, there is constant vortex formation, and the process described above is permanent. As the vortices migrate to the inner disk, they deplete the mass inside the planet orbit, see Figure 3.5.

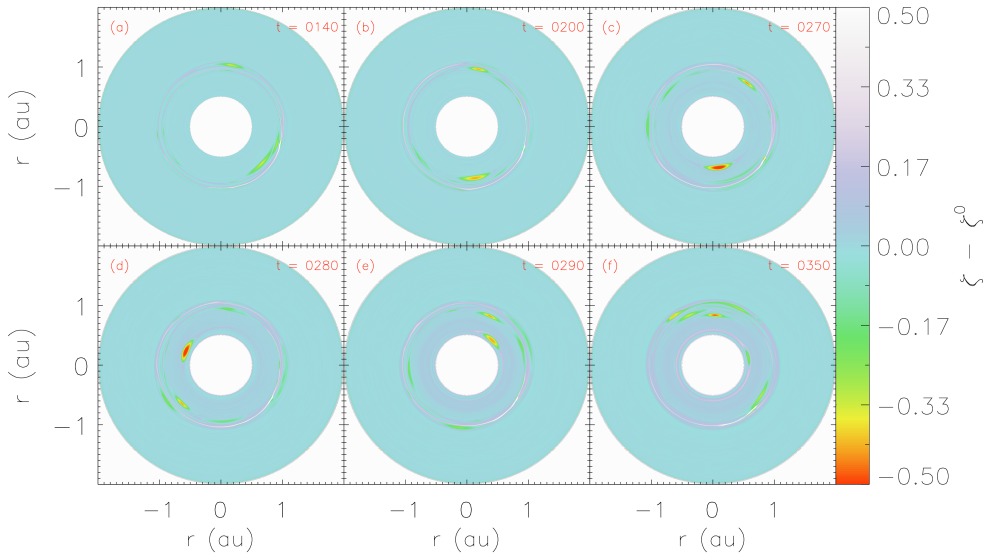

Figure 3.4 Temporal evolution of the potential vorticity with Keplerian profile subtracted for simulation ME10t1T1h1.

The depletion of mass inside the planet orbit produces a partial gap in the surface density profile. The low mass planet is situated in its outer border, see Figure 3.5. This figure shows the evolution of the partial gap opening process. Since a partial gap is opened, the planet migration is no longer a classic type I regime. The planet migration is slowed down and eventually reverses sign. At this stage, the planet is trapped at the outer border of the partial gap.

After the two bumps, the total torques converge to a well defined negative value for $\Omega\tau = 5.0$ and $\Omega\tau = 10.0$, from ~ 700 orbits until the time we stop the simulations. We also observe vortex formation and amplification in the horseshoe region. Nonetheless, they take more time to grow to sufficient amplitudes that lead to the excitation of spiral waves and further vortex migration. The later evolution for these two cases would be most likely very similar to the one described above, if we run the simulations for longer times.

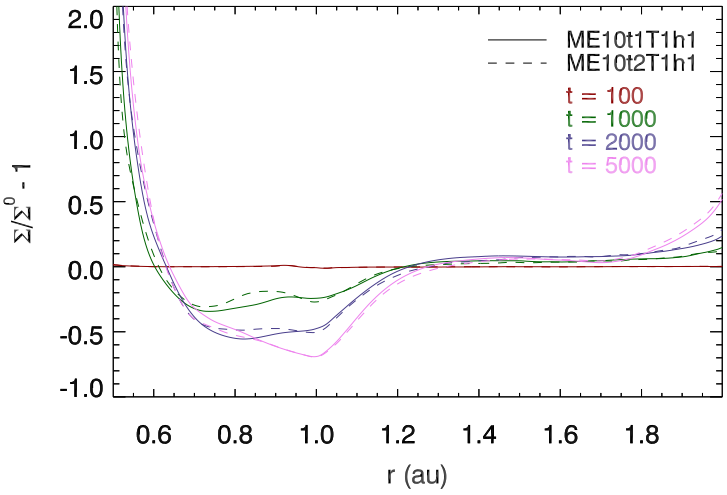

Figure 3.5 Surface density perturbation profiles averaged in azimuth for simulations ME10t1T1h1 and ME10t2T1h1 for different points in time.

The two bumps are also observed in the total torque curve for $\Omega\tau = \infty$ (adiabatic limit). Nonetheless, no strong vortices are formed in the whole simulation interval. Vortex amplification is not efficient in the adiabatic limit, as expected from vortex growth rates, this is in agreement with Klahr & Hubbard (2014). This is also the case for which the surface density changes less with time. Just a very smooth dip is created around the planet position, see Figure 3.3.

3.2.2 Temperature slope

The results for different temperature slopes are shown in Figure 3.6. For $\beta_T = 0.0$ (flat temperature), no vortices are formed. The square of the Brunt-Väisälä frequency (N^2) is positive for this case. There is no unstable radial buoyancy, thus vortex formation is not expected to happen. The planet cleans the material from its orbit, see Figure 3.7, accumulating mass in an inner ring from its orbit. This mass neither flows to the inner boundary nor is spread back to fill up the partial gap. Since the disk is stable, we do not expect that viscosity will be produced, explaining why the mass remains static in an inner ring next to the planet orbit. A very slow decrease is observed for the total torque. We considered a flat temperature, but note that this case does not represent an isothermal regime. The entropy has an initial weak positive slope, since we used $\gamma = 1.43$, thus a stable stratification. We also used a thermal relaxation timescale of $\Omega\tau = 1.0$, therefore the temperature can fluctuate. We chose to keep these parameters equal to what was used for the other β_T's to have a better control for the comparison of the cases. The initial positive

entropy gradient can lead to a negative value for the entropy-related horseshoe drag (Baruteau & Masset, 2008a; Paardekooper & Papaloizou, 2008; Masset & Casoli, 2009), which explains the constant decrease of the total torque.

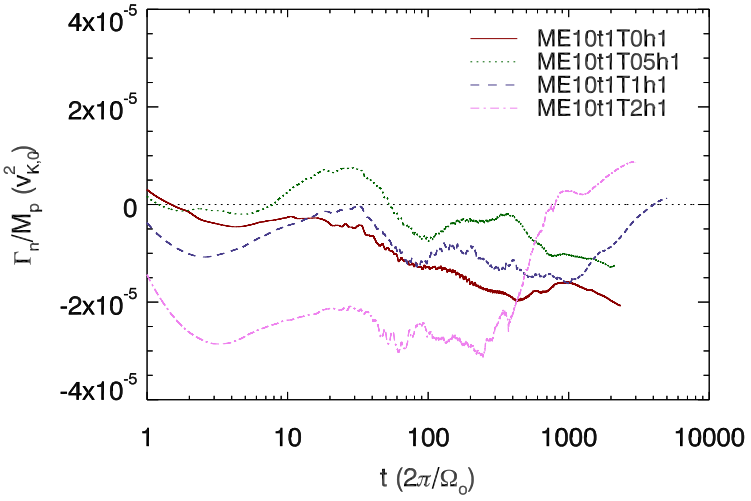

Figure 3.6 Cumulative averaged torques as a function of time. The different lines show the total torques for a $10M_{\oplus}$ planet, $h = 0.1$, $\Omega\tau = 1.0$, and several temperature slopes. See Table 3.1 to check the labels.

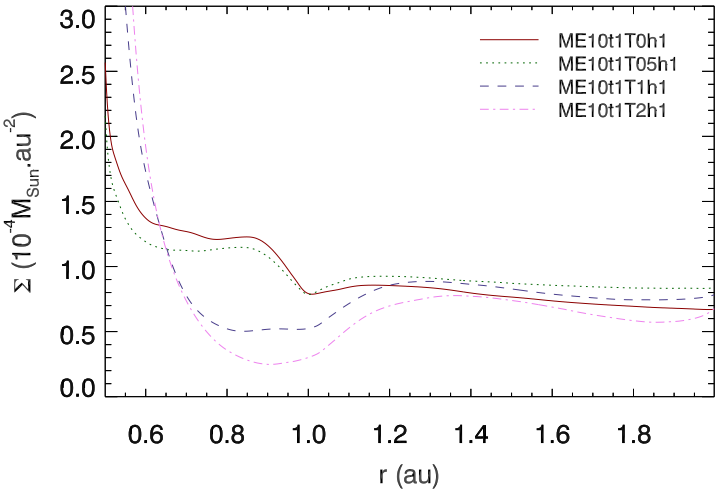

Figure 3.7 Surface density profiles averaged in azimuth at 2000 orbits and for a $10M_{\oplus}$ planet, $\Omega\tau = 1.0$, $h = 0.1$, and several β_T's. See Table 3.1 to check the labels.

The mass is also swept from the planet orbit for $\beta_T = 0.5$, see Figure 3.7. A ring of matter is also formed in an inner radius next to the planet orbit. There is some mass transport due to vortex migration towards the inner disk; however, much less

than for $\beta_T = 1.0$. We did not observe the formation of strong vortices for this case. Vortex amplification is favored for steeper temperature slopes. The amplification rate of the perturbations is proportional to β_T^2 (Raettig et al., 2013). The horseshoe drag is able to counteract the Lindblad torque during the first bump, even reversing the migration direction. Nonetheless, as time evolves, a constant decrease of the total torque is observed, since there is not enough viscosity being produced and the horseshoe drag is getting saturated with time. In the next section, we discuss how much viscosity is being produced.

Vortex amplification is strongly favored for $\beta_T = 2.0$, due to the steep temperature gradient. Indeed, many more vortices are observed for this case. A gap is carved out much faster in this case. For $t \gtrsim 250$ orbits, the total torque starts to constantly increase, due to the mass depletion caused by the vortex migration, likewise as for $\beta_T = 1.0$. The partial gap is also deeper than for $\beta_T = 1.0$, see Figure 3.7. Nonetheless, this case is not realistic. As much shallower temperature slopes are predicted by observations (e.g., Natta, 1993).

The temperature slopes that favor the formation and amplification of vortices due to unstable radial buoyancy are not the same that support higher total torques. The initial total torque is inversely proportional to the temperature slope, see Figure 3.6, thus shallower temperature slopes can lead to higher total torques, whereas the opposite is true for the amplification of vortices, where steeper temperature slopes favors vortex amplification.

3.2.3 Disk aspect ratio

Figure 3.8 shows the results for different disk aspect ratios. The first thing to notice is that the initial bump is much stronger for colder disks. This result is in agreement with Yamada & Inaba (2011). They showed that the horseshoe drag is dependent on the radiative efficiency, having increasing values for inefficient radiative cooling. The disk aspect ratio can be seen as an indicator of the radiative efficiency. Therefore, smaller h's lead to higher total torques. On the other hand, the amplification of vortices is dependent on N^2 (Raettig et al., 2013), thus it is also dependent on h^2, meaning that vortex amplification is favored for hotter disks. For $h = 0.05$ no vortex formation was observed. For $h = 0.07$, we observed a weak vortex in the horseshoe region.

The planets carved out a gap for $h = 0.05$ and $h = 0.07$, see Figure 3.9. Crida et al. (2006) showed that smaller values of h produce deeper gaps, in accordance with our results. However, we would expect that a higher threshold for the planet mass is required. A viscosity of the order of q and h of the order of $q^{1/3}$ are needed

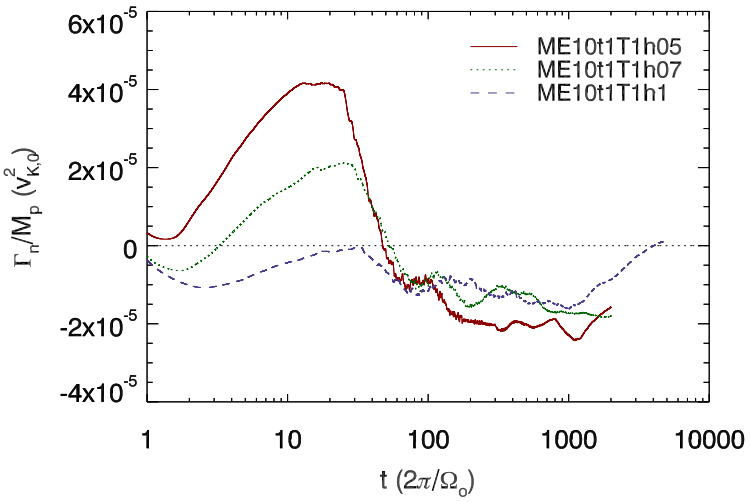

Figure 3.8 Cumulative averaged torques as a function of time. The different lines show the total torques for a $10M_{\oplus}$ planet, $\beta_T = 1.0$, $\Omega\tau = 1.0$, and several disk aspect ratios. See Table 3.1 to check the labels.

to allow gap opening. The disk scale height at the planet position changes over time in our simulations and the viscosity is also generated due to the hydrodynamical instability. Therefore, it is rather complex to check whether the gap opening criterion is being fulfilled in our simulations, due to the constant changing of the involved disk parameters.

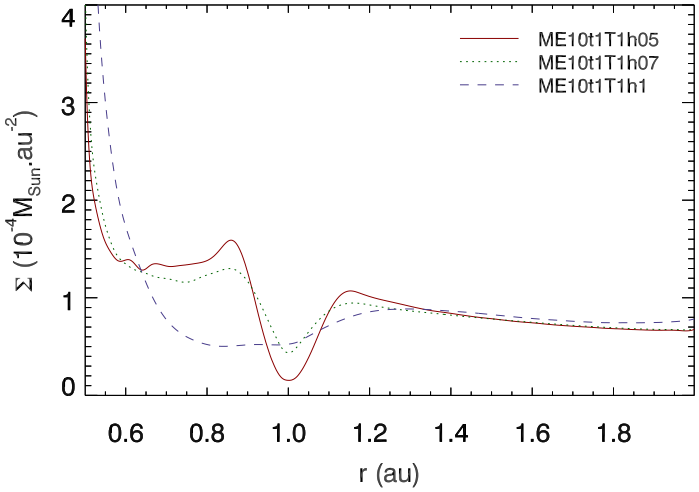

Figure 3.9 Surface density profiles averaged in azimuth at 2000 orbits and for a $10M_{\oplus}$ planet, $\beta_T = 1.0$, $\Omega\tau = 1.0$, and several disk aspect ratios. See Table 3.1 to check the labels.

For later times, the total torque decreases for smaller h's. The growth of the perturbations scales with h^2, which may explain why for later times the total torque is decreasing for smaller h's. For $h = 0.05$ and $t \gtrsim 1000$ orbits, the total torque starts to increase again. We expect that this increase is due to the planetary gap rather than the balance between Lindblad torque and horseshoe drag. Thus, for $h = 0.07$, at some point the torque would also not be well described by a classic type I regime.

3.2.4 Planet mass

The dependence of radiative effects on the planet mass was studied by Kley & Crida (2008) in radiative 2D disks. They found that planets with masses below $\sim 50 M_\oplus$ migrate outwards with velocities comparable to the absolute value of the standard type I migration. More massive planets were found to migrate inwards and to roughly follow the isothermal type II migration behaviour. In this scenario the planet cores would migrate outwards until it grows to $\sim 50 M_\oplus$, afterwards its migration would reverse sign and follow the type II migration case. Kley et al. (2009) extended their previous studies for 3D radiative viscous disks. Considering the same opacity law, the effect of the migration reversal appeared to be even stronger in 3D disks, but the upper limit for outward migration was reduced to $\sim 33 M_\oplus$. Lega et al. (2015) studied the migration of low mass planets in stellar irradiated disks and considering viscous friction as a source of heating. They compared their numerical results with the analytical formula of Paardekooper et al. (2011) and found agreement for planets with masses greater than $20 M_\oplus$. In addition, outward migration was observed for planets with masses up to $60 M_\oplus$.

The lowest mass from which type I migration can be directed outwards was studied by Lega et al. (2014) in 3D radiative disks. They concluded that the transition to inward migration occurs for planets with masses in the range from $3 - 5 M_\oplus$. The physical explanation is that an overdensity of gas is created behind the planet position for lower mass planets, which generates a negative contribution for the torque. Benítez-Llambay et al. (2015) used 3D radiative-HD simulations to study the migration of a $3 M_\oplus$ planet initially positioned at the Jupiter's distance from the Sun. They bombarded this planetary embryo with solid material and considered that the gravitational energy of the infalling material was completely converted into heat and then radiated by the planet. This process produces a force, which they called heating torque. They found that this heating torque has always a positive sign, which counteracts the rapid inward migration. In this scenario, planets with masses smaller than $3 M_\oplus$ could also experience outward migration.

Based in the discussion above, we decide to consider planets with masses in the range $5 - 30M_{\oplus}$ in our studies, since such planets should be able to experience outward migration. Figure 3.10 shows the torque results for several planet masses. The initial bump is narrower for higher planet masses. This confirms that the horseshoe drag gets saturated faster for larger planet masses. Moreover, the gap opening process may remove the saturated horseshoe drag and the total torque stops to be described by a classic type I regime.

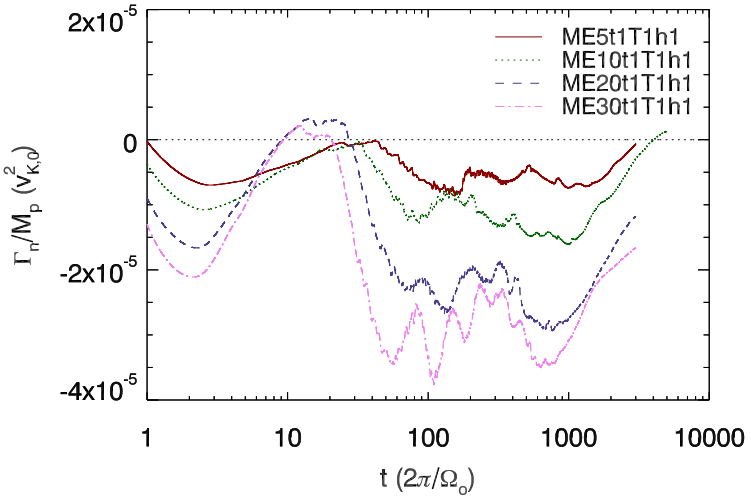

Figure 3.10 Cumulative averaged torques as a function of time. The different lines show the total torques for $\beta_T = 1.0$, $h = 0.1$, $\Omega\tau = 1.0$, and several planet masses. See Table 3.1 to check the labels.

Vortices are formed in the horseshoe region, get amplified, and then migrate to the inner disk for all the cases. Figure 3.11 shows the surface density profiles for all the planet masses after 3000 orbits. For the smaller planet masses ($M_p \leqslant 10M_{\oplus}$), a partial gap is carved out due to inward vortex migration, and the planet sits in its outer border. For the higher planet masses ($M_p \geqslant 20M_{\oplus}$), the migration of vortices also opens up a partial gap, but as time evolves, a gap centered at the planet position is settled. Higher mass planets are more likely to carve out a gap, under the same disk conditions. The generation of viscosity and the changing of the disk scale height at the planet position seem to allow for gap opening for our higher mass planets ($20M_{\oplus}$ and $30M_{\oplus}$).

At later times, the total torques cannot be described by a classic type I migration regime, due to the gap opening. For all the cases the total torques start to constantly increase for $t \gtrsim 1000$ orbits. It is also observed that the total torques get smaller values for higher planet masses. One reason for these smaller values could be

simply that the Lindblad torques are larger for larger planet masses (Tanaka et al., 2002), therefore much higher positive horseshoe drags are required to overcome the Lindblad torque.

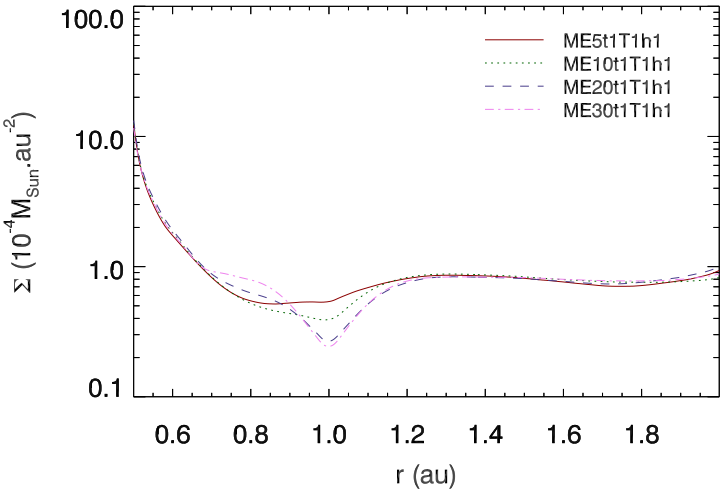

Figure 3.11 Surface density profiles averaged in azimuth at 3000 orbits and for $\beta_T = 1.0$, $\Omega\tau = 1.0$, $h = 0.1$, and several planet masses. See Table 3.1 to check the labels.

3.3 Generation of turbulence

In this section we study the generation of turbulence due to unstable radial buoyancy. For that, we analyse the temporal evolution of the α parameter. Using the $r - \phi$ component of the Reynolds stress and the local sound speed, we calculate α as in Flock et al. (2011)

$$\alpha = \frac{\int \Sigma \left(\frac{v'_\phi v'_r}{c_s^2} \right) dA}{\int \Sigma dA}, \tag{3.10}$$

where $v'_\phi = v_\phi - \overline{v_\phi}$ is the turbulent azimuthal velocity, with $\overline{v_\phi}$ being the average azimuthal velocity; and $v'_r = v_r - \overline{v_r}$ is the turbulent radial velocity, with $\overline{v_r}$ being the average radial velocity. This gives a global average for the α-viscosity. The turbulence-triggered viscosity can then be estimated by (Shakura & Sunyaev, 1973)

$$\nu = \alpha c_s H, \tag{3.11}$$

where H is the disk scale height.

Radiative and viscous diffusion are crucial to keep the horseshoe drag unsaturated and maintain an outward, slow inward, or stalled migration (Masset, 2001; Ogilvie & Lubow, 2003; Paardekooper & Papaloizou, 2008; Kley & Crida, 2008; Paardekooper & Papaloizou, 2009). When radiative and/or viscous diffusion are not present, after a few libration timescales, the entropy gradient flattens and the entropy-generated torque in the horseshoe region becomes saturated (Baruteau & Masset, 2008a; Paardekooper & Papaloizou, 2009). This is also true for the vortensity-generated torque, since when diffusion is not present the streamlines in the horseshoe region closes and become symmetric with respect to the planet's location, producing a zero net torque (Kley et al., 2009). Here, we analyse how much viscosity is being produced due to unstable radial buoyancy.

3.3.1 Thermal relaxation

Figure 3.12 shows the evolution of α for different $\Omega\tau$'s. The cases are sorted in three different panels with respect to their evolution behaviour. In the top panel, we see the α evolution for $\Omega\tau = 0.1$ and $\Omega\tau = \infty$. The α-value is maintained roughly equals to 10^{-5} until ~ 300 orbits for the former. Afterwards, the potential vorticity increases close to the horseshoe region and consequently turbulence is generated. The double peak between ~ 300 orbits and ~ 1000 orbits can be associated with the presence of vortices. Once the second vortex hits the inner boundary, the α-value decreases. After ~ 1000 orbits, when a lot of mass was already swept from the planet orbit, we can see that α does not converge to a clear value; however, a further tendency to its increase is observed. For $\Omega\tau = \infty$, we observe a constant increase of α until ~ 1000 orbits. This case did not present any strong vortex along the whole time simulated. Substantial potential vorticity is observed close to the horseshoe region until ~ 1000 orbits, which explains the constant increase of α. Nonetheless, the amplification of perturbations is not efficient for the adiabatic limit (Klahr & Hubbard, 2014), explaining the smoothing of the potential vorticity after 1000 orbits, the lack of vortices, and the further decay of α.

The middle panel shows the α evolution for $\Omega\tau = 1.0$ and $\Omega\tau = 2.0$. A constant increase of α is observed until ~ 300 orbits and ~ 500 orbits for $\Omega\tau = 1.0$ and $\Omega\tau = 2.0$, respectively. The peak at ~ 300 orbits, for $\Omega\tau = 1.0$, can be associated to the first strong vortex that migrates to the inner disk. Likewise, the peak at ~ 500 orbits, for $\Omega\tau = 2.0$, can be associated to its first strong vortex. The first vortices are the ones that achieve the highest amplitudes, therefore they produce more viscosity. Once the first vortex migrate to the inner disk, the α-value starts to decrease, since the next vortices produce less viscosity. The chaotic behaviour

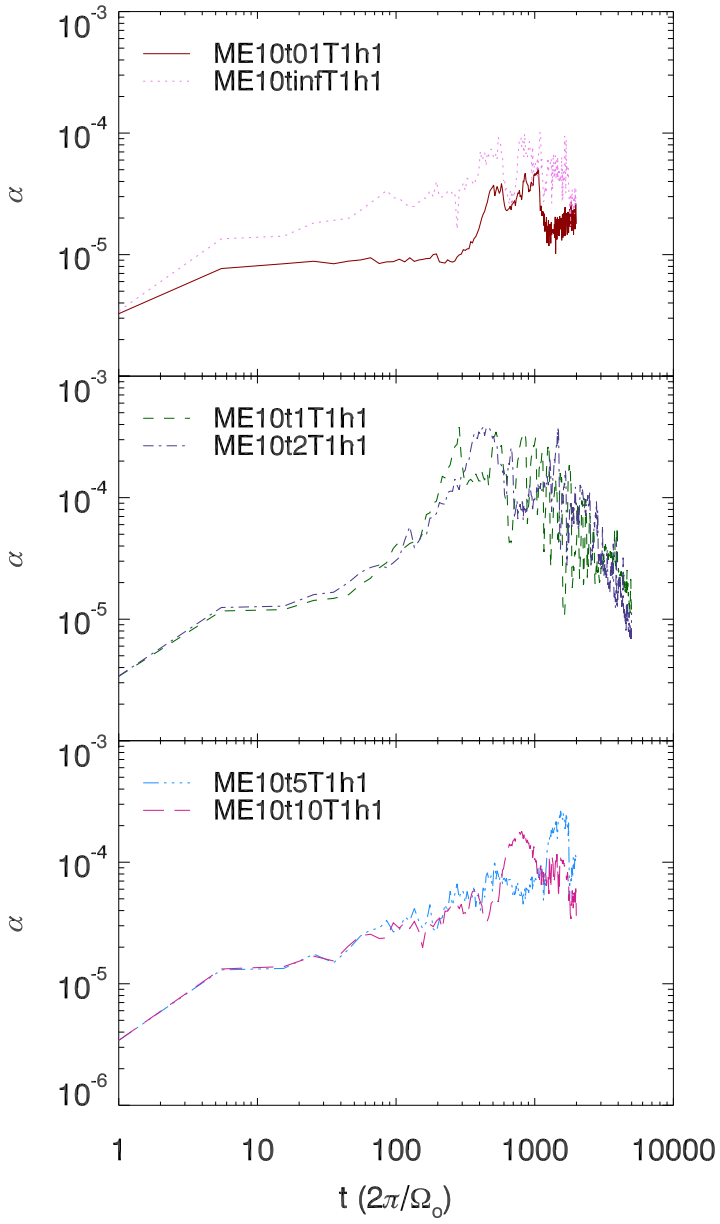

Figure 3.12 α parameter as a function of time. The different lines show α for a $10M_{\oplus}$ planet, $\beta_T = 1.0$, $h = 0.1$, and several thermal relaxation timescales. See Table 3.1 to check the labels. The data was binned, using a bin size of $\Delta t = 10.0$.

of α, when its curve starts to decrease, is related to the appearance of the next vortices. Thus, each peak is related to the appearance of a new vortex.

The bottom panel shows the α evolution for $\Omega\tau = 5.0$ and $\Omega\tau = 10.0$. For both cases, α is constantly increasing until the time the simulations are stopped. A pronounced peak is observed at ~ 1050 orbits and ~ 800 orbits for $\Omega\tau = 5.0$

and $\Omega\tau = 10.0$, respectively. Once more, the peaks can be associated with the appearance of the first strong vortex. We do not observe a decay of the α-value for these cases, because vortex amplification is slower and the next vortices yet could not grow and migrate to the inner disk.

3.3.2 Temperature slope

The evolution of α for different temperature slopes can be seen in Figure 3.13. The top panel shows the results for $\beta_T = 0.0$ and $\beta_T = 0.5$. For both cases, the α-value increases until $\alpha \sim 1.5 \times 10^{-5}$, remaining roughly at this level until the end of the simulations. Despite N^2 being positive for $\beta_T = 0.0$, some potential vorticity is observed in the density enhancement at the inner side of the planet orbital position, indicating that the local variations of the azimuthal velocity at this enhancement may be enough to produce some local turbulence. After ~ 700 orbits, for $\beta_T = 0.0$, some sharp variations arise; however, we could not relate them to any particular feature seem in the surface density or potential vorticity maps. For $\beta_T = 0.5$, a peak featuring at ~ 300 orbits is observed, which can be associated to some tiny vortices near the horseshoe region. Nonetheless, at ~ 600 orbits, these structures are already gone and α remains around 1.5×10^{-5} until the end of the simulation. As previously touched upon, vortex amplification scales with β_T^2 (Raettig et al., 2013), therefore for shallow temperature slopes we do not expect to see strong vortices or much turbulence being produced.

The bottom panel shows the α evolution for $\beta_T = 2.0$, alongside with $\beta_T = 1.0$, to provide some comparison. The evolution for both cases are very similar, with the difference that α achieves higher values for $\beta_T = 2.0$ than for $\beta_T = 1.0$. This behaviour is expected, since for $\beta_T = 2.0$ more vortices are created, meaning that more turbulence is generated. Also, the peak featuring at ~ 150 orbits cannot be related to an unique strong vortex, but to several strong vortices that migrate to the inner disk. From this time onwards the α-value decreases, likewise the $\beta_T = 1.0$ case.

3.3.3 Disk aspect ratio

Figure 3.14 shows the evolution of α for several disk aspect ratios. The initial α-value, after 1 orbit, is highly dependent on h. This is expected, since α is dependent on the inverse of c_s^2, thus it also scales with h^{-2}. For $h = 0.05$, α remains roughly above 10^{-4} until ~ 500 orbits. This is the time when the partial gap gets more pronounced, therefore after partial gap opening, the α-value decreases. For $h = 0.07$, α constantly increases until ~ 400 orbits. A peak is observed at this

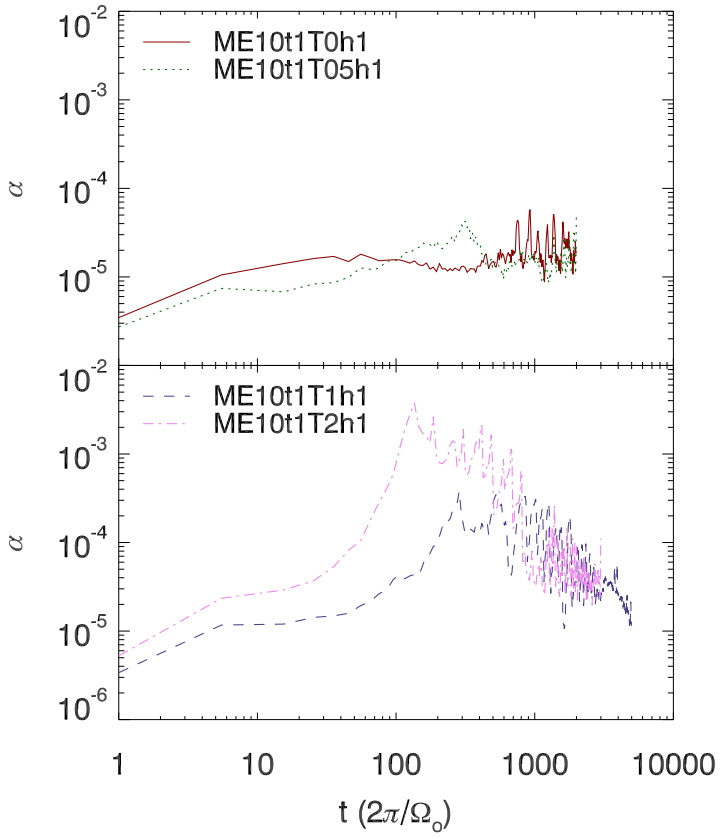

Figure 3.13 α parameter as a function of time. The different lines show α for a $10M_{\oplus}$ planet, $h = 0.1$, $\Omega\tau = 1.0$, and several temperature slopes. See Table 3.1 to check the labels. The data was binned, using a bin size of $\Delta t = 10.0$.

time, with a duration of about 600 orbits. Once more, the peak is associated with a vortex that arises in the horseshoe region; however, permanent vortex formation is not observed. After this peak, a substantial amount of mass was already swept from the planet orbit, thus the α-value decreases, as it was observed for $h = 0.05$.

3.3.4 Planet mass

Figure 3.15 shows the α evolution for different planet masses. The initial α-value is larger for larger planet masses; however, the further evolution is quite similar for all the cases. The time at which the first strong vortex has its amplitude peak also depends on the planet mass. With the peak happening faster for higher planet masses. Nonetheless, the maximum amplitudes that α can achieve do not seem to be strongly dependent on the planet mass. For all the cases, α do not get much higher than $\sim 5 \times 10^{-4}$.

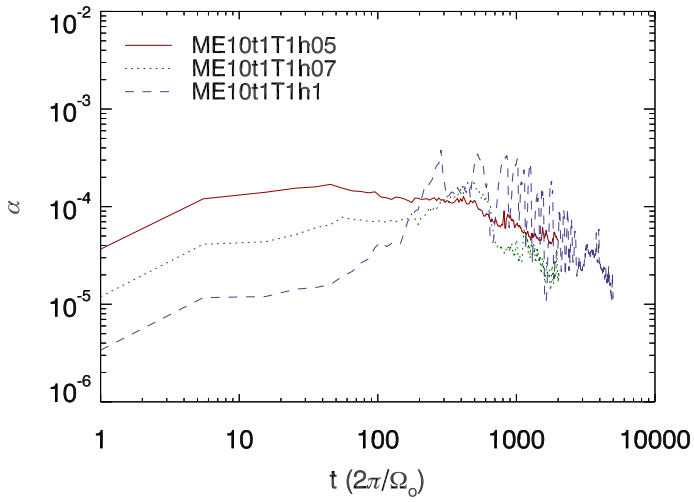

Figure 3.14 α parameter as a function of time. The different lines show α for a $10M_{\oplus}$ planet, $\beta_T = 1.0$, $\Omega\tau = 1.0$, and several disk aspect ratios. See Table 3.1 to check the labels. The data was binned, using a bin size of $\Delta t = 10.0$.

3.4 Summary and conclusions

In this chapter, we studied the long-term evolution of the migration of low mass planets in non-isothermal turbulent disks. Such planets experience the so-called type I migration. This migration regime is governed by the Lindblad torque – exchange of angular momentum between the planet and material located at the Lindblad resonances – and the horseshoe drag – exchange of angular momentum between the planet and material at the horseshoe region. The study of type I migration in isothermal disks leads to fast migration timescales (Tanaka et al., 2002), such rapid migration rates cannot explain the observed mass-distance distribution of exoplanets (Alibert et al., 2004; Ida & Lin, 2008; Mordasini et al., 2009). The consideration of non-isothermal disks helped to ease the type I migration problem (e.g., Morohoshi & Tanaka, 2003; Paardekooper & Mellema, 2006). Nonetheless, we still need to understand how to prevent the saturation of the horseshoe drag, which is essential to keep slow or outward migration (Baruteau & Lin, 2010). Here, we analysed whether unstable radial buoyancy can produce enough turbulence-triggered viscosity to maintain the unsaturation of the horseshoe drag. We run 2D-HD global simulations of planet-disk interactions with the PLUTO code. Thermal relaxation was used to account for radiative diffusion and we considered buoyantly radially unstable disks, which can lead to the formation and amplification of vortices.

We analysed the dependence of the total torques with the thermal relaxation timescales, the temperature slopes, the disk aspect ratios, and the planet masses.

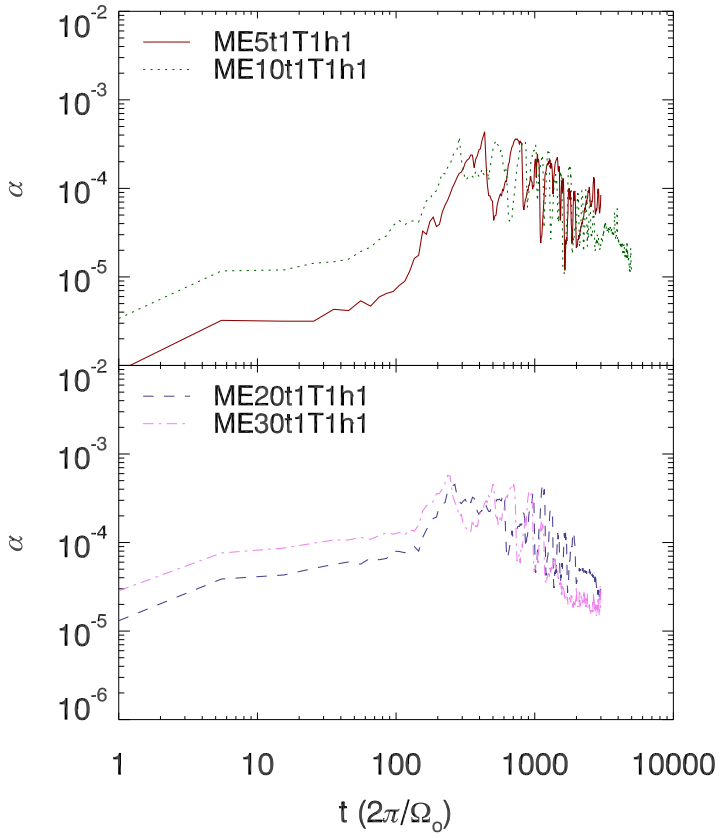

Figure 3.15 α parameter as a function of time. The different lines show α for $\beta_T = 1.0$, $h = 0.1$, $\Omega\tau = 1.0$, and several planet masses. See Table 3.1 to check the labels. The data was binned, using a bin size of $\Delta t = 10.0$.

We found that longer cooling timescales lead to more positive torques (outward migration). In the other hand, the amplification of vortices is faster for $\Omega\tau = 1.0$ and very inefficient in the adiabatic limit. The same inverse dependence was observed for the temperature slopes and disk aspect ratios. Shallower temperature slopes favor more positive torques, whereas steeper lead to faster vortex growth. With respect to the disk temperature, smaller disk aspect ratios lead to more positive torques, whereas larger favors vortex amplification. Finally, we did not observe a strong dependence of the vortex growth time with the planet masses; however, we found that smaller planets experience larger torques. Moreover, planets with masses greater than $\sim 20 M_\oplus$ are able to carve out a gap, therefore at very early stages the torques experienced by the planet cannot be described by a classic type I regime. In summary, the disk parameters that favors vortex growth are opposite to the ones that favors larger total torques. Therefore, unstable radial buoyancy is not a good mechanism to prevent the saturation of the horseshoe drag.

Despite radial buoyancy not being able to support large horseshoe drags, we found that it can produce a planet trap, for the disk parameters for which vortex amplification is favored. Vortices are formed in the horseshoe region due to the planet perturbation. These structures can then grow to amplitudes that are large enough to induce spiral waves in the surrounding disk, and the vortices then migrate to the inner disk. Since the planet perturbation is constant, vortex formation persists in the horseshoe region, which is followed by vortex growth and migration to the inner disk. This process depletes the mass in the inner side of the planet orbit, creating a planet trap. The low mass planet remains in the outer edge of this underdensity. Therefore, unstable radial buoyancy may not be able to prevent the unsaturation of the horseshoe drag; however, it can produce a planet trap and prevent the low mass planets to have a fast migration to the inner disk.

We suggest that these kind of simulations should be carried in three dimensions, to check whether the trap would still be created. The biggest concern is with respect to the vortex migration in a 3D disk. Richard et al. (2013) have shown that 3D vortex migration presents similar timescales as the 2D case (Paardekooper et al., 2010b; Surville & Barge, 2012, 2013). Nevertheless, their studies were performed for a rather small number of orbits, longterm simulations are needed to confirm that the vortices survive and migrate to the inner disk. The planet accretion is also an effect that should be considered. Planets with masses larger than $\sim 10 M_{\oplus}$ are supposed to accrete gas, this effect can potentially affect the planet migration. Simulations with multiple planets would also be interesting, in particular to compare with the *Kepler* systems with multiple low mass planets packed very close to the parent star (e.g., Lissauer et al., 2011).

Chapter 4

Gap opening planets in stellar irradiated disks

The work presented in this chapter is from **Lobo Gomes, A.**, *Klahr, H., Kuiper, R., Uribe, A. L., in preparation.*

Planetary gaps are carved out by high mass planets, when the gravitational torque coming from the planet spiral density waves can overtake the disk viscous torque (Lin & Papaloizou, 1979; Goldreich & Tremaine, 1980). The inner disk pushes the material inwards and the outer disk outwards, sweeping up material from the planet orbit. Varnière et al. (2004) proposed that gap width edges could be estimated by imposing a balance between the viscous and gravitational torques. Nevertheless, numerical simulations happened to present much narrower gaps than the ones expected from this assumption. Crida et al. (2006) suggested that an additional torque, which they called a pressure torque, helped the viscous torque to hold up the gravitational one, explaining the narrower gaps. This pressure torque transports part of the gravitational torque through density waves. They introduced a gap opening criterion that takes into account the planet-to-stellar mass ratio (q), the disk aspect ratio (h), and the α-viscosity parameter (Shakura & Sunyaev, 1973).

Despite Crida et al. (2006)'s model being able to explain the shapes and widths of planetary gaps up to a well extent, it predicts far too deep gaps. Recently, there has been some attempts to model the gap depth, and a power-law relation with q, h, and α was found (Duffell & MacFadyen, 2013; Fung et al., 2014; Kanagawa et al., 2015). The physical argument behind this scaling is that the torque exerted by the planet on the disk depends on the local surface density, when the torque is dominated by resonances excited inside the gap (Fung et al., 2014). A proper

determination of the gap surface density is important, because the remainder material inside the gap may be capable of exerting a horseshoe drag like torque on the planet (Paardekooper & Papaloizou, 2009), which influences the dynamical evolution of the planet's orbital parameters, therefore the migration description, as well as the evolution of the planet eccentricity.

A second problem related to the conventional gap opening criterion is that low mass planets embedded in disks with low viscosities should not be able to carve out gaps. Nevertheless, numerical simulations and semi-analytical studies have shown the contrary (e.g., Goodman & Rafikov, 2001; Dong et al., 2011b,a; Duffell & MacFadyen, 2012). In Chapter 3, some of our low mass planets were also able to open gaps, possibly violating the Crida et al. (2006)'s criterion. Duffell (2015) presented a new analytical model for gap profiles, which predicts that low mass planets can also open gaps in low viscosity disks. Moreover, his model can recover the shape of planetary gaps up to a well extent, including the gap width and depth. This model assumes similar arguments as Varnière et al. (2004), however, it uses a simpler algebra.

Many of the numerical studies related to gap structure have considered locally isothermal disks. Gap opening planets in radiative disks were studied by Klahr & Kley (2006). Their focus was with respect to the numerical parameters and the planet accretion process. Nevertheless, the heating from stellar irradiation was neglected. In this chapter, we investigate the interaction of gap opening planets with their parent disks, considering radiative disks, where the stellar irradiation is also included.

From an observational point of view, the study of planetary gaps are important to properly interpret recent observations of disks where cavities have been detected. Usually these holes are much wider than what we expect for planetary gaps, from the theory of planet-disk interactions. So far, the only two observed systems that display a planetary gap like feature are HD 169142 (Quanz et al., 2013) and TW Hya (Debes et al., 2013; Akiyama et al., 2015). These two systems were observed with scattered light in the near infrared. Such kind of data are very powerful to detect disk structures (gaps, spiral waves, arcs, rims). Further observations with the *Atacama Large Millimeter/submillimeter Array* (ALMA) observatory should be able to measure planetary gap surface densities. Therefore, put to the test the current theory.

In this chapter we are interested in studying gap opening planets in stellar irradiated disks. The main goal is to compare the results with radiation transport to their locally isothermal and adiabatic counterparts. The chapter is organized as follows. In Section 4.1 we describe our planet-disk model and simulations setup.

The general results for distinct models are presented in Section 4.2, where we discuss the most important differences for various treatments for the disk thermal structure. The planet migration and the planetary gap structure are discussed in Section 4.3. Finally, in Section 4.4 we briefly summarize our results and main conclusions.

4.1 Simulations

We study gap opening planets in protoplanetary disks (PPDs) by solving numerically the following system of radiative-hydrodynamical (RT-HD) equations in three-dimensions (3D)

$$\frac{\partial \rho}{\partial t} + \boldsymbol{\nabla} \cdot (\rho \mathbf{v}) = 0, \tag{4.1}$$

$$\frac{\partial \mathbf{v}}{\partial t} + (\mathbf{v} \cdot \boldsymbol{\nabla})\mathbf{v} = -\frac{1}{\rho}\boldsymbol{\nabla} p - \mathbf{a}, \tag{4.2}$$

$$\frac{\partial E}{\partial t} + \boldsymbol{\nabla} \cdot ((E + p)\mathbf{v}) = \rho \mathbf{v} \cdot \mathbf{a} - \boldsymbol{\nabla} \cdot (\mathbf{F_R} + \mathbf{F}_\star), \tag{4.3}$$

$$\mathbf{F}_\star(r, \nu) = \mathbf{F}_\star(R_\star, \nu)\left(\frac{R_\star}{r}\right)^2 e^{-\tau(r,\nu)}, \tag{4.4}$$

$$\frac{\partial E_R}{\partial t} = -f_c(\boldsymbol{\nabla} \cdot \mathbf{F_R} + \boldsymbol{\nabla} \cdot \mathbf{F}_\star), \tag{4.5}$$

where ρ is the gas density, $\mathbf{v}$ is the gas velocity vector, p is the gas pressure, $\mathbf{a}$ is an acceleration term that accounts for additional physics, E is the total gas energy density, $\mathbf{F_R}$ is the flux of the dust radiation energy density, $\mathbf{F}_\star$ is the flux of the stellar irradiation energy density, ν is the radiation frequency, $R_\star$ is the stellar radius, $\tau(r, \nu)$ is the optical depth dependent on frequency, E_R is the dust radiation energy density, and f_c is a coefficient that depends on the ratio between internal and radiation energies. The first three equations are the Euler equations for compressible fluids, whereas the last two equations describe the radiation transport.

We need an equation of state to close this system of equations. We chose an ideal equation of state

$$p = (\gamma - 1)\rho\left(E - \frac{1}{2}\rho v^2\right), \tag{4.6}$$

where $\gamma = 1.4$ is the adiabatic index. The acceleration term is composed of the gravitational potential of the star and the planet plus contributions from stellar feedback and dust radiation

$$\mathbf{a} = \boldsymbol{\nabla}(\phi_\star + \phi_p) - \frac{\boldsymbol{\nabla} \cdot \mathbf{F}_\star \hat{\mathbf{e}}_\mathbf{r}}{c\rho} - \frac{\lambda}{\rho}\boldsymbol{\nabla} E_R, \tag{4.7}$$

where $\phi_\star$ is the stellar gravitational potential, ϕ_p is the planet gravitational potential, c is the speed of light, and λ is the flux limiter. The coefficient f_c is given by

$$f_c = \left(\frac{c_V \rho}{4aT^3} + 1\right)^{-1}, \tag{4.8}$$

where c_V is the specific heat capacity, a is the radiation constant, and T is the temperature. We assume thermal equilibrium, thus $T_{rad} = T_{dust} = T_{gas} = T$, where T_{rad} is the radiation temperature, T_{dust} is the dust temperature, and T_{gas} is the gas temperature. The flux of the radiation density energy is given by

$$\mathbf{F_R} = -\frac{\lambda c}{\kappa_R \rho} \boldsymbol{\nabla} E_R, \tag{4.9}$$

where κ_R is the Rosseland mean opacity. Finally, we can relate the dust radiation energy density with the disk temperature, since we assumed equilibrium between the dust temperature and the total radiation field ($T_{dust} = T_{rad}$), where the total radiation field is the superposition of the stellar and the thermal dust radiation fields, then

$$aT^4 = E_R + \sum_{\nu_i} \frac{\kappa(\nu_i)}{\kappa_P(T)} \frac{\mid \mathbf{F}_\star(r, \nu_i) \mid}{c}, \tag{4.10}$$

where $\kappa(\nu_i)$ is the dust opacity for a given frequency ν_i and $\kappa_P(T)$ is the Planck mean dust opacity for a given temperature T.

We used the finite volume Godunov-type code PLUTO (Mignone et al., 2007). In order to carry out RT-HD simulations of planet-disk interactions, we merged the planet-disk module from Uribe et al. (2011) with the radiation transport module from Kuiper et al. (2010). The planet-disk module implemented the gravitational potentials from the star and the planet, using a softening approach for the planet gravitational potential. We used a softening parameter of $\epsilon = 0.5 R_H$, where R_H is the planet Hill radius. The planet is set up as a point mass and it is allowed to move. We added the planet slowly along its first orbit, that means the planet mass increased from 0 to M_p smoothly. The planet acceleration changes according to its gravitational interaction with the star-disk system, and its velocity and position are updated using a leapfrog integrator. Since we do not properly resolve the planet Hill sphere, we taper the contribution of the disk gravity in this region, in the calculation of the planet acceleration and of the torque applied by the disk on the planet. More information about this procedure can be found in Uribe et al. (2011).

The radiation transport module solves the radiation transport in four steps. Firstly, the flux of the stellar energy density (Equation 4.4) is calculated using a ray-tracing method. Secondly, the dust radiation energy density is calculated

from Equation 4.10, using the current temperature distribution. Thirdly, the new dust radiation energy density is evolved using Equation 4.5, where a flux limited diffusion (FLD) approximation was used to solve Equation 4.9. Finally, the new temperature distribution is obtained from Equation 4.10. More details about the radiation transport method can be found in Kuiper et al. (2010). This hybrid radiation transport method is particularly good for PPDs, since it is able to resolve shadows in irradiated disks, in contrast to the pure FLD approximation (Kuiper & Klessen, 2013).

4.1.1 Initial conditions

The stationary solution of a sub-Keplerian disk was taken as initial conditions, which in spherical coordinates is given by

$$\rho = \rho_0 \left(\frac{r \sin\theta}{r_0 \sin\theta_0} \right)^{-\delta} \exp\left(\frac{\sin\theta - 1}{h^2} \right), \tag{4.11}$$

$$c_s = c_0 \left(\frac{r \sin\theta}{r_0 \sin\theta_0} \right)^{-\beta}, \tag{4.12}$$

$$v_r = 0, \tag{4.13}$$

$$v_\theta = 0, \tag{4.14}$$

$$v_\phi = \sqrt{v_K^2 + \frac{r}{\rho}\frac{\partial p}{\partial r}}, \tag{4.15}$$

where (r, θ, ϕ) are the spherical coordinates; $r_0 = 1$ au is a reference radius; $\theta_0 = \pi/2$ is a reference polar angle (midplane); $\rho_0 = 1.12 \times 10^{-10}$ g cm^{-3} is the density constant; $\delta = 1.5$ is the slope for the density distribution; $h = H/r = 0.05$ is the disk aspect ratio; $c_0 = h v_{K,p0}$ is the sound speed constant, where $v_{K,p0}$ is the initial Keplerian speed at the planet radius; $\beta = 0.5$ is the slope for the sound speed distribution; and v_K is the Keplerian speed.

4.1.2 Numerical setup

The description of the numerical methods used to solve the Euler equations can be found in Chapter 2 (Lobo Gomes et al., 2015) and for the radiation transport in Kuiper et al. (2010). We solved the problem in three dimensions, considering a spherical coordinates system. The coordinate system was centered at the system's barycenter. A logarithmic grid was used for the radial direction and a uniform one for the polar and azimuthal directions. The disk was integrated from 1.25 to 20 au in radius, from $\pi/2 \pm 0.2$ in polar ($\sim 4H$), and from 0 to 2π in azimuth. Reflective

or non-reflective boundary conditions were used for the radial and polar directions, see Table 4.1. The non-reflective boundary applies a zero gradient for all the fluid quantities, expect for the velocity, where inflow is not allowed. Periodic boundary conditions were used for the azimuthal direction for all the cases. Distances are given in units of $r_{cu} = 1$ au; densities in units of $\rho_{cu} = M_{\odot}/(au)^3$, which yields to a disk mass of $0.01 M_{\odot}$, and a disk-to-stellar mass ratio of 0.02, thus self-gravity can be neglected; and velocities in units of $v_{cu} = v_{K,0} = \sqrt{GM_{\star}/au}$, where G is the gravitational constant and $M_{\star}$ is the stellar mass.

Table 4.1 Simulations parameters

Label	(N_r, N_θ, N_ϕ)[a]	Planet[b]	BC$_r$[c]	BC$_\theta$[d]	T_{tot}[e] $(2\pi/\Omega_{p0})$
ISO	$(128, 64, 256)$	Free	R	R	100
ADI	$(128, 64, 256)$	Free	R	R	100
DR1	$(100, 20, 200)$	Fixed	NR	NR	66
DR2	$(100, 20, 200)$	Free	R	NR	100
SDR1	$(100, 20, 200)$	Fixed	NR	NR	53
SDR2	$(100, 20, 200)$	Free	R	NR	86

[a] Numerical resolution in the radial (N_r), polar (N_θ), and azimuthal (N_ϕ) directions.
[b] Free means that the planet is allowed to migrate, whereas fixed means that the planet is fixed at an orbital radius.
[c] Boundary conditions for the radial direction (R: reflective, NR: non-reflective).
[d] Boundary conditions for the polar direction (R: reflective, NR: non-reflective).
[e] Total time simulated in orbital units at the planet initial position.

We used the opacity of Weingartner & Draine (2001), which consists of 62.5% silicate and 37.5% graphite. Dust evaporation was disregarded, since the disk temperatures do not get higher than ~ 1000 K. The gas-to-dust mass ratio was assumed to be 100. A constant gas opacity of 0.01 cm^2 g^{-1} was considered. Radiation pressure was neglected, this approximation can be justified, because we expect that the thermal pressure should dominate over the radiation pressure. A T Tauri star with a mass of 0.5 $M_{\odot}$, a radius of 2.5 $R_{\odot}$, a luminosity of 1.43 $L_{\odot}$, and an effective temperature of 4000 K was considered. This means that our protostar has a few Myr and will become a K star, when it enters the main sequence. We did not follow the stellar evolution, since no evolution is expected in the timescales we simulated.

The simulations considered a planet-to-stellar mass ratio of $q = 10^{-3}$, equivalent to a Jupiter mass planet for a Sun-like star. The planet was initially located at 5 au. Table 4.1 presents each simulation label. The ISO simulation assumed a locally isothermal disk ($\gamma = 1.0001$), thus the temperature varies with radius, but not with time. The ADI simulation assumed an adiabatic disk, thus temperature is allowed to change with time, but we conserve entropy. The radiation transport equations were not solved for these two cases. These reference simulations are important to contrast with the cases where radiation transport is considered. The DRX[1] simulations include the dust thermal radiation, but neglects stellar irradiation. The disk thermal structure is set mostly by the balance between heating and cooling due to dust emission and absorption. Finally, the SDRX simulations include the full radiation transport treatment. The stellar irradiation also plays a role for the disk thermal structure, being a new source of heating. For this case, we had to wait for the disk structure to achieve an equilibrium solution, before adding the planet. A lower resolution was used for simulations DRX and SDRX, in order to be able to achieve a fair number of planetary orbits, using the computational time we could afford.

Two important simplifications were made. The first is regarding the planet accretion, as a first step, we do not model the planet accretion. This simplification can potentially influence the mass content inside the gap, leading to upper limits for the gap depth. The torque felt by the planet may also be altered. Klahr & Kley (2006) have observed strong fluctuations in the migration rate for models which do not include planet accretion; however, good agreement for the mean torque values averaged over time. Secondly, we assumed an inviscid disk, thus no heating from viscous accretion is modelled. This simplification may lead to wider gaps (Crida et al., 2006), as well as the process of gap opening may be facilitated. A more complete study should include both planet accretion and α-viscosity. Nevertheless, we leave it for a future study.

4.2 Models comparison

In this section, we compare the results for different models: locally isothermal (ISO), adiabatic (ADI), dust radiation (DR1), and stellar plus dust radiations (SDR1). We discuss the final density and temperature structures in the midplane and vertical direction and talk through the general characteristics of each model.

[1] X refers to the simulation number, see Table 4.1.

4.2.1 Midplane structure

Figure 4.1 presents midplane density maps for each model at their latest planetary orbit, see Table 4.1. The qualitative results for the ISO and ADI cases are very similar. A noticeable gap is opened and some matter is accumulated in the gap edges. The mass accumulation is greater for the ISO simulation. Vortex formation may take place at later times, as it is often observed in two-dimensional (2D) simulations of gap opening planets (e.g., de Val-Borro et al., 2007; Zhu & Stone, 2014; Fu et al., 2014; Les & Lin, 2015; Lobo Gomes et al., 2015). The centering of our coordinates system at its barycenter leads to the formation of two horseshoe regions at the planetary gap, in contrast to Chapter 2, where just one horseshoe region is formed. The reason for this discrepancy lies in the location of the system's center, the centering of the system at the star's center removes the Lagrange point L3, leading to the merging of the fluid around the Langrange points L4 and L5, thus the formation of a single horseshoe region.

The most standing difference between the ISO and ADI models is regarding the gap bottom density, which is much smaller for the ISO case. This shows that the locally isothermal approximation may yield to an overestimation for the gap depth. However, one would need to check whether the temperature treatment influences how much the gap is depleted or just the time that is needed for the mass to be depleted and a steady state for the gap structure to be achieved. We discuss the gap structure in Section 4.3.2, where we come back to this topic.

The DR1 model displays more differences with respect to the ISO and ADI cases. The gap takes much longer to be emptied out and its structure is greatly different. Instead of matter being accumulated around the Lagrange points L4 and L5, forming two horseshoe regions, it piles up behind the planet position at the Lagrange point L4. Since the gap is still not completely open, there is no accumulation of matter at the gap edges. It will be interesting to run this simulation for longer to check whether vortex formation takes place, possibly higher numerical resolution may be needed for that. The ISO and ADI simulations display a clear gap after 66 planetary orbits, indicating that when dust radiation is considered, gap opening becomes more difficult. We are considering inviscid simulations, meaning that a viscous torque is not present. One would expect that the gap opening process should be facilitated in the lack of viscosity. Crida et al. (2006) showed that a pressure torque may also counteract the gravitational torque for gap opening. We suggest that the pressure torque may be increased for the simulations with radiation transport included, delaying the gap opening or perhaps even halting it, before a completely clear gap is carved out.

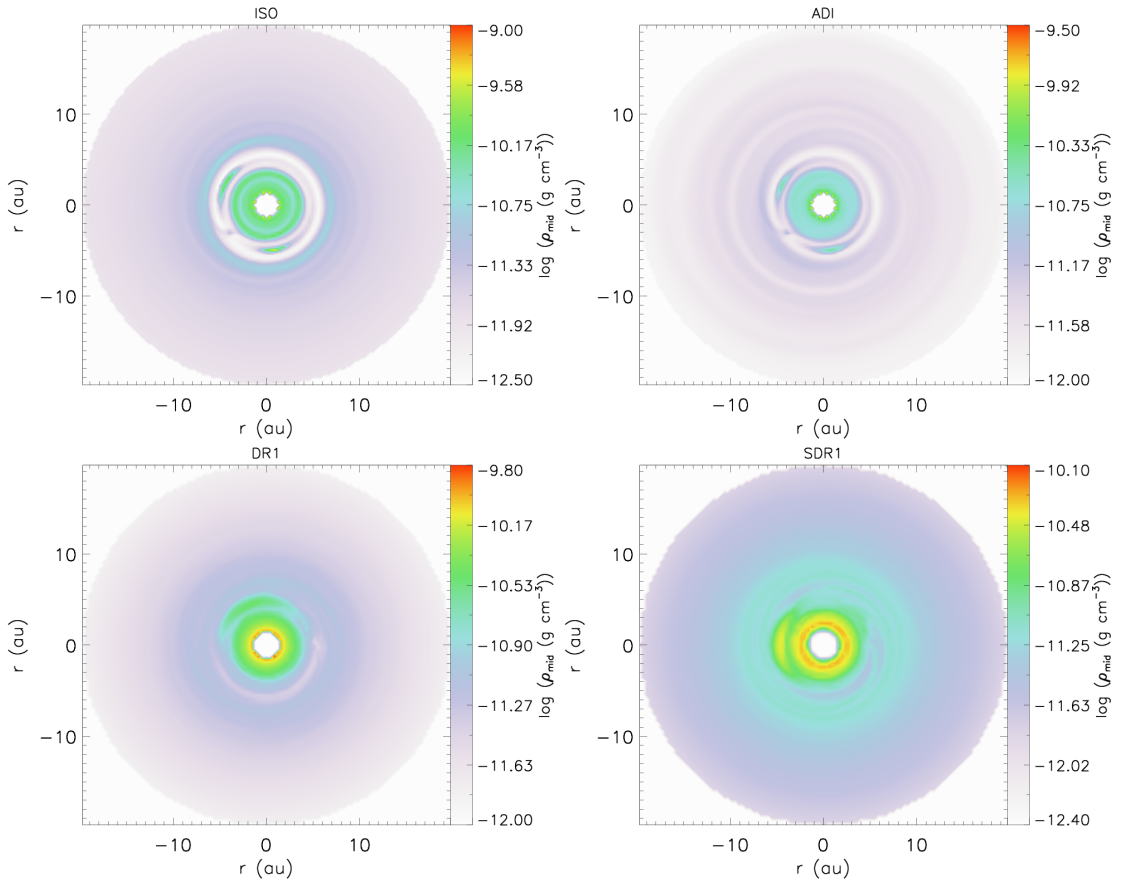

Figure 4.1 Midplane density maps for each model at their latest planetary orbit, see Table 4.1. The ISO model can be seen in the upper left panel, whereas the ADI model in the upper right panel, the DR1 model in the lower left panel, and the SDR1 model in the lower right panel.

The SDR1 model is similar to the DR1 in many aspects. The planetary gap takes also a long time to be carved out and the bottom density is even higher than for the DR1 case. Again, we suggest that the pressure torque may be high enough to hamper gap opening. The inclusion of stellar irradiation seems to boost this effect even more. One interesting feature of this model is that accumulation of mass also initially occurred around the Lagrange point L4, however after ~ 30 planetary orbits the blob of gas reduced its azimuthal velocity and was locked to the Lagrange point L3, therefore right opposite to the planet azimuthal position. The same effect may happen for simulation DR1 in a longer timescale.

Figure 4.2 shows the midplane temperature maps for each model at their latest planetary orbit, see Table 4.1. The discrepancies in the temperature maps for the ISO and ADI cases can be justified by the differences from their density maps. The inner disk region of the ADI simulation achieves much lower densities, therefore the temperature increases to maintain the vertical pressure equilibrium. The same

being true for the gap of the ISO simulation. Another prominent difference is the temperature at the horseshoe regions. For the ISO simulation the gas in the horseshoe region gets to a much lower temperature, due to the much higher densities. Now, it is important to mention that the ISO simulation represents a "quasi" locally isothermal case, since $\gamma = 1.0001$. However, the energy equation is being solved, thus variations from the temperature initial state are possible. Nevertheless, we observe deviations from the initial state only in the planetary gap region, which is a natural consequence of the gap opening.

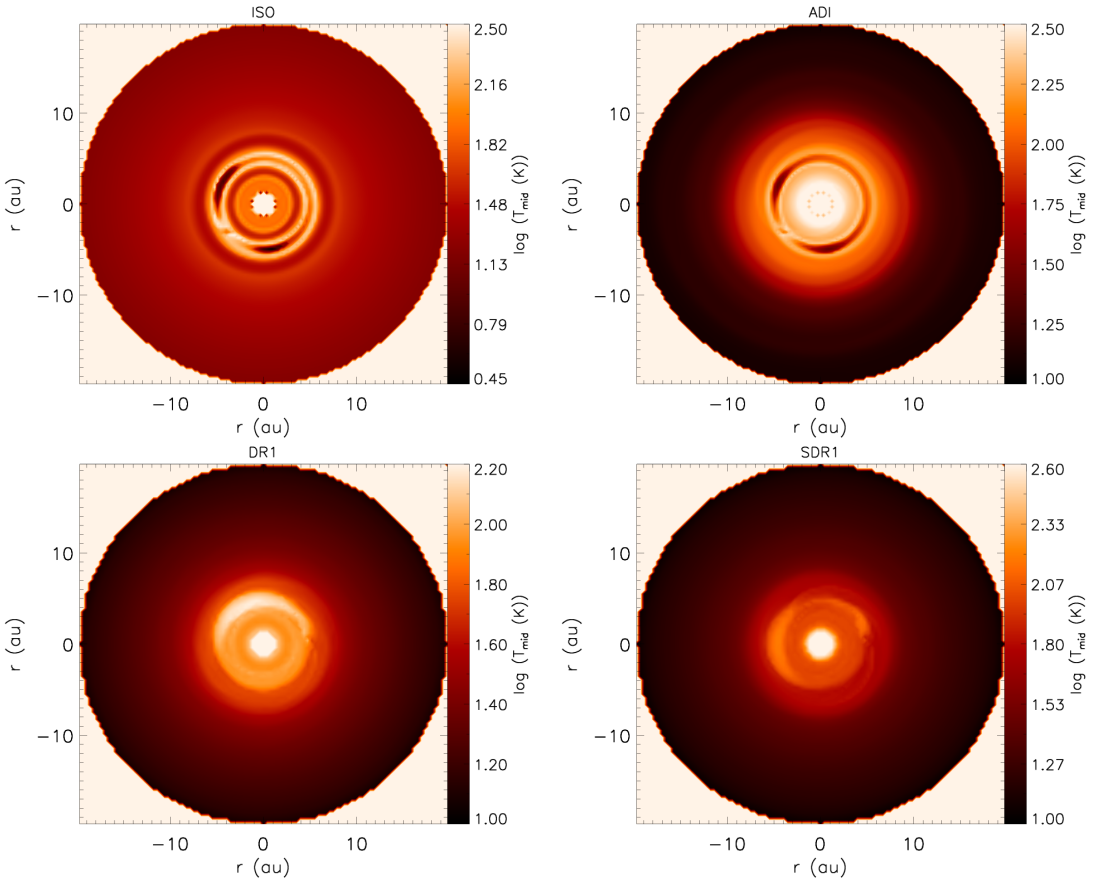

Figure 4.2 Midplane temperature maps for each model at their latest planetary orbit, see Table 4.1. The ISO model can be seen in the upper left panel, whereas the ADI model in the upper right panel, the DR1 model in the lower left panel, and the SDR1 model in the lower right panel.

Once more the DR1 simulation presents more differences. The outer disk is warmer than for the ADI simulation, on the other side, the inner disk is much colder. This temperature structure is the new equilibrium configuration after the planet initial disturbance. The blob of gas behind the planet achieves high temperatures, in contrast to the cool gas at the horseshoe region for the ISO and ADI cases. The high temperatures are due to the high densities, therefore high optical depths and

low cooling rates. A similar effect was observed by Klahr & Kley (2006), where a pressure supported atmosphere with constant temperature was build up around the planet. They explained that the constant temperature is due to the balance between the mass flux and radiation flux over the planet Roche lobe surface. In Klahr & Kley (2006) models, pile up of mass is observed at the planet's vicinity, even for non-accreting planet models. In our case, this effect seems to be much weaker. Nevertheless, our simulations should run for longer times in order to directly compare our results to theirs.

For the SDR1 model, we waited 30 orbits at 5 au before adding the planet. After $\sim$ 15 orbits, the disk already appeared to have achieved an equilibrium. As a result, the addition of the planet perturbation did not seem to influence the inner and outer disk. The equilibrium temperature for the inner disk is slightly higher than for the DR1 case, which seems to be a natural result from the inclusion of stellar irradiation. On the other hand, the equilibrium temperature for the outer disk is lower. The temperature of the blob of gas is higher in this case, due to the higher densities. Despite the blob moved from the L4 to the L3 Lagrange point, some mass remained close to the planet. We need to run this simulation for longer to check whether this material will pile up at the planet's Roche lobe or if it will remain locked to the Lagrange point L4.

4.2.2 Vertical structure

Figure 4.3 presents vertical density maps for each model at their latest planetary orbit, see Table 4.1. The ISO simulation clearly displays a cavity also in the vertical direction. The disk aspect ratio, which describes the disk geometry, is kept roughly constant at the outer regions, indicating that the planet perturbation alters the disk geometry only locally. For the ADI simulation the planetary gap is also visible in the vertical direction; however, the planet perturbation alters the disk geometry in the whole simulated disk. Strong vertical flows make the disk upper layers very "turbulent", even after 100 planetary orbits.

The planetary gap in the vertical direction is not prominent for the DR1 simulation. Vertical flows during the first planetary orbits are even stronger than for the ADI case; however, at later times they become weaker and the disk vertical structure finds an equilibrium. This effect was also observed by Klahr & Kley (2006) in their simulations with the TRAMP code. In their case, this effect was also stronger during the early gap opening phase. The SDR1 simulation displays a similar behaviour as the DR1. The vertical flows are also stronger during the first planetary orbits and the effect becomes weaker at later times. The planetary cavity

is also not as prominent as for the ISO and ADI simulations, which is natural, since the planetary gaps are shown to be much shallower for the simulations with radiation transport. About the vertical structure equilibrium before adding the planet, the disk achieved an equilibrium state also after ~ 15 orbits at the planet position.

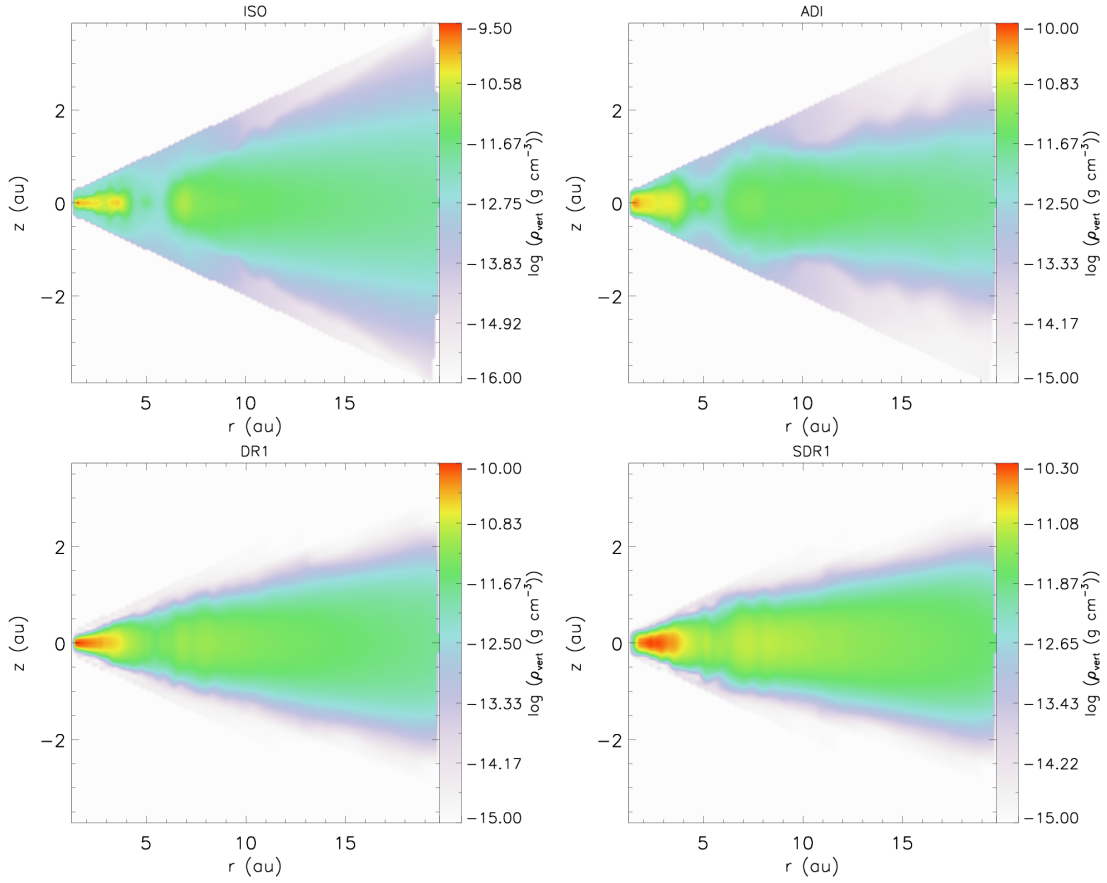

Figure 4.3 Vertical density maps for each model at their latest planetary orbit, see Table 4.1. A vertical cut centered at the planet azimuthal position is used. The ISO model can be seen in the upper left panel, whereas the ADI model in the upper right panel, the DR1 model in the lower left panel, and the SDR1 model in the lower right panel.

Figure 4.4 presents vertical temperature maps for each model at their latest planetary orbit, see Table 4.1. The planet is seen as a cold spot in the vertical temperature map of the ISO simulation. The disk upper layers get warmer, most likely due to the vertical flows induced by the planet perturbation. This effect is less pronounced in further distances from the planet, which is already expected from the analysis of the density map. The planet is also seem as a cold spot in the temperature map of the ADI simulation. The disk upper layers get warmer than in the ISO case and a larger vertical extent is heated up due to the planet

perturbation. This behaviour is again linked to the strong vertical flows observed in the density maps.

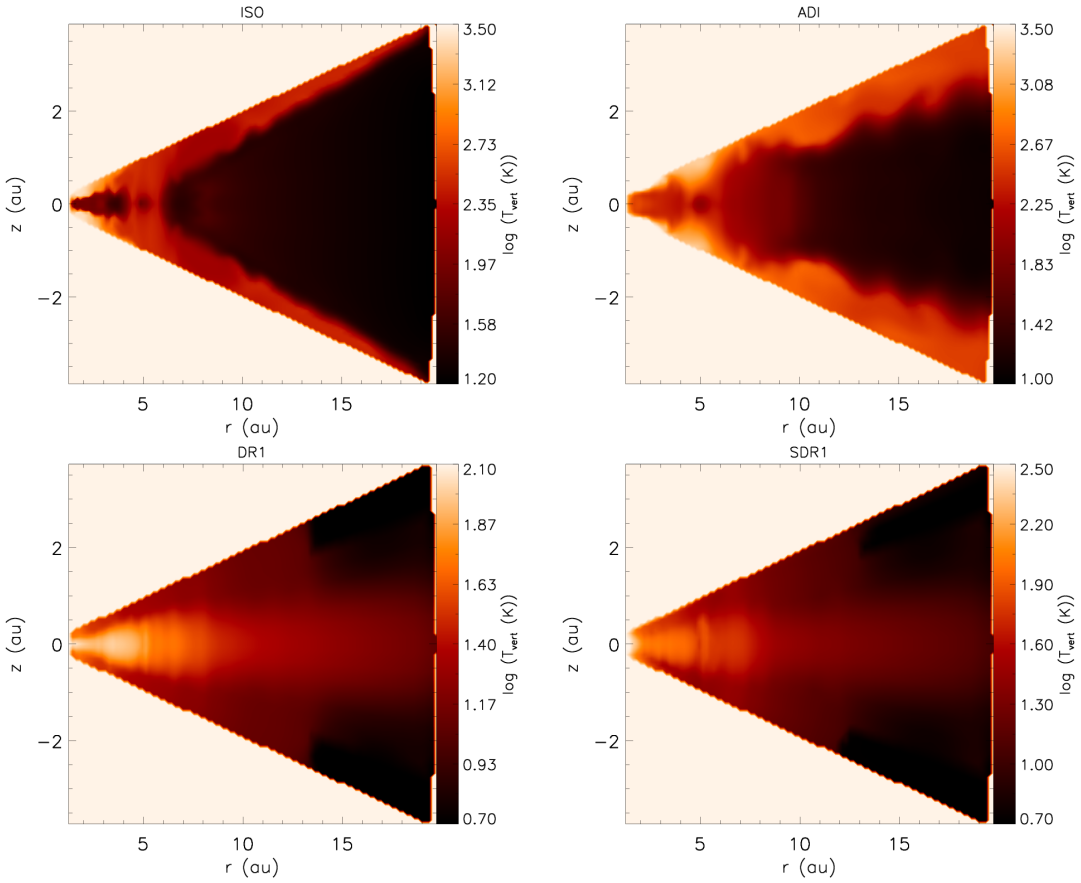

Figure 4.4 Vertical temperature maps for each model at their latest planetary orbit, see Table 4.1. A vertical cut centered at the planet azimuthal position is used. The ISO model can be seen in the upper left panel, whereas the ADI model in the upper right panel, the DR1 model in the lower left panel, and the SDR1 model in the lower right panel.

The DR1 and SDR1 simulations present again a similar behaviour. Once more the planet is not highlighted by any feature in the temperature vertical map, as it was not in the density map. Nevertheless, at the planet position the temperature is high, in opposition to the ISO and ADI cases, and naturally agreeing with the midplane maps. A second difference, with respect to the ISO and ADI cases, is that the temperature gets lower in regions of lower density. The explanation is that the gas can cool down very efficiently in such low density locations, because the optical depth is low. These underdensity regions at the disk upper layers in further distances from the planet are created due to the vertical flows.

Figure 4.5 shows the disk aspect ratio as a function of radius. For certain disk regions the disk aspect ratio can be well described by $H/r \propto r^{\alpha}$, when $\alpha = 0$

the disk has a constant aspect ratio, $\alpha > 0$ represents flared disks, and $\alpha < 0$ shadowed disks. As it was discussed, the disk geometry for the ISO simulation has not changed for large radii ($r > 10$ au). Nevertheless, at the planet's vicinity the disk geometry was greatly affected. In the inner disk region, the disk aspect ratio is kept roughly constant, thus the temperature slope has not changed; however, the aspect ratio is smaller than its initial value, indicating that the disk became slightly thinner. For the ADI simulation, at large radii ($r \gtrsim 10$ au), the disk aspect ratio is roughly constant, but in contrast to the ISO case its value slightly increased, thus the disk became slightly thicker. From the planet's vicinity until $r \sim 10$ au, the disk is shadowed, since the aspect ratio exponent is negative. On the other hand, in the inner disk region the disk is flared, since the disk aspect ratio exponent is positive.

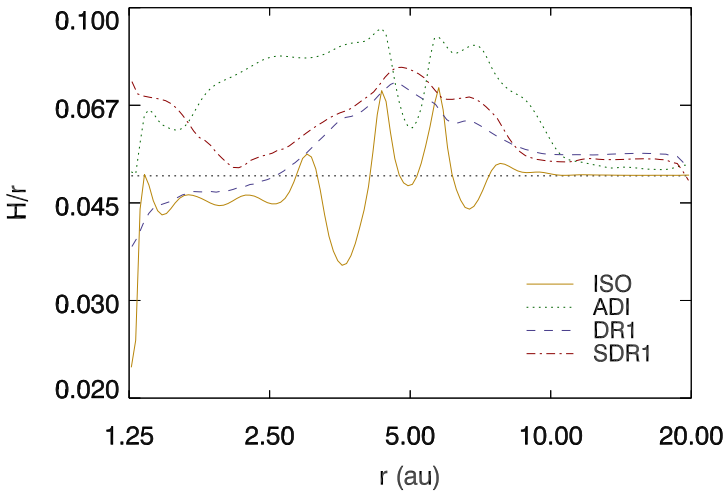

Figure 4.5 Disk aspect ratio as a function of radius for $t = 53$ planetary orbits. The disk aspect ratio was averaged over azimuth at the midplane. The dark orange solid line shows the ISO simulation, whereas the dotted green line the ADI simulation, the dashed blue line the DR1 simulation, and the dotted-dashed red line the SDR1 simulation. This plot has a log-log scale.

As previously touched upon, the planet disturbed the disk geometry much less for the cases where radiation transport was included. The DR1 simulation displays three main regions. In the inner disk region, until the planet position, the disk is flared. The disk becomes shadowed from the planet position until $r \sim 10$ au. The transition from flared to shadowed most likely occurs because the disk puffs up in the vertical direction, due to the planetary gap opening. From $r \sim 10$ au onwards, the disk aspect ratio is again roughly constant; however, its value increased as it happened for the ADI case. The SDR1 simulation is rather similar to the

DR1. Nevertheless, four main regions can be identified. The first one extends from the inner boundary until $r \sim 2$ au, where the disk is shadowed. The other three regions are exactly the same as for the DR1 simulation. The density maps in the vertical direction for simulations ISO, ADI, and DR1 have not changed much from $t = 53$ planetary orbits until their latest snapshots, which are shown in Figure 4.3. Therefore, the features expected from the interpretation of Figure 4.5 can be seen in Figure 4.3.

4.3 Radiation effects

In this section, we discuss some consequences that raise from the inclusion of radiation effects. Firstly, the migration behaviour of the high mass planet is investigated. At last, the gap structure for different treatments for the temperature structure is discussed.

4.3.1 Migration

One of the first most important things to considered to study, once radiative effects are included, is the planet migration. Thermal effects are known to play a major role for the migration of low mass planets, due to the so-called entropy-related horseshoe drag (e.g., Paardekooper & Mellema, 2006; Masset & Casoli, 2009, 2010; Paardekooper et al., 2011). In the high mass planet side, the migration is governed by the viscous evolution of the system (Lin & Papaloizou, 1986), because of the planetary gap, which leads to the planet isolation from the gaseous disk and cancelling out of the torques exerted by the disk on the planet. Nevertheless, we observed that the mass is not being efficiently depleted from the planet orbit, when radiation transport is included, which means that the planet may still feel the disk torques. Figure 4.6 shows the cumulative torques, averaged over time, for simulations ISO, ADI, DR1, and SDR1.

The torques for the ISO and ADI simulations are null, therefore the planet is not migrating for those cases. This result is expected for an inviscid model. Since viscosity is not present, there should not be any disk evolution, thus the planet should remain at its initial radius. It is also important to reinforce that the torques are cancelled out, only because a deep gap was carved out. Therefore the planet is indeed isolated from the gaseous disk.

The DR1 and SDR1 simulations, otherwise, display very high positive torques. In general, the inner disk applies positive torques (outward migration) and the outer disk negative torques (inward migration). The balance between these two

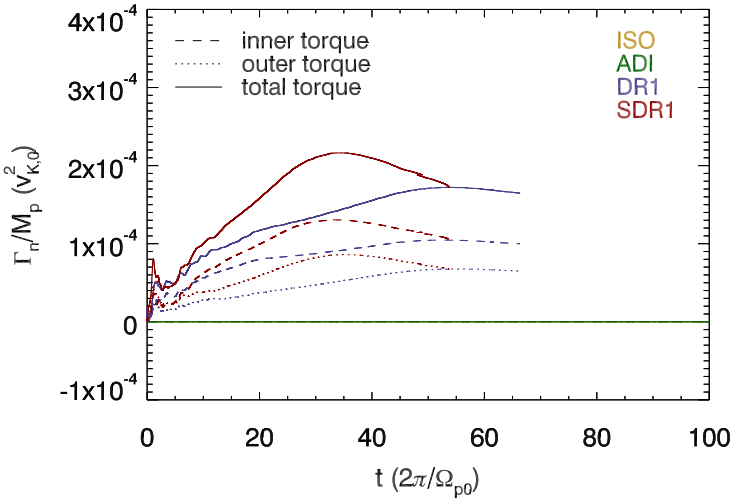

Figure 4.6 Cumulative averaged torques as a function of time. The dark orange lines show the ISO simulation, whereas the green lines the ADI simulation, the blue lines the DR1 simulation, and the red lines the SDR1 simulation. The dashed lines display the torque exerted by the inner disk, the dotted lines the torque exerted by the outer the disk, and the solid lines the total torques felt by the planet.

defines the direction of the planet migration. Here, we can see that even the torque coming from the outer disk is positive. In a low mass planet framework, this is possible when the horseshoe drag is positive and large enough to counteract the Lindblad torque. The theory of type I migration, in principle, cannot be applied for high mass planets, because it is assumed small perturbations for the torque calculation. Nevertheless, here we can see that the material in the planet's horseshoe region is strongly contributing for the torques applied on the planet. The physical origin of this effect is the same as for the low mass planet regime, even though the mathematical description may be different. Basically, the blob of gas formed behind the planet gives angular momentum to the planet, explaining the large positive torques. The ISO and ADI simulations present two horseshoe regions; however, since they are symmetric the net torque is null for these cases. It is important to remember that we neglected planet accretion. The planet accretion may help to deplete the mass in the gap region, therefore also modifying the torque felt by the planet. This effect will be studied in a future work.

The planet was kept at a fixed radius for simulations DR1 and SDR1. New simulations allowing the planet to move were run: DR2 and SDR2, see Table 4.1. Figure 4.7 shows the cumulative torques, averaged over time, for these new simulations. In the left side simulations with dust radiation included are shown, whereas in the right side simulations with dust radiation and stellar irradiation.

The simulations with a fixed planet display higher values for the torques, indicating that this approximation may lead to an overestimation for the torques. The larger torques for these simulations can be explained by the blob that is created behind the planet. In the case when the planet is fixed, this blob is more massive, thus it exchanges more angular momentum. The general behaviour for the torque curves, however, appear to be consistent. For the DRX simulations, there is an initial sharp growth for the total torque and at later times this torque saturates, when the blob of gas stops to grow. In the simulation with a fixed planet it took longer for this torque to saturate. The torque saturation for this simulation should be confirmed by running this simulation for a longer time. A similar behaviour is seen for the SDRX simulations. In this case, a bump is observed, which is followed by torque saturation. For the SDRX simulations, the blob of gas formed behind the planet moves from the Lindblad point L4 to L3, explaining the decrease of the torque after some time. The timescales are again longer for the simulation with a fixed planet. The torque saturation should also be confirmed by running this simulation for a longer time.

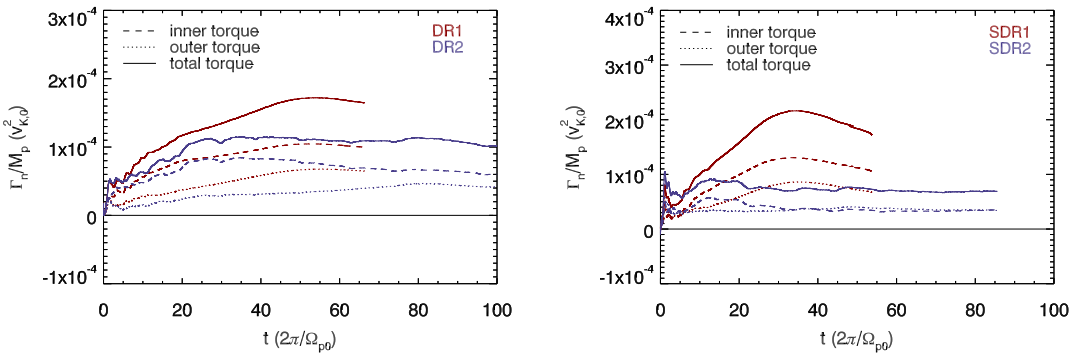

Figure 4.7 Cumulative averaged torques as a function of time for simulations including radiation transport. In the left side, simulations with only dust radiation are shown. The red lines show the DR1 simulation and the blue lines the DR2 simulation. In the right side, simulations with dust radiation and stellar irradiation included are shown. The red lines show the SDR1 simulation and the blue lines the SDR2 simulation. The dashed lines display the torque exerted by the inner disk, the dotted lines the torque exerted by the outer the disk, and the solid lines the total torques felt by the planet.

4.3.2 Gap structure

We already established that the gap is much shallower for simulations with radiation transport. Therefore a second interesting thing to study is the gap structure. A

good comprehension of planetary gap structures is essential to interpret recent observations of cavities in PPDs (e.g., Quanz et al., 2013; Debes et al., 2013). Figure 4.8 displays the surface density profiles averaged in azimuth for the ISO, ADI, DR1, and SDR1 simulations at $t = 53$ planetary orbits. Surface densities are the right quantity to examine, since observations measure column densities. We expect that in the near future observations with the ALMA observatory may give good measurements of the surface densities of the recent detected cavities.

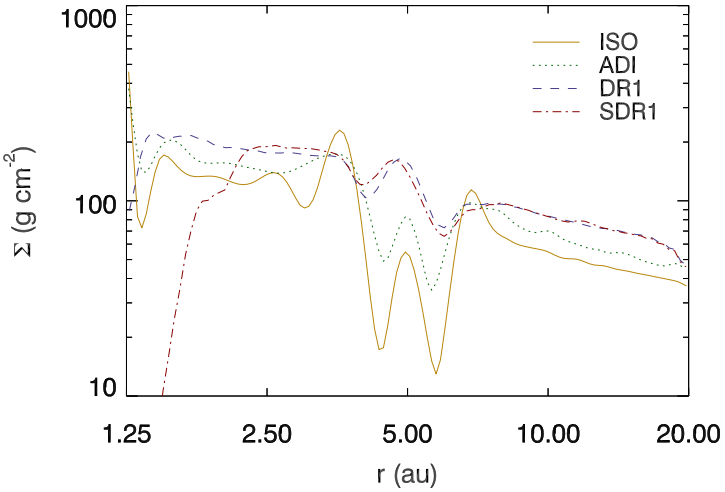

Figure 4.8 Surface density profiles averaged in azimuth for $t = 53$ planetary orbits. The dark orange solid line shows the ISO simulation, whereas the dotted green line the ADI simulation, the dashed blue line the DR1 simulation, and the dotted-dashed red line the SDR1 simulation. This plot has a log-log scale.

The first outstanding feature in Figure 4.8 is the gap depths. The more physics we add, the shallower the gap is at a certain time. The gap widths in contrast agree pretty well, indicating that the gravitational torques are cancelled out at a similar location for a certain time. Both gap width and depth evolve with time for simulations ISO and ADI from $t = 53$ planetary orbits until the end of the simulation. One needs to wait around 100 planetary orbits to get a steady state gap for both models, see Figure 4.9. We need to run simulations DR1 and SDR1 for longer times, until the planetary gap achieves a steady state. Just then, we can state final conclusions regarding the gap shapes. Still, the planetary gap is deeper for the ISO model than for the ADI model, thus one can suspect that the same will remain true for the DR1 and SDR1 models.

Figure 4.10 shows the gap profiles for the DR1, DR2, SDR1, and SDR2 simulations. The most important conclusion is that when the planet is allowed to move, the gap opening process gets even more difficult. The gaps appear as a very

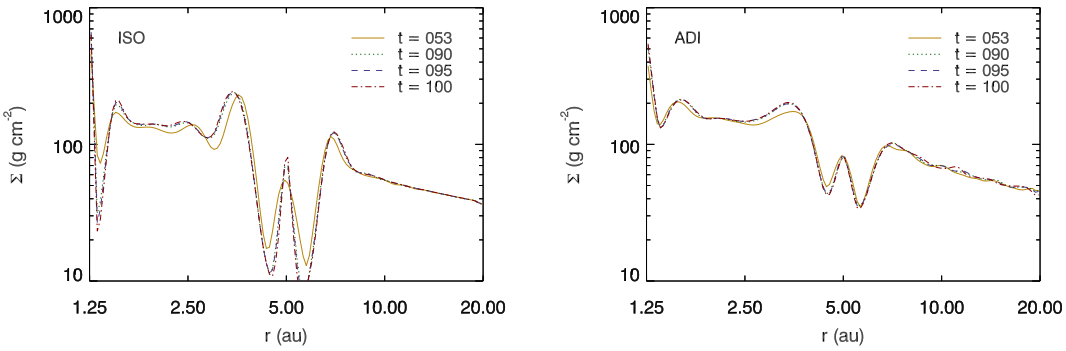

Figure 4.9 Surface density profiles averaged in azimuth at different times for the ISO and ADI simulations. In the left side the ISO simulation is shown, whereas in the right side the ADI simulation. The solid dark orange line shows the result for $t = 53$ planetary orbits, the dotted green line for $t = 90$ planetary orbits, the dashed blue line for $t = 95$ planetary orbits, and the dotted-dashed red line for $t = 100$ planetary orbits. This plot has a log-log scale.

smooth feature in the surface density profiles of simulations DR2 and SDR2. We still need to understand whether there is a physical reason for this behaviour or whether numerical factors are playing a role and giving misleading results.

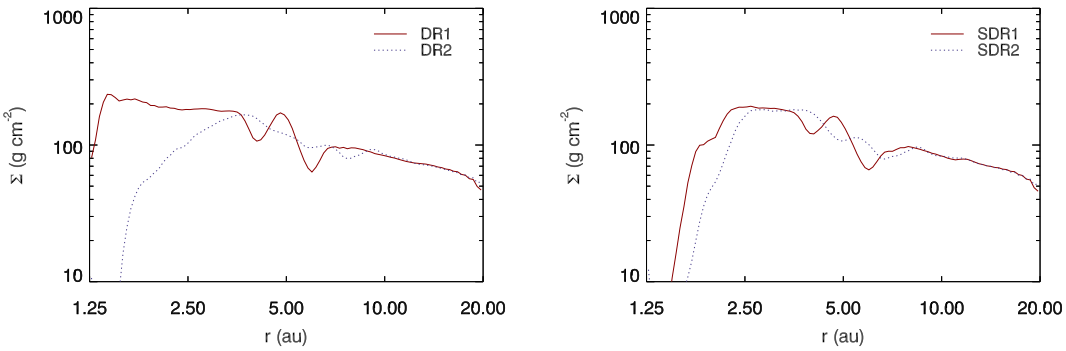

Figure 4.10 Surface density profiles averaged in azimuth for simulations including radiation transport. In the left side, simulations with only dust radiation are shown, the results stand for $t = 66$ planetary orbits. The red solid line shows the DR1 simulation and the dashed blue line the DR2 simulation. In the right side, simulations with dust radiation and stellar irradiation included are shown, the results stand for $t = 53$ planetary orbits. The red solid line shows the SDR1 simulation and the dashed blue line the SDR2 simulation. This plot has a log-log scale.

According to our knowledge, the only study that considered gap opening planets in disks with radiation transport coupled to hydrodynamics was Klahr & Kley (2006). Nevertheless, they were interested in planet accretion and to find the

numerical setup that gives more accurate results. The planet was fixed at a certain radius in their studies, as our simulations DR1 and SDR1. Moreover, they added an initial gap artificially in most of their simulations, since they wanted to look for planet accretion. Nonetheless, they considered two models with non-accreting planets, following the gap opening from the beginning. The only difference between these two models is the numerical resolution close to the planet position. Their DN model has a very similar setup to our DR1 model, whereas their DN4 model is also similar, but with a much higher numerical resolution near the planet. Figure 9 in their paper shows the surface density profiles for models DN and DN4. The gap shape of the DN4 model for $t = 55$ planetary orbits is rather similar to the gap shape of our model DR1. The gap profile for their DN model is presented for $t = 141$ planetary orbits. Therefore we should run our DR1 simulation for a longer time, to be able to directly compare our model to their DN model, which has a similar setup as ours.

4.4 Summary and conclusions

High mass planets are able to carve out gaps in their parent disks, becoming isolated from the gaseous gas. Recently, cavities have been observed in several PPDs. In particular in the systems HD 169142 (Quanz et al., 2013) and TW Hya (Debes et al., 2013), the cavities display a similar structure as it is expected from planet-disk interactions. It is important to have a good understanding of planetary gap structures, in order to be able to interpret these recent observations. In this chapter, we run 3D RT-HD global simulations with the PLUTO code, where dust radiation and stellar irradiation were included, to study the interaction between gap opening planets and their parent disks. We compare the models with radiation transport to locally isothermal and adiabatic models.

The qualitative results for the locally isothermal and adiabatic models agree pretty well. Nevertheless, the planetary gap structures are different. The locally isothermal model displays a much deeper gap than the adiabatic one. The second most important difference is regarding how much the planet perturbation affects the disk vertical structure. For the locally isothermal case, the planet affects the disk only locally. For the adiabatic case, the planet influences the disk in the whole simulated area, even changing the disk geometry. Strong vertical flows induced by the planet perturbation are observed in both cases; however, this effect does not last for long in the locally isothermal model, whereas for the adiabatic model this effect persists until the end of the simulation.

The addition of dust radiation greatly influenced the results. The planetary gap opening process became more difficult and the gap depth even shallower than for the adiabatic case. We suspect that a stronger pressure torque may be the reason for that. Mass piled up behind the planet position, leading to the formation of a very warm blob of gas. Vertical flows induced by the planet perturbation were also observed. Nonetheless, they last for a shorter time, when compared to the adiabatic model. This same effect was seen by Klahr & Kley (2006) in their simulations of gap opening planets with dust radiation included. The planet perturbation led to the flaring of the inner disk and shadowing of the outer disk until $r \sim 10$ au.

The addition of stellar irradiation in top of dust radiation gives an even better description of the disk temperature structure. The model with both ingredients displayed even more differences to the locally isothermal and adiabatic models, than the one with just dust radiation included. In general, the model with stellar irradiation added agrees well with the one with just dust radiation included. The first important difference is with respect to the gap structure, in this case the gap depth is even shallower. A warm blob of gas is also formed behind the planet. Its azimuthal velocity is reduced with time and therefore it moves from the Lagrange point L4 to L3, which is right opposite the planet azimuthal location. Vertical flows were also observed and they last for a short time, as for the locally isothermal and only dust radiation models. The flaring of the inner disk and shadowing of the outer disk until $r \sim 10$ au was also observed; however, in the very inner disk a transition from flared to shadowed was also observed.

The planet migration for the different models was also studied. The total torque felt by the high mass planet in the locally isothermal and adiabatic models is null. This result is expected, since we considered an inviscid disk, therefore no disk evolution is expected and the planet should remain locked at its initial position. The torques in the cases with radiation transport included, however, are very high and positive, which leads to outward migration. This highly positive torque is caused by the blob of gas just behind the planet, which gives angular momentum to the planet. For the model with stellar irradiation included, this blob of gas moved from the Lagrange point L4 to L3, reducing the torque applied on the planet at later times.

The planet was kept fixed at an orbital radius in the two aforementioned models with radiation transport. Two additional models, where the planet was allowed to move, were considered. For both cases, the gap opening process became even more difficult. We need still to understand whether there is a physical reason behind this behaviour or whether this is a result of numerical issues. Since the blob of gas that forms behind the planet is less massive when the planet is allowed to move, lower

torques were observed. This shows that the fixing of the planet at a certain orbital radius leads to an overestimation of the torques and migration rates.

We need to run the simulations with radiation transport for longer times, until the gap structure achieves a steady state. After that, we can give final conclusions regarding the gap structure. Once more orbits are simulated, we can also directly compare our results to the ones obtained by Klahr & Kley (2006) with their simulations with dust radiation.

This work is a big step to a better understanding of the interaction between high mass planets and their parent disks, considering a better treatment for the disk temperature structure. Nevertheless, models including viscosity and planet accretion should be carried out. Viscosity is an important ingredient for the gap opening process, therefore it should not be completely neglected. Planet accretion is also important, since it helps to deplete the mass inside the planetary gap. Moreover, the torques felt by the planet may be changed due to gas accretion. Models with planet accretion can also be used to study circumplanetary disks. In particular in this case, the consideration of radiative effects is important, since it plays a role for the contraction of the planet envelope. Finally, our simulations can be used to predict observational signatures that can be observed by ALMA, such kind of studies have been successfully carried out lately (e.g., Ruge et al., 2013, 2014).

Chapter 5

Summary, conclusions, and future perspectives

The goal of this thesis was to study several aspects of planet-disk interactions in non-isothermal disks. The inclusion of the temperature evolution is of great importance, since the disk thermodynamics is shown to play a role in many scenarios. As a whole, the study of planet-disk interactions is essential for the understanding of the large variety of exoplanets that have been observed. Different disk parameters, as well as distinct processes coming from the interaction of planets with their parent disks may lead to the formation of diverse stellar systems. Moreover, a good comprehension of the interplay between forming planets and their parent disks may give constraints to planet formation theories. Because the reliability of a planet formation model should be sustained by the prospect that a formed planet at a certain orbital radius can survive through the several stages of disk evolution. In this thesis, hydrodynamical (HD) numerical simulations were performed with the PLUTO code (Mignone et al., 2007), using the planet-disk module developed by Uribe et al. (2011) to tackle some open questions.

The formation and evolution of vortices induced by high mass planets was investigated in Chapter 2. Vortices are important structures in several contexts. They are good candidates to trap dust particles, preventing them to quickly drift towards the central star and allowing them to grow to bigger sizes. Therefore they are a good channel to overcome the radial drift barrier for planet formation. They may also explain angular momentum transport through the disk dead zone, which is essential to allow for inward accretion. The exchange of angular momentum between waves in the inner and outer side of the vortex position leads to a negative net flux of angular momentum and therefore a positive flux of mass. Finally, vortices may

also trap planet cores, slowing down the core migration towards the central star, easing the timescale problem of the rapid inward drift of small objects.

Dust asymmetries have recently been observed in several transition disks, e.g., in the Oph IRS 48 system (van der Marel et al., 2013). These features may be explained by the presence of large-scale vortices born at the outer edge of a planetary gap. Motivated by these observations, several recent studies have focused on the formation and evolution of planet-induced vortices. Questions regarding the lifetimes of these features and whether they are able to trap dust particles are fundamental to check if they can explain these recent observations. In Chapter 2, we performed two-dimensional (2D) global HD simulations to investigate planet-induced vortices. A Newtonian cooling approach (thermal relaxation) was used to evolve the disk temperature structure. The main aim of Chapter 2 was to assess the importance of radial buoyancy for the development of planet-induced vortices. We found that unstable radial buoyancy leads to smoother planetary gap edges, therefore weaker vortices are generated. An interesting outcome of this study was the observation of a second generation of vortices. The first generation of vortices is formed in the outer wall of the planetary gap due to the triggering of the Rossby wave instability (RWI). The merged primary vortex induces accretion, which depletes the mass on its orbit. This process creates a surface density enhancement beyond the primary vortex position. The second generation of vortices arises in this surface density enhancement, indicating that the bump in this region is sufficient to trigger the RWI once more.

In light of this finding, we modeled the Oph IRS48 system. The main objective was to check whether the second generation of vortices would also be formed. The hypothesis that a planet-induced vortex is the reason for the asymmetric feature in this system has a major problem: the location of the asymmetry cannot be explained by a vortex at the planetary gap edge, since the vortex location is very far from the possible planet location. We observed a second generation of vortices in the model of this system, therefore posing a promising explanation for the location of the vortex. Lastly, the primary vortices' lifetimes, as well as the secondary vortices' birth times, were found to be dependent on the disk thermal relaxation timescale. Therefore the cooling properties of the disk play a role for the generation and maintenance of these structures.

Type I migration is another aspect of planet-disk interactions, where the thermodynamics of the disk is shown to be important. Therefore, we investigated the long-term evolution of the migration of low mass planets in non-isothermal disks in Chapter 3. Low mass planets typically experience type I migration, which is governed by the Lindblad torque and the horseshoe drag. The former being the

gravitational torque due to spiral density waves launched by the planet. The latter being the torque exerted by fluid elements executing a U-turn around the planet. A problem related to type I migration is the timescales predicted by isothermal models, which are much shorter than the typical disk lifetimes. It would not be possible to explain the observed mass-distance distribution of exoplanets with such fast migration rates. Recent works have shown that non-isothermal effects can increase the horseshoe drag, which leads to slower migration rates or even the reversal of the migration direction. Nevertheless, there are still questions related to this subject. How can the saturation of the horseshoe drag be prevented, such that slow type I migration is sustained? This is an important question to address.

We used global 2D-HD simulations, with the same cooling approach as in Chapter 2, to study the unsaturation of the horseshoe drag. Radial stratification in combination with thermal relaxation can lead to the development of a convective instability, which generates and amplifies vortices. Hydrodynamical instabilities can cause turbulence. The main goal of Chapter 3 was to check whether turbulence-triggered viscosity due to unstable radial buoyancy can sustain the unsaturation of the horseshoe drag, which is essential to balance or counteract the Lindblad torque. We found that the disk parameters that favor slow/outward migration oppose the amplification of vortices. Therefore this is not a good mechanism to prevent the saturation of the horseshoe drag. However, we observed that the planet perturbation leads to the formation of vortices in the horseshoe region. These vortices get amplified and excite spiral waves, leading to fast inward vortex migration. The continuous planet perturbation results in permanent vortex formation. The process of constant creation and amplification of vortices, that later migrate to the inner disk, depletes the matter in the inner side of the planet orbit. The planet remains trapped in the outer edge of this underdensity. This result is a new promising mechanism to prevent the fast type I migration rates in regions of the disk that are buoyantly unstable.

We studied the interaction between high mass planets and their parent disks in Chapter 4. The main goal was to investigate the influence of radiative effects for planetary gap structure. High mass planets are able to carve out a gap in their parent disks, when the gravitational torque from the planet spiral density waves is able to counteract the disk viscous and pressure torques. The gravitational torque pushes the inner disk inwards and the outer disk outwards, opening up a gap. It is important to understand the surface density inside the planetary gap, since the material in the planet's horseshoe region may be able to apply torques on the planet, possibly influencing the planet migration and eccentricity evolution. Moreover, cavities have recently been observed in protoplanetary disks. To interpret

these recent observations, we should have a good comprehension of planetary gap structures.

We used three-dimensional (3D) global radiative-hydrodynamical (RT-HD) simulations, including dust radiation as well as stellar irradiation. Such simulations were possible by merging the planet-disk and radiation transport (Kuiper et al., 2010) PLUTO modules. The simulations with radiation transport were compared to locally isothermal and adiabatic 3D models, in order to assess the influence of radiative effects. We found that the planetary gap depth becomes shallower as more physics is included. Thus, the locally isothermal model displayed a deeper gap, whereas the model with dust radiation and stellar irradiation presented a shallower gap. The gap opening process was also found to become more difficult as more physics is included. We suspect that a stronger pressure torque may be the cause for that. The formation of a blob of gas behind the planet was observed for the models with radiation transport. This blob moved from the Lagrange point L4 to L3 for the model that included dust radiation and stellar irradiation. Strong vertical flows induced by the planet perturbation were observed for all models. These vertical flows last for a short time for all models, except for the adiabatic one, where they are still observed by the end of the simulation. The planet disturbance influenced the disk geometry in all cases. Nevertheless, this influence is only local for the isothermal model, whereas it is extended to the whole simulated area for the other models. Transitions from a constant disk aspect ratio to flared and shadowed regions were observed.

The planet was found to be in a stable orbital radius for the locally isothermal and adiabatic models. This behaviour was expected, since we considered an inviscid disk, thus the planet should not migrate, as there is no disk viscous evolution. On the other hand, a strong positive torque was observed for the models with radiation transport, which leads to outward migration. This torque is applied by the blob of gas behind the planet, which gives angular momentum to the planet. The previously mentioned models, with radiation transport, placed the planet at a fixed orbital radius, for simplification. New models, allowing the planet to move, were run. We observed that the gap opening process became even more difficult for the models where the planet was moving. We still need to understand whether there is a physical reason for that or whether numerical issues led to misleading results.

This thesis brought new insights to the subject of planet-disk interactions. In particular, we took into account the disk temperature evolution in all of our projects, which is often disregarded in this subject. There is still a long way to go to fully explain the birth and settlement of stellar systems and to understand the origin

of the many flavours these systems can have. Many of the open questions are raised as a result of the observation of curious protoplanetary disks and exoplanets. New observatories with high angular resolution and powerful instruments will be able to put many of the present theories to the test and hopefully prove some of them. RT-HD simulations may help with a more precise modelling of these recently observed systems. After this thesis, such simulations are now possible to be carried out with the PLUTO code.

From a theoretical point of view, a next important step is to study the gas accretion of embedded planets with masses greater than about $10M_{\oplus}$. Such studies are important for the numerical modelling of the gas accretion phase in the formation of high mass planets via the core accretion scenario and to model circumplanetary disks. In order to make these simulations more realistic, one needs to implement the radiative feedback of accreting planets to the disk, since this mechanism is essential to understand the contraction of the planet envelope. The coupling of the RT-HD simulations to magnetic fields is also important. In particular for the previously mentioned problem, magnetic fields seem to lead to lower gas accretion rates into the planet (Uribe et al., 2013). The importance of non ideal magnetohydrodynamical (MHD) effects have also been established (Keith & Wardle, 2015). However, studies including both radiation and magnetic fields have never been done, since they are computationally highly expensive and challenging. Nevertheless, first attempts should already be possible with present day computing facilities. RT-MHD simulations may also be important for a better description of outer disk layers, as well as the inner disk regions, where both stellar irradiation and magnetic fields are already known to play a major role. Finally, studies concentrated in multiple planets systems are getting increasing attention, motivated by several recent observations of such systems. The incorporation of multiple planets to the planet-disk module of the PLUTO code is rather straightforward, therefore such simulations can easily be carried out.

Bibliography

Adams, F. C., & Bloch, A. M. 2009, ApJ, 701, 1381

Akiyama, E., et al. 2015, ApJl, 802, L17

Albrecht, S., et al. 2012, ApJ, 757, 18

Alexander, R. D., Clarke, C. J., & Pringle, J. E. 2006, MNRAS, 369, 229

Alibert, Y., Mordasini, C., & Benz, W. 2004, A&A, 417, L25

Andrews, S. M., Rosenfeld, K. A., Wilner, D. J., & Bremer, M. 2011, ApJl, 742, L5

Armitage, P. J. 2013, Astrophysics of Planet Formation

Artymowicz, P. 1993a, ApJ, 419, 166

—. 1993b, ApJ, 419, 155

Ataiee, S., Dullemond, C. P., Kley, W., Regály, Z., & Meheut, H. 2014, A&A, 572, A61

Ataiee, S., Pinilla, P., Zsom, A., Dullemond, C. P., Dominik, C., & Ghanbari, J. 2013, A&A, 553, L3

Aumann, H. H. 1985, PASP, 97, 885

Aumann, H. H., et al. 1984, ApJl, 278, L23

Balbus, S. A., & Hawley, J. F. 1991, ApJ, 376, 214

Balmforth, N. J., & Korycansky, D. G. 2001, MNRAS, 326, 833

Bans, A., Königl, A., & Uribe, A. 2015, ApJ, 802, 55

Barge, P., & Sommeria, J. 1995, A&A, 295, L1

Baruteau, C., et al. 2014, Protostars and Planets VI, 667

Baruteau, C., Fromang, S., Nelson, R. P., & Masset, F. 2011, A&A, 533, A84

Baruteau, C., & Lin, D. N. C. 2010, ApJ, 709, 759

Baruteau, C., & Masset, F. 2008a, ApJ, 672, 1054

—. 2008b, ApJ, 678, 483

Batalha, N. M., et al. 2013, ApJs, 204, 24

Bate, M. R., Lodato, G., & Pringle, J. E. 2010, MNRAS, 401, 1505

Batygin, K. 2012, Nature, 491, 418

Benisty, M., et al. 2015, ArXiv e-prints

Benítez-Llambay, P., Masset, F., Koenigsberger, G., & Szulágyi, J. 2015, Nature, 520, 63

Birnstiel, T., Dullemond, C. P., & Pinilla, P. 2013, A&A, 550, L8

Bitsch, B., Crida, A., Libert, A.-S., & Lega, E. 2013, A&A, 555, A124

Bitsch, B., & Kley, W. 2010, A&A, 523, A30

—. 2011, A&A, 530, A41

Boss, A. P. 1997, Science, 276, 1836

Bracco, A., Chavanis, P. H., Provenzale, A., & Spiegel, E. A. 1999, Physics of Fluids, 11, 2280

Brown, J. M., Blake, G. A., Qi, C., Dullemond, C. P., Wilner, D. J., & Williams, J. P. 2009, ApJ, 704, 496

Brown, J. M., Herczeg, G. J., Pontoppidan, K. M., & van Dishoeck, E. F. 2012, ApJ, 744, 116

Cameron, A. G. W. 1978, Moon and Planets, 18, 5

Casassus, S., et al. 2013, A&A, 553, A64

Casoli, J., & Masset, F. S. 2009, ApJ, 703, 845

Chandrasekhar, S., & Fermi, E. 1953, ApJ, 118, 116

Chatterjee, S., Ford, E. B., Matsumura, S., & Rasio, F. A. 2008, ApJ, 686, 580

Chiang, E. I., & Goldreich, P. 1997, ApJ, 490, 368

Clarke, C. J., Gendrin, A., & Sotomayor, M. 2001, MNRAS, 328, 485

Correia, A. C. M., et al. 2009, A&A, 496, 521

Cresswell, P., Dirksen, G., Kley, W., & Nelson, R. P. 2007, A&A, 473, 329

Cresswell, P., & Nelson, R. P. 2008, A&A, 482, 677

Crida, A., Morbidelli, A., & Masset, F. 2006, Icarus, 181, 587

Crida, A., Sándor, Z., & Kley, W. 2008, A&A, 483, 325

D'Angelo, G., & Lubow, S. H. 2010, ApJ, 724, 730

D'Angelo, G., & Marzari, F. 2012, ApJ, 757, 50

de Val-Borro, M., Artymowicz, P., D'Angelo, G., & Peplinski, A. 2007, A&A, 471, 1043

Debes, J. H., Jang-Condell, H., Weinberger, A. J., Roberge, A., & Schneider, G. 2013, ApJ, 771, 45

Dittkrist, K.-M., Mordasini, C., Klahr, H., Alibert, Y., & Henning, T. 2014, A&A, 567, A121

Dong, R., Rafikov, R. R., & Stone, J. M. 2011a, ApJ, 741, 57

Dong, R., Rafikov, R. R., Stone, J. M., & Petrovich, C. 2011b, ApJ, 741, 56

Drążkowska, J., Windmark, F., & Dullemond, C. P. 2013, A&A, 556, A37

—. 2014, A&A, 567, A38

Duffell, P. C. 2015, ApJl, 807, L11

Duffell, P. C., & MacFadyen, A. I. 2012, ApJ, 755, 7

—. 2013, ApJ, 769, 41

Dullemond, C. P., & Dominik, C. 2005, A&A, 434, 971

Dunhill, A. C., Alexander, R. D., & Armitage, P. J. 2013, MNRAS, 428, 3072

Dutrey, A., Lecavelier Des Etangs, A., & Augereau, J.-C. 2004, The observation of circumstellar disks: dust and gas components, ed. M. C. Festou, H. U. Keller, & H. A. Weaver, 81–95

Dzyurkevich, N., Flock, M., Turner, N. J., Klahr, H., & Henning, T. 2010, A&A, 515, A70

Eisner, J. A., Hillenbrand, L. A., Carpenter, J. M., & Wolf, S. 2005, ApJ, 635, 396

Elsasser, H., & Staude, H. J. 1978, A&A, 70, L3

Epstein, P. S. 1924, Phys. Rev., 23, 710

Fendyke, S. M., & Nelson, R. P. 2014, MNRAS, 437, 96

Field, G. B. 1978, in IAU Colloq. 52: Protostars and Planets, ed. T. Gehrels, 243–264

Finkenzeller, U., & Mundt, R. 1984, A&As, 55, 109

Fischer, D. A., Howard, A. W., Laughlin, G. P., Macintosh, B., Mahadevan, S., Sahlmann, J., & Yee, J. C. 2014, Protostars and Planets VI, 715

Flock, M., Dzyurkevich, N., Klahr, H., Turner, N. J., & Henning, T. 2011, ApJ, 735, 122

Flock, M., Ruge, J. P., Dzyurkevich, N., Henning, T., Klahr, H., & Wolf, S. 2015, A&A, 574, A68

Ford, E. B., & Rasio, F. A. 2008, ApJ, 686, 621

Fromang, S., Terquem, C., & Nelson, R. P. 2005, MNRAS, 363, 943

Fu, W., Li, H., Lubow, S., & Li, S. 2014, ApJl, 788, L41

Fukagawa, M., et al. 2013, PASJ, 65, L14

Fung, J., Shi, J.-M., & Chiang, E. 2014, ApJ, 782, 88

Galli, D., Lizano, S., Shu, F. H., & Allen, A. 2006, ApJ, 647, 374

Gammie, C. F. 1996, ApJ, 457, 355

Goldreich, P., & Nicholson, P. D. 1989, ApJ, 342, 1075

Goldreich, P., & Tremaine, S. 1979, ApJ, 233, 857

—. 1980, ApJ, 241, 425

Goodman, J., & Rafikov, R. R. 2001, ApJ, 552, 793

Guilet, J., Baruteau, C., & Papaloizou, J. C. B. 2013, MNRAS, 430, 1764

Herbig, G. H. 1960, ApJs, 4, 337

Hughes, A. M., et al. 2009, ApJ, 698, 131

Ida, S., & Lin, D. N. C. 2008, ApJ, 673, 487

Inaba, S., & Barge, P. 2006, ApJ, 649, 415

Isella, A., Pérez, L. M., Carpenter, J. M., Ricci, L., Andrews, S., & Rosenfeld, K. 2013, ApJ, 775, 30

Jeans, J. H. 1902, Royal Society of London Philosophical Transactions Series A, 199, 1

Johansen, A., Henning, T., & Klahr, H. 2006, ApJ, 643, 1219

Johansen, A., Oishi, J. S., Mac Low, M.-M., Klahr, H., Henning, T., & Youdin, A. 2007, Nature, 448, 1022

Johnson, E. T., Goodman, J., & Menou, K. 2006, ApJ, 647, 1413

Johnstone, D., Hollenbach, D., & Bally, J. 1998, ApJ, 499, 758

Joy, A. H. 1942, PASP, 54, 15

—. 1945, ApJ, 102, 168

—. 1949, ApJ, 110, 424

Juhász, A., Benisty, M., Pohl, A., Dullemond, C. P., Dominik, C., & Paardekooper, S.-J. 2015, MNRAS, 451, 1147

Jurić, M., & Tremaine, S. 2008, ApJ, 686, 603

Kanagawa, K. D., Tanaka, H., Muto, T., Tanigawa, T., & Takeuchi, T. 2015, MNRAS, 448, 994

Keith, S. L., & Wardle, M. 2015, MNRAS, 451, 1104

Kenyon, S. J., & Bromley, B. C. 2002, AJ, 123, 1757

—. 2004, AJ, 127, 513

Kenyon, S. J., & Hartmann, L. 1987, ApJ, 323, 714

Klahr, H. 2004, ApJ, 606, 1070

Klahr, H., & Bodenheimer, P. 2006, ApJ, 639, 432

Klahr, H., & Hubbard, A. 2014, ApJ, 788, 21

Klahr, H., & Kley, W. 2006, A&A, 445, 747

Klahr, H. H., & Bodenheimer, P. 2003, ApJ, 582, 869

Klahr, H. H., & Henning, T. 1997, Icarus, 128, 213

Kley, W., Bitsch, B., & Klahr, H. 2009, A&A, 506, 971

Kley, W., & Crida, A. 2008, A&A, 487, L9

Kley, W., & Dirksen, G. 2006, A&A, 447, 369

Kley, W., Lee, M. H., Murray, N., & Peale, S. J. 2005, A&A, 437, 727

Kley, W., Müller, T. W. A., Kolb, S. M., Benítez-Llambay, P., & Masset, F. 2012, A&A, 546, A99

Kley, W., & Nelson, R. P. 2012, ARA&A, 50, 211

Kley, W., Peitz, J., & Bryden, G. 2004, A&A, 414, 735

Kokubo, E., & Ida, S. 1996, Icarus, 123, 180

—. 1998, Icarus, 131, 171

Koller, J., Li, H., & Lin, D. N. C. 2003, ApJl, 596, L91

Kolmogorov, A. 1941, Akademiia Nauk SSSR Doklady, 30, 301

Korycansky, D. G., & Pollack, J. B. 1993, Icarus, 102, 150

Kuiper, G. P. 1951, Proceedings of the National Academy of Science, 37, 1

Kuiper, R., Klahr, H., Dullemond, C., Kley, W., & Henning, T. 2010, A&A, 511, A81

Kuiper, R., & Klessen, R. S. 2013, A&A, 555, A7

Lai, D., Foucart, F., & Lin, D. N. C. 2011, MNRAS, 412, 2790

Larson, R. B. 1981, MNRAS, 194, 809

Laughlin, G., Steinacker, A., & Adams, F. C. 2004, ApJ, 608, 489

Lee, M. H., & Peale, S. J. 2002, ApJ, 567, 596

Lega, E., Crida, A., Bitsch, B., & Morbidelli, A. 2014, MNRAS, 440, 683

Lega, E., Morbidelli, A., Bitsch, B., Crida, A., & Szulagyi, J. 2015, ArXiv e-prints

Les, R., & Lin, M.-K. 2015, MNRAS, 450, 1503

Lesur, G., & Papaloizou, J. C. B. 2010, A&A, 513, A60

Li, H., Finn, J. M., Lovelace, R. V. E., & Colgate, S. A. 2000, ApJ, 533, 1023

Li, H., Lubow, S. H., Li, S., & Lin, D. N. C. 2009, ApJl, 690, L52

Li, Z.-Y., Banerjee, R., Pudritz, R. E., Jørgensen, J. K., Shang, H., Krasnopolsky, R., & Maury, A. 2014, Protostars and Planets VI, 173

Lin, D. N. C., & Papaloizou, J. 1979, MNRAS, 186, 799

—. 1986, ApJ, 309, 846

Lin, M.-K. 2012a, ApJ, 754, 21

—. 2012b, MNRAS, 426, 3211

Lin, M.-K., & Papaloizou, J. C. B. 2011a, MNRAS, 415, 1445

—. 2011b, MNRAS, 415, 1426

Lissauer, J. J., et al. 2011, Nature, 470, 53

Lobo Gomes, A., Klahr, H., Uribe, A. L., Pinilla, P., & Surville, C. 2015, ApJ, 810, 94

Lovelace, R. V. E., Li, H., Colgate, S. A., & Nelson, A. F. 1999, ApJ, 513, 805

Lubow, S. H. 1991, ApJ, 381, 259

Lynden-Bell, D., & Pringle, J. E. 1974, MNRAS, 168, 603

Lyra, W. 2014, ApJ, 789, 77

Lyra, W., Johansen, A., Klahr, H., & Piskunov, N. 2009a, A&A, 493, 1125

Lyra, W., Johansen, A., Zsom, A., Klahr, H., & Piskunov, N. 2009b, A&A, 497, 869

Lyra, W., & Mac Low, M.-M. 2012, ApJ, 756, 62

Lyra, W., Paardekooper, S.-J., & Mac Low, M.-M. 2010, ApJl, 715, L68

Masset, F., & Snellgrove, M. 2001, MNRAS, 320, L55

Masset, F. S. 2001, ApJ, 558, 453

—. 2002, A&A, 387, 605

Masset, F. S. 2008, in EAS Publications Series, Vol. 29, EAS Publications Series, ed. M.-J. Goupil & J.-P. Zahn, 165–244

Masset, F. S., & Casoli, J. 2009, ApJ, 703, 857

—. 2010, ApJ, 723, 1393

Masset, F. S., Morbidelli, A., Crida, A., & Ferreira, J. 2006, ApJ, 642, 478

Masset, F. S., & Papaloizou, J. C. B. 2003, ApJ, 588, 494

Matsumura, S., Thommes, E. W., Chatterjee, S., & Rasio, F. A. 2010, ApJ, 714, 194

Mayor, M., & Queloz, D. 1995, Nature, 378, 355

McCaughrean, M. J., & O'dell, C. R. 1996, AJ, 111, 1977

McNeil, D., Duncan, M., & Levison, H. F. 2005, AJ, 130, 2884

Meheut, H., Lovelace, R. V. E., & Lai, D. 2013, MNRAS, 430, 1988

Meheut, H., Meliani, Z., Varniere, P., & Benz, W. 2012a, A&A, 545, A134

Meheut, H., Yu, C., & Lai, D. 2012b, MNRAS, 422, 2399

Mendoza V., E. E. 1966, ApJ, 143, 1010

—. 1968, ApJ, 151, 977

Mestel, L. 1965, QJRAS, 6, 161

Mignone, A., Bodo, G., Massaglia, S., Matsakos, T., Tesileanu, O., Zanni, C., & Ferrari, A. 2007, ApJs, 170, 228

Mizuno, H. 1980, Progress of Theoretical Physics, 64, 544

Morbidelli, A., & Crida, A. 2007, Icarus, 191, 158

Morbidelli, A., Crida, A., Masset, F., & Nelson, R. P. 2008, A&A, 478, 929

Mordasini, C., Alibert, Y., & Benz, W. 2009, A&A, 501, 1139

Morohoshi, K., & Tanaka, H. 2003, MNRAS, 346, 915

Mouschovias, T. C. 1976, ApJ, 207, 141

—. 1979a, ApJ, 228, 475

—. 1979b, ApJ, 228, 159

Mouschovias, T. C., & Paleologou, E. V. 1979, ApJ, 230, 204

Müller, T. W. A., Kley, W., & Meru, F. 2012, A&A, 541, A123

Mustill, A. J., & Wyatt, M. C. 2011, MNRAS, 413, 554

Muto, T., Machida, M. N., & Inutsuka, S.-i. 2008, ApJ, 679, 813

Natta, A. 1993, ApJ, 412, 761

Nelson, R. P. 2005, A&A, 443, 1067

Nelson, R. P., & Gressel, O. 2010, MNRAS, 409, 639

Nelson, R. P., & Papaloizou, J. C. B. 2002, MNRAS, 333, L26

—. 2004, MNRAS, 350, 849

Nelson, R. P., Papaloizou, J. C. B., Masset, F., & Kley, W. 2000, MNRAS, 318, 18

Norman, C., & Silk, J. 1980, ApJ, 238, 158

O'Brien, D. P., Morbidelli, A., & Levison, H. F. 2006, Icarus, 184, 39

O'dell, C. R., Wen, Z., & Hu, X. 1993, ApJ, 410, 696

Ogilvie, G. I., & Lubow, S. H. 2002, MNRAS, 330, 950

—. 2003, ApJ, 587, 398

Ou, S., Ji, J., Liu, L., & Peng, X. 2007, ApJ, 667, 1220

Owen, J. E., Ercolano, B., & Clarke, C. J. 2011, MNRAS, 412, 13

Owen, J. E., Ercolano, B., Clarke, C. J., & Alexander, R. D. 2010, MNRAS, 401, 1415

Paardekooper, S.-J., Baruteau, C., Crida, A., & Kley, W. 2010a, MNRAS, 401, 1950

Paardekooper, S.-J., Baruteau, C., & Kley, W. 2011, MNRAS, 410, 293

Paardekooper, S.-J., Lesur, G., & Papaloizou, J. C. B. 2010b, ApJ, 725, 146

Paardekooper, S.-J., & Mellema, G. 2006, A&A, 459, L17

Paardekooper, S.-J., & Papaloizou, J. C. B. 2008, A&A, 485, 877

—. 2009, MNRAS, 394, 2283

Papaloizou, J., & Lin, D. N. C. 1984, ApJ, 285, 818

Papaloizou, J. C. B., & Larwood, J. D. 2000, MNRAS, 315, 823

Papaloizou, J. C. B., Nelson, R. P., & Masset, F. 2001, A&A, 366, 263

Papaloizou, J. C. B., Nelson, R. P., & Snellgrove, M. D. 2004, MNRAS, 350, 829

Papaloizou, J. C. B., & Szuszkiewicz, E. 2005, MNRAS, 363, 153

Pérez, L. M., Isella, A., Carpenter, J. M., & Chandler, C. J. 2014, ApJl, 783, L13

Perri, F., & Cameron, A. G. W. 1974, Icarus, 22, 416

Petersen, M. R., Julien, K., & Stewart, G. R. 2007a, ApJ, 658, 1236

Petersen, M. R., Stewart, G. R., & Julien, K. 2007b, ApJ, 658, 1252

Pierens, A., & Huré, J.-M. 2005, A&A, 433, L37

Pierens, A., & Nelson, R. P. 2008, A&A, 482, 333

Pinilla, P., Benisty, M., & Birnstiel, T. 2012, A&A, 545, A81

Pinilla, P., de Juan Ovelar, M., Ataiee, S., Benisty, M., Birnstiel, T., van Dishoeck, E. F., & Min, M. 2015, A&A, 573, A9

Pollack, J. B., Hubickyj, O., Bodenheimer, P., Lissauer, J. J., Podolak, M., & Greenzweig, Y. 1996, Icarus, 124, 62

Quanz, S. P., Avenhaus, H., Buenzli, E., Garufi, A., Schmid, H. M., & Wolf, S. 2013, ApJl, 766, L2

Quillen, A. C. 2006, MNRAS, 365, 1367

Raettig, N., Lyra, W., & Klahr, H. 2013, ApJ, 765, 115

Rafikov, R. R. 2002, ApJ, 572, 566

Raymond, S. N., et al. 2011, A&A, 530, A62

Raymond, S. N., Quinn, T., & Lunine, J. I. 2006, Icarus, 183, 265

Regály, Z., Juhász, A., Sándor, Z., & Dullemond, C. P. 2012, MNRAS, 419, 1701

Regály, Z., Király, S., & Kiss, L. L. 2014, ApJl, 785, L31

Regály, Z., Sándor, Z., Csomós, P., & Ataiee, S. 2013, MNRAS, 433, 2626

Regály, Z., Sándor, Z., Dullemond, C. P., & van Boekel, R. 2010, A&A, 523, A69

Rein, H., Papaloizou, J. C. B., & Kley, W. 2010, A&A, 510, A4

Rice, W. K. M., Armitage, P. J., Bate, M. R., & Bonnell, I. A. 2003, MNRAS, 339, 1025

Richard, S., Barge, P., & Le Dizès, S. 2013, A&A, 559, A30

Ruge, J. P., Wolf, S., Uribe, A. L., & Klahr, H. H. 2013, A&A, 549, A97

—. 2014, A&A, 572, L2

Safronov, V. S. 1972, Evolution of the protoplanetary cloud and formation of the earth and planets.

Santos-Lima, R., de Gouveia Dal Pino, E. M., & Lazarian, A. 2012, ApJ, 747, 21

Shakura, N. I., & Sunyaev, R. A. 1973, A&A, 24, 337

Shlosman, I., & Begelman, M. C. 1989, ApJ, 341, 685

Shu, F. H., Adams, F. C., & Lizano, S. 1987, ARA&A, 25, 23

Shu, F. H., Galli, D., Lizano, S., Glassgold, A. E., & Diamond, P. H. 2007, ApJ, 665, 535

Simon, M., & Prato, L. 1995, ApJ, 450, 824

Smith, B. A., & Terrile, R. J. 1984, Science, 226, 1421

Snellgrove, M. D., Papaloizou, J. C. B., & Nelson, R. P. 2001, A&A, 374, 1092

Spitzer, Jr., L. 1968, Dynamics of Interstellar Matter and the Formation of Stars, ed. B. M. Middlehurst & L. H. Aller (the University of Chicago Press), 1

Strom, S. E., Strom, K. M., & Grasdalen, G. L. 1975, ARA&A, 13, 187

Su, K. Y. L., et al. 2005, ApJ, 628, 487

Surville, C., & Barge, P. 2012, ArXiv e-prints

Surville, C., & Barge, P. 2013, in European Physical Journal Web of Conferences, Vol. 46, European Physical Journal Web of Conferences, 5002

Takeda, G., & Rasio, F. A. 2005, ApJ, 627, 1001

Tanaka, H., Takeuchi, T., & Ward, W. R. 2002, ApJ, 565, 1257

Tanaka, H., & Ward, W. R. 2004, ApJ, 602, 388

Terebey, S., Shu, F. H., & Cassen, P. 1984, ApJ, 286, 529

Terquem, C. E. J. M. L. J. 2003, MNRAS, 341, 1157

Toomre, A. 1964, ApJ, 139, 1217

Triaud, A. H. M. J., et al. 2010, A&A, 524, A25

Umurhan, O. M. 2010, A&A, 521, A25

Uribe, A., Bans, A., & Königl, A. 2015, ApJ, 802, 54

Uribe, A. L., Klahr, H., Flock, M., & Henning, T. 2011, ApJ, 736, 85

Uribe, A. L., Klahr, H., & Henning, T. 2013, ApJ, 769, 97

van der Marel, N., et al. 2013, Science, 340, 1199

Varnière, P., Quillen, A. C., & Frank, A. 2004, ApJ, 612, 1152

Varnière, P., & Tagger, M. 2006, A&A, 446, L13

Walsh, K. J., Morbidelli, A., Raymond, S. N., O'Brien, D. P., & Mandell, A. M. 2011, Nature, 475, 206

Wang, Z., Chakrabarty, D., & Kaplan, D. L. 2006, Nature, 440, 772

Ward, W. R. 1986, Icarus, 67, 164

—. 1988, Icarus, 73, 330

—. 1989, ApJ, 336, 526

Ward, W. R. 1991, in Lunar and Planetary Inst. Technical Report, Vol. 22, Lunar and Planetary Science Conference, 1463

—. 1997, Icarus, 126, 261

Weidenschilling, S. J. 1977, MNRAS, 180, 57

—. 1997, Icarus, 127, 290

Weingartner, J. C., & Draine, B. T. 2001, ApJ, 548, 296

Wetherill, G. W., & Stewart, G. R. 1989, Icarus, 77, 330

Whipple, F. L. 1972, in From Plasma to Planet, ed. A. Elvius, 211

Williams, J. P., & Cieza, L. A. 2011, ARA&A, 49, 67

Windmark, F., Birnstiel, T., Güttler, C., Blum, J., Dullemond, C. P., & Henning, T. 2012, A&A, 540, A73

Winters, W. F., Balbus, S. A., & Hawley, J. F. 2003, ApJ, 589, 543

Wolk, S. J., & Walter, F. M. 1996, AJ, 111, 2066

Wolszczan, A., & Frail, D. A. 1992, Nature, 355, 145

Xiang-Gruess, M., & Papaloizou, J. C. B. 2013, MNRAS, 431, 1320

Yamada, K., & Inaba, S. 2011, MNRAS, 411, 184

Youdin, A. N. 2011, ApJ, 742, 38

Yu, C., Li, H., Li, S., Lubow, S. H., & Lin, D. N. C. 2010, ApJ, 712, 198

Zhu, Z., & Stone, J. M. 2014, ApJ, 795, 53

Zhu, Z., Stone, J. M., & Rafikov, R. R. 2013, ApJ, 768, 143

Zhu, Z., Stone, J. M., Rafikov, R. R., & Bai, X.-n. 2014, ApJ, 785, 122

Zsom, A., Ormel, C. W., Güttler, C., Blum, J., & Dullemond, C. P. 2010, A&A, 513, A57

Zuckerman, B., & Palmer, P. 1974, ARA&A, 12, 279

Acknowledgements

"All things are difficult before they are easy". I got this message in a fortune cookie during my second year as a PhD student and since then I kept this quotation. Now that I got to the point that I am writing my thesis acknowledgments, I would like to share this *fortune* with whoever reads this text.

Em primeiro lugar, eu gostaria de agradecer a minha família por sempre me encorajar a seguir os meus sonhos. Obrigada pelo amor, pela paciência, pelo interesse e por todas as mensagens trocadas diariamente. As fotos e videos sempre fizeram me sentir um pouco presente nos inúmeros eventos que acabei perdendo. Obrigada aos meus pais Antonio e Maria. Obrigada as minhas irmãs Leo, Li e Mile. Obrigada aos meus sobrinhos João e Toninha. Obrigada aos meus cunhados André e Pieter. Obrigada aos meus bisavós, avós, tios, primos e agregados. Eu me considero como uma pessoa de muita sorte por ter uma família tão grande e querida. I would also like to especially thank Ben, without you by my side, this journey would have been much more difficult and less fun. Thank you for encouraging me to live a healthy life and to change some bad habits, it is actually very nice to see the daylight. *Merci, Ben!*

I would like to thank my supervisor Hubert for giving me the opportunity to pursue my PhD in Heidelberg. Thank you for giving me a great project to work with, which was difficult at many times, but I am very glad to see the results of all the hard work. Thanks for the discussions and for your enthusiasm. Special thanks also go to some other people that made this work possible. Thanks Ana for sharing your planet-disk PLUTO module with me, for being always so good at answering my questions, and to share your knowledge with me. I would also like to especially thank Paola: you were instrumental for the completion of this thesis, bringing me back the motivation I was lacking. The first paper would have never been possible, without you showing me the way to go. Thanks also to Clément for helping me to understand more about vortices, for the discussions and your interest in my work. Thanks also to Rolf for sharing your radiation transport PLUTO module with me. Thank you for the hours spent with me to solve technical issues and for always being so prompt in giving me feedback.

A special thanks also goes to Paulina. *Dziękuję Paulina!* You are the first friend I made in Heidelberg and you will be always in my heart. All the adventures and nice moments we had together are saved in my memory as one of the best things I lived in Heidelberg. Thank you also for always being such a good friend at all moments. Alongside Paulina, I would like to thank the non-astronomers: Alex, Florian, Kerstin, and Stefano. Thank you for making my life more cheerful, since the first weeks I arrived in Heidelberg. Thanks also to Aleksey for sharing some great times together. There are many nice people I met outside astronomy that made life more fun. Thank you all!

Another two great friends I made at the institute are Maria and Sara. Thank you girls for making the daily-life at work a lot more pleasant, thank you for nice words in difficult times and for nice moments shared outside the office. I would also like to thank Elena, Taisiya, and Tobias. Thank you guys for fun dinners, parties, and for always being interested in my well being. Some other special people I would like to thank are Adriana and Simona. Thank you girls for reading over my Introduction. Thanks Adriana for the help with translating the *Zusammenfassung* and for your careful comments for the Introduction. Thanks Simona for hosting me during the few days I was homeless, thank you for the holidays we had together after a conference, thanks for always being there. I would also like to thank Gabriel and Nick, you two are very great people with very great minds that I had the pleasure to meet in Heidelberg. Thanks to all the other students with whom I shared some nice experiences.

Eu também não posso deixar de agradecer aos meus amigos brasileiros, os de nascimento e os de coração, pros quais a distância nunca foi um problema. Obrigada por serem como uma segunda família para mim. Obrigada ao *all star gang*: Caio, Dai, Má, Marcelo e Ná. Vocês me acompanharam desde o ínicio da graduação e a amizade de vocês é o melhor presente que eu obtive na Física. Obrigada pelas mensagens trocadas diariamente e por fazerem parte da minha vida. Obrigada ao Dani, que chegou um pouquinho mais tarde. É sempre legal de ver a afinidade que temos, e com a Daizinha também. Muito obrigada por me compreender e por sempre estar disponível em todos os momentos. Obrigada a minha florzinha Thaíse por sempre estar presente, ainda que virtualmente, as nossas inúmeras mensagens foram sempre importantes para me fazer seguir em frente. As amizades sua e do Reinaldo foram os melhores presentes que eu obtive no mestrado. Obrigada ao Reinaldo por sempre estar disposto a responder as minhas dúvidas de física e astronomia, mais do que isso pelas ótimas vibrações que você sempre me envia. Obrigada a Andressa, minha amiga brasileira em Munique, foi muito legal o quanto nos aproximamos depois de que mudei pra Alemanha, obrigada também pelas dicas

quando decidi aplicar para doutorado fora. *Merci Fred*, foi muito legal ir te visitar em Londres, obrigada também pelas dicas para as aplicações de posdoc e por sempre se manter em contato. *Gracias Jose, mi hermano español*, obrigada pela visita em Heidelberg e por sempre se manter em contato e se mostrar interessado com o desenvolvimento da minha vida. Obrigada a Cintia, Cói, Leila e Pri, amigos que eu carrego desde a infância/adolescência, vocês sempre morarão no meu coração. Obrigada também a Akm, Aline e Clé os meus primeiros amigos da Física, ainda que nossos caminhos tomaram rumos tão diferentes, é legal de ver como nunca perdemos o contato e vocês são pessoinhas muito especiais na minha vida.

I would like to thank my thesis committee members Christian Fendt and Sebastian Wolf for their advice, interest, and support. To the PhD Student Advisory Committee members for their general support and advice on how to deal with time constraints. I am grateful to Andreas Quirrenbach for accepting to be a referee for my thesis. Thanks also to Henrik Beuther and Stephanie Hansmann-Menzemer for accepting to be part of my examination committee.

I am very thankful to the International Max Planck Research School (IMPRS) programme, in particular to Christian Fendt. It was great to have you as a member of my thesis committee, thanks for taking such a good care of this PhD programme in Heidelberg. You are concerned not only about our success as students, but also that we are personally happy and I appreciate that a lot. I would also like to thank the 8th IMPRS generation for great times together during and after the IMPRS seminars and during our retreats. Thanks to the Heidelberg Graduate School of Fundamental Physics for financial support for *Deutschunterricht* and for organizing the Graduate Days twice a year. It is always very nice to go there and to learn also about non-astronomy related topics.

It was a great privilege to pursue my PhD at the Max-Planck-Institut für Astronomie. Thanks to all the *Mitarbeiter* for making the work environment a very relaxed place. In particular, I would like to thank Marion for always being so kind. *Danke Marion, dass du versuchst mit mir Deutsch zu reden.*

Finally, I would like to thank financial support from the Deutsche Forschungsgemeinschaft, grant n. KL 1469/9-1. This work used the PLUTO code and the simulations were performed at the THEO and HYDRA clusters of the Rechenzentrum Garching of the Max Planck Society.

Declaration

I hereby declare that except where specific reference is made to the work of others, the contents of this thesis are original and produced by me. This thesis have not been submitted in whole or in part for consideration for any other degree or qualification in this, or any other university.

The work presented in this thesis was conducted from 2012 to 2015 under supervision of PD. Dr. Hubert Klahr at the Max-Planck-Institut für Astronomie. As in Astrophysics research is often done in collaboration with others, I have benefited of extra assistance from Dr. Ana Uribe, Dr. Paola Pinilla, Dr. Clément Surville, and Dr. Rolf Kuiper for technical issues and discussions regarding the interpretation of the results.

Alara Lobo Gomes

Heidelberg, 17 August 2015